Title
Identification of modulators of deoxyribonucleotide pools and replication stress in cancer

Author
Poddar, Soumya

Publication Date
2019

Peer reviewed|Thesis/dissertation

UNIVERSITY OF CALIFORNIA

Los Angeles

Identification of modulators of deoxyribonucleotide pools and replication stress in cancer

A dissertation submitted in partial satisfaction of the

requirements for the degree Doctor of Philosophy

in Molecular and Medical Pharmacology

by

Soumya Poddar

2019

ABSTRACT OF THE DISSERTATION

Identification of modulators of deoxyribonucleotide pools and replication stress in cancer

By

Soumya Poddar

Doctor of Philosophy in Molecular and Medical Pharmacology

University of California, Los Angeles, 2018

Professor Caius G. Radu, Chair

Regulation of intracellular deoxyribonucleotide triphosphate (dNTP) pools are critical for DNA replication and repair. DNA replication is a highly demanding process, which requires precise timing and supply of adequate unmodified dNTPs. Imbalanced dNTP pools can lead to genomic instability and result in cancer development. Several studies have reported cancer cells are more susceptible than normal cells to perturbations in the quantity, quality and balance of dNTP pools. Therefore, therapeutic agents targeting dNTP synthesis have been used for treatment of several types of cancer. Despite these studies, the molecular mechanisms that regulate quantity and quality of dNTP pools are not completely understood. Studying the crosstalk between metabolic and signaling mechanisms for regulation of dNTP pools are required to develop better pharmacological interventions against cancer.

Dysregulation of dNTP pools can occur in different ways -

Modulators of dNTP pools' quantity: Similar to other major branches of cellular metabolism, nucleotide biosynthesis consists of redundant and convergent biosynthetic pathways. dNTPs required for DNA replication and repair can be produced by the de novo pathway (DNP) or by the nucleoside salvage pathway (NSP). Therefore, both pathways are required to be targeted simultaneously to achieve therapeutic efficacy.

Modulators of dNTP pools' quality: Reactive oxygen species (ROS), generated by both endogenous and exogenous routes can pose a significant threat to cellular integrity by inducing oxidative damage. This results in DNA base modifications, formation of apurinic/apyrimidinic lesions, which can be mutagenic and lead to DNA damage. Hence, pharmacological intervention by redox modulators is being investigated as promising anti-cancer therapy.

Regulation of dNTP pools by signaling pathways: Dysregulation of quantity or quality of dNTP pools lead to transient disruption of replication fork progression, termed as replication stress (RS), defined by accumulation of unprotected single-stranded DNA (ssDNA) at stalled replication forks. In order to protect genomic integrity, cells activate the replication stress response (RSR) pathway to limit the amount of ssDNA and subsequent DNA damage. However, the metabolic consequences of RSR on nucleotide metabolism are poorly understood.
This thesis focuses on development of pharmacological modulators to regulate dNTP pools. Further it explores the interconnections between these dNTP pool modulators and replication stress to establish combination therapies against cancer.

In Chapter 1, we identified metabolic alterations in response to ATR inhibition in acute lymphoblastic leukemia, and developed a combination therapy targeting the metabolic vulnerabilities.

In Chapter 2, we developed a novel dCK (the rate-limiting enzyme of NSP) inhibitor, with improved metabolic stability and bioavailability. We studied preclinical pharmacokinetics and dose-response relationships of dCK inhibitor for translation to first in-human clinical trials.

In Chapter 3, we evaluated a series of novel isoquinoline based thiosemicarbazone compounds to discover a highly potent copper ionophore which induces oxidative stress and DNA damage against aggressive solid tumor models.

In Chapter 4, we designed and applied a metabolic modifier screen which identified multiple protein kinase inhibitors as having non-canonical targets within pyrimidine metabolism.

The dissertation of Soumya Poddar is approved.

Michael E Jung

Timothy R Donahue

Johannes Czernin

Edmund Capparelli

Caius Gabriel Radu, Chair

University of California, Los Angeles

2019

DEDICATION

I would like to dedicate this dissertation to my father, Dr. Hiranmoy Poddar and my mother, Mrs. Bithi Poddar for their love and support throughout my life. My Dad, a surgeon himself, who passed away at the age of 49 due to cancer has been my greatest inspiration throughout my scientific training. Thank you Maa for your incredible support, inspiration and motivation throughout my life. If not for you, I will never be the person I am today.

TABLE OF CONTENTS

LIST OF FIGURES

CHAPTER 1

CHAPTER 2

CHAPTER 3

CHAPTER 4

ACKNOWLEDGEMENTS

This doctoral thesis is a product of an amazing team, and I am thankful to everyone who have helped me through this journey.

Firstly, I would like to thank Dr. Caius Radu for giving me the opportunity to develop my doctoral thesis in his lab and his continued support throughout my graduate career. I want to thank him for his scientific advice and mentorship that made this thesis possible. I am grateful that he always pushed me to be the scientist I am today.

I would like to thank the members of my doctoral committee Dr. Johannes Czernin, Dr. Timothy Donahue, Dr. Edmund Capparelli, Dr. Michael Jung as well as my former committee members Dr. Owen Witte and Dr. Michael Teitell for their expert advice and suggestions during my committee meetings.

I would like to thank all my colleagues of Radu/Czernin/Donahue laboratory, especially Thuc Le, Evan Abt, Woosuk Kim, Joseph Capri, Ethan Rosser, Daniel Sun and Roy Pan for all the assistance over these years. None of these projects would have been possible without their dedicated efforts.

I would like to thank Dr. Liu Wei and Lawrence Pang for their help with the mPET/CT imaging studies.

Last but not least, I would like to thank my family, especially my mother, my younger brother for their active support throughout this time. I would like to express my appreciation to my beloved wife, Tanya for endless scientific discussions, for always being my support in need and for all the great times we spent together.

VITA

2011	Bachelor of Engineering, Biotechnology Indian Institute of Technology, Kharagpur Kharagpur, India
2012	Master of Engineering, Biochemical Engineering Indian Institute of Technology, Kharagpur Kharagpur, India
2013-2019	Graduate Student Researcher Department of Molecular and Medical Pharmacology University of California, Los Angeles Los Angeles, CA, USA

Publications

1. Abt ER[#], Rosser EW[#], Durst MA[#], **Poddar S**, Lok V, Kim W, Song J, Capri JR, Le TM, Slavik R, Jung ME, Damoiseaux R, Czernin J, Donahue TR, Lavie A and Radu CG. Metabolic modifier screen reveals secondary targets of protein kinase inhibitors within nucleotide metabolism. Under review in **Cell Chem Bio**, 2019. ([#] equal contribution)

2. **Poddar S[#]**, Capparelli E, Rosser E, Wei L, Le TM, Radu CG and Nikanjam M. Development and preclinical pharmacology of a novel dCK inhibitor, DI-87. Submitted to **Br J Pharmacol**, 2019.

3. Sun DL[#], **Poddar S[#]**, Pan RD, Valkenburgh JV, Rosser EW, Abt ER, Lok V, Capri J, Hernandez SP, Song J, Li J, Vergnes L, Cabebe A, Armstrong WR, Plamthottam S, Steele D, Osto C, Stuparu A, Le TM, Reue K, Damoiseaux R, Czernin J and Radu CG. Evaluation of potent isoquinoline-based thiosemicarbazone antiproliferatives against solid tumor models. Submitted to **J Med Chem**, 2019. ([#] equal contribution)

4. Elliott IA, Dann AM, Kim SS, Abt ER, Kim W, **Poddar S**, Moore A, Zhou L, Williams JL, Capri JR, Ghukasyan R, Matsumura C, Tucker DA, Armstrong WR, Cabebe AE, Wu N, Li L, Le TM, Radu CG and Donahue TR. Lysosome inhibition sensitizes pancreatic cancer to replication stress by aspartate depletion. **Proc Nat Acad Sci USA**. 2019 Mar 20.

5. Fendler WP, Stuparu AD, Evans-Axelsson S, Lückerath K, Wei L, Kim W, **Poddar S**, Said J, Radu CG, Eiber M, Czernin J, Slavik R, Herrmann K. Establishing 177Lu-PSMA-617 radioligand therapy in a syngeneic model of murine prostate cancer. **J Nucl Med**. 2017 May 25. pii: jnumed.117.193359.

6. Le TM[#], **Poddar S[#]**, Capri JR[#], Abt ER, Kim W, Wei L, Uong NT, Cheng CM, Braas D, Nikanjam M, Rix P, Merkurjev D, Zaretsky J, Kornblum HI, Ribas A, Herschman HR, Whitelegge J, Faull KF, Donahue TR, Czernin J, Radu CG. ATR inhibition facilitates targeting of leukemia dependence on convergent nucleotide biosynthetic pathways. **Nat Commun.** 2017 Aug 14;8(1):241. ([#] equal contribution)

7. Kim W[#], Le TM[#], Wei L, **Poddar S**, Bazzy J, Wang X, Uong NT, Abt ER, Capri JR, Austin WR, Van Valkenburgh JS, Steele D, Gipson RM, Slavik R, Cabebe AE, Taechariyakul T,

Yaghoubi SS, Lee JT, Sadeghi S, Lavie A, Faull KF, Witte ON, Donahue TR, Phelps ME, Herschman HR, Herrmann K, Czernin J, and Radu CG. [^{18}F]CFA as a clinically translatable probe for PET imaging of deoxycytidine kinase activity. **Proc Nat Acad Sci USA**. 2016 Apr 12;113(15):4027-32. (# equal contribution)

8. Nomme J, Li Z, Gipson RM, Wang J, Armijo AL, Le T, **Poddar S**, Smith T, Santarsiero BD, Nguyen HA, Czernin J, Alexandrova AN, Jung ME, Radu CG, Lavie A. Structure-guided development of deoxycytidine kinase inhibitors with nanomolar affinity and improved metabolic stability. **J Med Chem**. 2014 Nov 26;57(22):9480-94.

9. Paul D, **Poddar S**, Sar P. Characterization of arsenite-oxidizing bacteria isolated from arsenic-contaminated groundwater of West Bengal. **J Environ Sci Health A Tox Hazard Subst Environ Eng.** 2014;49(13):1481-92.

10. Crotty D#, Silkstone G#, **Poddar S**, Ranson R, Prina-Mello A, Wilson MT, Coey JM. Reexamination of magnetic isotope and field effects on adenosine triphosphate production by creatine kinase. **Proc Natl Acad Sci U S A.** 2012 Jan 31;109(5):1437-42. (# equal contribution)

Patents

1. Radu CG, **Poddar S**, Czernin J, Nathanson D and Le TM. (2016). “Combination Cancer Therapy”. ***US Patent No. US2016/017199*** filed Feb 09, 2016.

2. Radu CG, Sun D, **Poddar S,** Pan R, Valkenburgh JV and Jung ME (2019). “Thiosemicarbazone Compounds”. ***US Patent No.048539-553PO1US*.**

Presentations

1. **Poddar S** (2017 and 2019) “Relating tumor drug concentrations to target effect with semi-physiologic PK-PD modeling in drug development: an application using novel dCK inhibitor”. American association of cancer research (AACR) hosted in Washington D.C. in 2017 and Georgia, Atlanta in 2019.

2. **Poddar S** (2016) “Targetable dependence on convergent nucleotide biosynthetic pathways in leukemia is facilitated by ATR inhibition” and “Development of Ribonucleotide reductase inhibitors for efficacy against solid tumors”. UCLA Pharmacology Annual retreat hosted in Huntington Beach. Won best poster award for both posters.

CHAPTER 1

Targetable dependence on convergent nucleotide biosynthetic pathways in leukemia is facilitated by ATR inhibition

ABSTRACT

Leukemia cells rely on two nucleotide biosynthetic pathways, *de novo* and salvage, to produce dNTPs for DNA replication. Using metabolomic, proteomic, and phosphoproteomic approaches, we show that inhibition of the replication stress sensing kinase ataxia telangiectasia and Rad3-related protein (ATR) reduced the output of both *de novo* and salvage pathways by regulating the activity of their respective rate-limiting enzymes, ribonucleotide reductase (RNR) and deoxycytidine kinase (dCK), via distinct molecular mechanisms. Quantification of nucleotide biosynthesis in ATR-inhibited acute lymphoblastic leukemia (ALL) cells revealed substantial remaining *de novo* and salvage activities, and could not eliminate the disease *in vivo*. However, targeting these remaining activities with RNR and dCK inhibitors triggered lethal replication stress *in vitro* and long-term disease-free survival in mice with B-ALL, without detectable toxicity. The functional interplay between alternative nucleotide biosynthetic routes and ATR provides new therapeutic opportunities in leukemia and potentially other cancers.

INTRODUCTION

Unabated proliferation is a hallmark of cancer which requires new DNA synthesis from deoxyribonucleotide triphosphates (dNTPs). However, cellular dNTP levels only suffice to sustain a few minutes of DNA replication indicating that dNTP pools are produced “on demand” via tightly regulated biosynthetic pathways[1]. These deoxynucleotide biosynthetic pathways, termed *de novo* and salvage, rely on distinct carbon and nitrogen sources[2]. *De novo* pathways use glucose and amino acids to produce ribonucleotide diphosphates (rNDPs) which are converted into deoxyribonucleotide diphosphates (dNDPs) by ribonucleotide reductase (RNR), a two-subunit enzyme complex[3] upregulated in most cancers[4]. Salvage pathways convert preformed ribonucleosides, deoxyribonucleosides, and nucleobases into nucleotides through the actions of metabolic kinases and phosphoribosyltransferases[2]. Amongst nucleoside salvage kinases, deoxycytidine kinase (dCK) has the broadest substrate specificity, encompassing both purine and pyrimidine nucleosides[5]. While tumors are thought to predominantly rely on *de novo* pathways to produce nucleotides[6], scavenging of preformed nucleosides via dCK and other salvage kinases may also play important roles in the economy of nucleotide metabolism in cancer cells. Many of the cell lines included in the Cancer Cell Line Encyclopedia (CCLE)[7,8] express dCK at higher levels than the corresponding normal tissues (Supplementary Fig. 1a and 1b). Increased tumor dCK expression relative to matched normal tissues also occurs in patient samples, as evidenced by RNASeq data from The Cancer Genome Atlas (TCGA, http://cancergenome.nih.gov; Supplementary Fig. 1c)[9,10]. Moreover, *in vivo*, cancer cells often encounter limited supplies of essential *de novo* pathway substrates, e.g. glucose, glutamine and aspartate, because of their avid consumption of these nutrients and inadequate vascularization[11]. An insufficient *de novo* biosynthetic capacity, coupled with an increased demand for dNTPs due to unabated proliferation driven by oncogenic signaling, might increase the dependency of certain tumors on salvage pathways for nucleotide production. Consistent with this hypothesis, we previously showed that acute lymphoblastic leukemia (ALL) cells

display nucleotide biosynthetic plasticity[12], defined as the ability to compensate for the inhibition of either *de novo* or salvage pathways by upregulating the alternate pathway. These metabolic transitions occurred both *in vitro* and *in vivo*; moreover partial inhibition of both *de novo* and salvage biosynthetic routes was required for therapeutic activity in animal models of T and B-ALL[12].

Collectively, these results described above suggest that, in acute leukemia, and potentially in other cancers, nucleoside salvage biosynthetic pathways may be metabolic non-oncogene addictions[13] targetable by specific inhibitors. However, since both *de novo* and salvage biosynthetic pathways also operate in normal cells[14,15], a better understanding of the signaling mechanisms that regulate their activity in cancer cells may lead to the development of more effective targeted therapies. In this context, the mTOR[16–18], Myc[19,20] and Ras[21] pathways have been shown to regulate nucleotide biosynthesis. The replication stress response pathway, constitutively upregulated in many tumors, also plays important roles in regulating nucleotide metabolism, given its unique ability to 'sense' dNTP insufficiency[22]. The most proximal enzyme in the cellular response to replication stress is ataxia telangiectasia and Rad3-related protein (ATR), a serine threonine kinase activated at stalled replication forks[23] in response to nucleotide insufficiency and other replication defects. In addition to its well-established role in regulating origin firing and promoting fork stability[24], ATR has been recently linked to nucleotide metabolism. Inhibition of ATR, or of its downstream effector kinases CHEK1 and WEE1, reduces dNTP levels in multiple cancer cell lines[25]. This effect of ATR inhibition was proposed to involve the downregulation of the small RNR subunit RRM2, particularly at the G1/S transition[26], when cells are most susceptible to nucleotide insufficiency[27]. Intriguingly, ATR also regulates dCK activity in several solid tumor and myeloid leukemia cells by phosphorylation at serine 74[28]. This post-translational modification (PTM) modulates dCK's catalytic properties and substrate specificity[29,30]. While collectively these findings support a connection between ATR signaling and dNTP production, the metabolic consequences of ATR inhibition in malignancies with

nucleotide biosynthetic plasticity are yet to be defined. Here, we examined ATR modulation of dNTP synthesis and utilization for DNA synthesis, and the consequences for tumor cell viability in culture and *in vivo* in ALL models, using quantitative approaches. A targeted multiplexed mass spectrometric (MS) assay was developed to measure the differential contributions of the *de novo* and salvage pathways both to nucleotide pools and newly replicated DNA. This assay was used in conjunction with proteomic and phosphoproteomic MS approaches to investigate the mechanisms responsible for alterations in nucleotide biosynthesis induced by ATR inhibition. In addition, we compared direct targeting of *de novo* and salvage rate-limiting enzymes, using specific inhibitors versus indirect inhibition of these enzymes via interference with ATR signaling. These studies identified a synthetically lethal interaction between inhibition of convergent nucleotide biosynthetic routes and ATR in ALL. This combination is therapeutically exploitable *in vivo*, resulting in long-term, disease-free survival in a systemic p185$^{BCR\text{-}ABL}$*Arf*$^{-/-}$ pre-B-ALL mouse model representative of the human disease[31–33]. Overall, our findings suggest that nucleotide biosynthetic plasticity in lymphoblastic leukemia cells, and potentially in other malignancies, is mediated by both ATR signaling and nucleotide metabolic adaptive mechanisms which may be targetable without overt toxicity to normal tissues, using existing small molecule inhibitors.

METHODS AND MATERIALS

Cell culture and culture conditions. Leukemia cell lines: CCRF-CEM, EL4, Jurkat, Molt-4, CEM-R, THP-1, HL-60, TF-1, MV-4-11, HH, HuT 78, K-562; ovarian cancer cell lines: Hey-T30, PA-1, Caov-3, OVCAR-5, IGROV-1, A2780; hepatocellular carcinoma (HCC) cell lines: SNU-475, PRC/PRF/5, SNU-449, Hep 3B, Hep G2, SK-HEP-1; and pancreatic adenocarcinoma (PDAC) cell lines: L3.BP1, KPC, BxPC-3, MIA PaCa-2, Hs 766T, AsPC-1, PANC-1 were obtained from American Type Culture Collection (ATCC). Nalm-6 and p185$^{BCR\text{-}ABL}$Arf$^{-/-}$ pre-B cells were gifts from M. Teitell (UCLA) and N. Boulos (CERN Foundation), respectively. Patient-derived primary cells of leukemia COG332 was gift from Yong-Mi Kim (USC). Patient-derived primary cells of glioblastoma (HK-374) and melanoma (M299 and M417) were derived in the labs of Drs. Kornblum (UCLA) and Ribas, respectively. With a few exceptions, cell lines were cultured in RPMI-1640 (Corning) containing 10% fetal bovine serum (FBS, Omega Scientific) and were grown at 37 ºC, 20% O_2 and 5% CO_2. p185$^{BCR\text{-}ABL}$Arf$^{-/-}$ pre-B cells were cultured in RPMI-1640 containing 10% FBS and 0.1% β-mercaptoethanol. HK374 was cultured in DMEM-F12 (Invitrogen) containing B27 supplement (Life Technologies), 20 ng/mL basic fibroblast growth factor (bFGF; Peprotech), 50 ng/mL epidermal growth factor (EGF; Life Technologies), penicillin/streptomycin (Invitrogen), Glutamax (Invitrogen), and 5 µg/mL heparin (Sigma-Aldrich). All cultured cells, except HK374, were incubated in antibiotic free media and were regularly tested for mycoplasma contamination using MycoAlert kit (Lonza) following the manufacturer's instructions, except that the reagents were diluted 1:4 from their recommended amount.

Cell cycle synchronization. Cells were treated with a CDK4/6 inhibitor, Pablociclib or PD-0332991 (Selleckchem, S1116) for 18 h to synchronize them in the G1 phase. Subsequently, cells were washed twice with PBS containing 2% FBS (Omega Scientific) and released into fresh media.

Proliferation assays. Cells were plated in 384-well plates (1,000 cells/well for suspension cell lines and 500 cells/well for adherent cell lines in 30 µL volume). For suspension cells, the plates were incubated at 37 ºC for 1 h to allow settling. For adherent cell lines, the plates were incubated at 37 ºC overnight to allow the cells to seed. Drugs were serially diluted to the desired concentration and an equivalent amount of DMSO was used in vehicle control. After pre-incubation, 10 µL of the diluted drugs were added to each well. Following a 72 h incubation, CellTiter-Glo reagent was added to each well according to manufacturer's instructions (Promega, CellTiter-Glo® Luminescent Cell Viability Assay). The plates were shaken for 2 min,

incubated in the dark for 8 min, and then analyzed by SpectraMax luminometer (Molecular Devices).

Isotopic labeling in cell culture. Cells were transferred into RPMI-1640 without glucose and supplemented with 10% dialyzed FBS (Gibco) containing the following labeled substrates: precursors for *de novo* [U-$^{13}C_6$]glucose (Sigma-Aldrich, 389374) at 11 mM; precursors for purine salvage [U-$^{13}C_{10}$,$^{15}N_5$]dA (Cambridge Isotopes, CIL 3896), [$^{15}N_5$]dA (Cambridge Isotopes, NLM-3895), and [$^{15}N_5$]dG (Cambridge Isotopes, NLM-3899) at 5 μM or as indicated; and precursors for pyrimidine salvage: [U-$^{13}C_9$,$^{15}N_3$]dC (Silantes, 124603602) and [U-$^{13}C_{10}$,$^{15}N_2$]dT (Cambridge Isotopes, CNLM-3902) at 5 μM and [$^{15}N_2$]orotate (Cambridge Isotopes, NLM-1048) at indicated concentrations. The cells were incubated for 12 h or as indicated before sample collection and processing.

Western blot. Cells were lysed using RIPA buffer supplemented with protease (ThermoFisher, 78430) and phosphatase (ThermoFisher, 78420) inhibitors, scraped, sonicated, and centrifuged (20,000 x g at 4 ºC). Protein concentrations in the supernatant were determined using the Micro BCA Protein Assay kit (Thermo), and equal amounts of protein were resolved on pre-made Bis-Tris polyacrylamide gels (Life Technologies). Primary antibodies: pS345 CHEK1 (Cell signaling, #2341), pT68 CHEK2 (Cell signaling, #2197), pS139 H2A.X (Millipore, 05-636), clvd. Casp8 (Cell signaling, #8592), clvd. Casp9 (Cell signaling, #9502), clvd. Casp3 (Cell signaling, #9662), clvd. PARP (Cell signaling, #5625), and anti-actin (Cell Signaling Technology, 9470, 1:10,000). Primary antibodies were stored in 5% BSA (Sigma-Aldrich) and 0.1% NaN_3 in TBST solution. Anti-rabbit IgG HRP-linked (Cell Signaling Technology, 7074) and anti-mouse IgG HRP-linked (Cell Signaling Technology, 7076) were used as secondary antibodies. Chemiluminescent substrates (ThermoFisher Scientific, 34077 and 34095) and autoradiography film (Denville) were used for detection.

Drugs. The following drugs were used: Pablociclib (Selleckchem, S1116, 1 μM), VE-822 (ApeXBio, B1381, 1 μM or as indicated), DI-82 (dCKi[2], 1 μM), thymidine (Sigma-Aldrich, T1895, as indicated), hydroxyurea (Sigma-Aldrich, H8627, as indicated), gallium maltolate (Nanoman Industries, CN-GAM-02-1G00-A00, as indicated), 3-AP (ApeXBio, custom, 500 nM or as indicated), Pentostatin (Santa Cruz Biotechnology, sc-204177, 10 μM), forodesine or BCX-1777 (Chemscene, CS-3781, 100 nM), and dasatinib (LC Laboratories, D-3307, 1 nM).

Sequencing of dasatinib-resistant clones. Bone marrow cells were harvested from dasatinib treated mice with disease relapse during sacrifice and cultured in standard culture conditions.

Genomic DNA was collected from resistant cell populations and a 2-step nested PCR strategy was utilized to amplify the human *ABL* kinase domain. PCR products were sequenced and assessed for the presence of T315I mutation.

Melanoma mutation assessment. Exome sequencing for M417 and M299 was performed at the UCLA Clinical Microarray Core on an Illumina HiSeq3000 using the SeqCap EZ Exome Enrichment Kit v3.0 (Roche). Reads were mapped to UCSC hg19 (bwa-mem), deduplicaed (PicardTools), and subjected to base quality score recalibration and realignment around known indels according to the Broad Institute Genome Analysis Toolkit (GATK) Best Practices v3.0. Variants in genes associated with nucleotide biosynthesis were identified using the GATK HaplotypeCaller, and annotated with Oncotator (http://portals.broadinstitute.org/oncotator/).

Mass spectrometry analyses

dNTP sample processing. 0.5 – 1 x 10^6 cells were collected into 1.5 mL microcentrifuge tubes and centrifuged (450 x g, 4 min, 4 ºC). The supernatant was carefully aspirated and the cells were washed twice with 1 mL of cold PBS, followed each time by centrifugation (450 x g, 4 min 4 ºC). The PBS were aspirated. Thereafter, the pellets were treated with 10 µL of 10% trifluoroacetic acid with internal standards (1 µM [$^{15}N_3$]dCMP and [$^{15}N_3$]dCTP, Silantes # 122303802 and # 120303802, respectively) vigorously vortexed for 30 s, and incubated on ice for 10 min. 40 µL of 500 mM ammonium acetate, pH = 9.3, with the same internal standard (1 µM [$^{15}N_3$]dCMP and [$^{15}N_3$]dCTP) was then added and the samples were vigorously vortexed again for 30 s. The samples were centrifuged (14,000 x g, 10 min, 4 ºC) to remove cell debris. The supernatants (~ 40 µL) were transferred into HPLC injector vials. Stock solutions (10 mM) of rCTP, rCDP, dCMP, dCDP, and dCTP (Sigma Aldrich) were prepared individually in water, and stored at –20 ºC before use to generate calibration standards. Calibration standards were prepared and mixed together in water with internal standards (1 µM [$^{15}N_3$]dCMP and [$^{15}N_3$]dCTP) to make working stock concentrations in 100 nM – 100 µM range. Calibration standards were diluted 10-fold into the same nucleotide extraction solution of 10% TFA/500 mM ammonium acetate (1:4, v/v) with internal standards (1 µM [$^{15}N_3$]dCMP and [$^{15}N_3$]dCTP) to give a final concentration in 10 nM – 10 µM. Nucleotide and calibration samples were processed together to minimize variation.

DNA sample processing. Genomic DNA from 0.5 – 1 x 10^4 cells was extracted using the Quick-gDNA MiniPrep kit (Zymo Research, D3021) and hydrolyzed to nucleosides using the DNA Degradase Plus kit (Zymo Research, E2021), following manufacturer-supplied instructions. In the final step of DNA extraction, 50 µL of water was used to elute the DNA into 1.5 mL

microcentrifuge tubes. A nuclease solution (5 µL; 10X buffer/DNA Degradase Plus™/water, 2.5/1/1.5, v/v/v) was added to 20 µL of the eluted genomic DNA in an HPLC injector vial. The samples were incubated overnight at 37 ºC.

Media samples processing. Culture media (20 µL) was collected at the indicated time points. Stock solutions (10 mM) of [U-$^{13}C_{10}$,$^{15}N_5$]dA, and [$^{15}N_3$]dC (Cambridge Isotope Laboratories) were prepared individually in dimethyl sulfoxide (DMSO), and stored at – 20 ºC before use as internal standards. The solutions were diluted to 20 nM in methanol to generate working solutions. Calibration standards were prepared by spiking working stock solutions of [U-$^{13}C_{10}$,$^{15}N_5$]dA and [U-$^{13}C_9$,$^{15}N_3$]dC with blank media to give concentrations in the 10 nM - 10 µM range. Each 20 µL calibration standard sample was mixed with 60 µL of internal standard solution, mixed for 30 s and centrifuged (15,000 x g, 10 min, 4ºC). After centrifugation, 60 µL of the supernatant was transferred into an HPLC injector vial for LC-MS/MS-MRM analysis. Media samples were processed similarly and in parallel to the calibration standard samples to minimize the experimental variability.

Targeted LC-MS/MS-MRM assays. For genomic DNA and media analysis, an aliquot of the hydrolyzed DNA or media samples (20 µL) were injected onto a porous graphitic carbon column (Thermo Fisher Scientific Hypercarb, 100 x 2.1 mm, 5 µm particle size) equilibrated in solvent A (water 0.1% formic acid, v/v) and eluted (200 µL/min) with an increasing concentration of solvent B (acetonitrile 0.1% formic acid, v/v) using min/%B/flow rates (µL/min) as follows: 0/0/200, 5/0/200, 10/15/200, 20/15/200, 21/40/200, 25/50/200, 26/100/700, 30/100/700, 31/0/700, 34/0/700, 35/0/200. For free nucleotide analysis, a modified version of the same previously reported method[1] was used in which each dNTP lysate sample (20 µL) was injected directly onto the Hypercarb column equilibrated in solvent C (5 mM hexylamine and 0.5% diethylamine, v/v, pH 10.0) and eluted (200 µL/min) with an increasing concentration of solvent D (acetonitrile/water, 50/50, v/v) at the following min/%D/flow rates (µL/min): 0/0/200, 5/0/200, 10/15/200, 20/15/200, 21/40/200, 25/50/200, 26/100/700, 30/100/700, 31/0/700, 34/0/700, 35/0/200. The effluent from the column was directed to the Agilent Jet Stream ion source connected to the triple quadrupole mass spectrometer (Agilent 6460) operating in the multiple reaction monitoring (MRM) mode using previously optimized settings. The peak areas for each nucleosides and nucleotides (precursor→fragment ion transitions) at predetermined retention times were recorded using the software supplied by the instrument manufacturer (Agilent MassHunter).

Quantification. The area for nucleotides measurements were obtained from extracted ion chromatograms of MRM ion transitions. These measurements were normalized from the spiked internal standards ([$^{15}N_3$]dCMP and [$^{15}N_3$]dCTP). A calibration curve was prepared to convert the normalized areas of nucleotides to absolute quantitation, pmol/10^6 cells. For DNA, the area for the hydrolyzed labeled nucleosides were obtained from extracted ion chromatograms of MRM ion transitions. These measurements were normalized to the total ion current at that retention time. To calculate the DNA labeled pmol/10^6 cells, the peak area ratio for a given biosynthetic pathway was multiplied by 1089.3, the dCTP pmol amount needed to replicate the entire genomic DNA from 10^6 cells (assuming the size of the genomic DNA per cell to be 3.2 billion base pair with 41% GC content).

Non-targeted LC-MS metabolic assays. 1 x 10^6 cells were washed with ice-cold 150 mM ammonium acetate twice before adding 1 mL of ice-cold 80% methanol with 10 nM norvaline as an internal standard. After vigorous vortexing, samples were centrifuged at maximum speed, the aqueous layer was transferred to a glass vial and the metabolites were dried under vacuum. Metabolites were resuspended in 50 µL 70% acetonitrile (ACN) and 5 µL of this solution used for the mass spectrometer-based analysis. The analysis was performed on a Q Exactive (Thermo Scientific) in polarity-switching mode with positive voltage 4.0 kV and negative voltage 4.0 kV. The mass spectrometer was coupled to an UltiMate 3000RSLC (Thermo Scientific) UHPLC system. Mobile phase A was 5 mM ammonium acetate (NH_4AcO), pH 9.9, B was acetonitrile and the separation achieved on a Luna 3 mm NH2 100 A column (150 × 2.0 mm, Phenomenex). The flow was 200 µL/min, and the gradient ran from 15% A to 95% A in 18 min, followed by an isocratic step for 9 min and re-equilibration for 7 min. Metabolites were detected and quantified as area under the curve based on retention time and accurate mass (≤ 3 p.p.m.) using the TraceFinder 3.1 (Thermo Scientific). Relative amounts of metabolites between various conditions, as well as percentage of [$^{13}C_6$]glucose labelling, were calculated and corrected for naturally occurring ^{13}C abundance.

Proteomic analyzes. CCRF-CEM cells were treated ± with a CDK4/6 inhibitor, PD-0332991 (Selleckchem) for 18 h to arrest at G1 phase. Cells were then washed twice with PBS and released in fresh media with treatment at a density of 1 x 10^6 cells/mL. Cells were collected at 12 h, washed twice with ice-cold PBS, and lysed by trituration using 1 mL per 5 x 10^7 cells of 0.5% sodium deoxycholate, 12 mM sodium lauryl sarcosine, and 50 mM triethylammonium bicarbonate, pH 8.0. Lysates were heated at 95 ºC for 5 min and water bath sonicated at room temperature (RT) for 5 min. Bicinchoninic acid protein assay (Pierce) was performed to determine protein concentration. Disulfide bridges were reduced with 5 mM tris(2-

carboxyethyl)phosphine (final concentration) at RT for 30 min with subsequent treatment with 10 mM iodoacetamide (final concentration) at RT in the dark for 30 min. Solutions were diluted 1:5 (v:v) with 50 mM triethylammonium bicarbonate. Proteins were cleaved with sequencing grade trypsin (Promega) at 1:100 (enzyme:protein) for 4 h at 37 ºC followed by a second aliquot of trypsin 1:100 (enzyme:protein) overnight at 37 ºC. Samples were acidified with 0.5% trifluoroacetic acid (final concentration), vortexed rapidly for 5 min, and centrifuged (16,000 x g for 5 min, RT) to pellet sodium deoxycholate. Supernatants were transferred to new microcentrifuge tubes and 20 µg of total peptide were desalted using C18 StageTips as previously described[3]. On-column dimethyl labeling using C18 StageTips was performed as previously described[4]. Briefly, StageTips were equilibrated with 20 µL of 250 mM 2-(N-morpholino)ethanesulfonic acid (MES) pH 5.5. Tryptic peptides were dimethyl labeled using 60 mM sodium cyanoborohydride, 0.4% formaldehyde, and 250 mM MES pH 5.5 for 10 min. Dimethyl labeled peptides were eluted from StageTips using 20 µL of 80% acetonitrile with 0.1% trifluoroacetic acid and lyophilized to dryness. Labeled peptides were reconstituted with 2% acetonitrile and 0.1% formic acid (loading buffer). The light, medium, and heavy labeled peptides were mixed 1:1:1 (light:medium:heavy), diluted with loading buffer to a final peptide concentration of 0.2 µg/µL and 1 µg total peptide was analyzed using 180 min data-dependent nLC-MS/MS on Thermo Orbitrap XL as later discussed. Light, medium, and heavy labeled samples were mixed using the protein median ratios as normalization from the “trial” analysis. 48 µg of mixed light, medium, and heavy labeled peptides were sub-fractionated using strong cation exchange (SCX) StageTips as previously described[3]. Briefly, 8 fractions were made using 25, 35, 50, 70, 90, 150, 350, and 750 mM ammonium acetate in 30% acetonitrile and 0.5% acetic acid. Each SCX fraction was desalted using C18 StageTips, vacuum concentrated to 1 µL, and resuspended with 10 µL of loading buffer. 5 µL of each fraction was analyzed using 180 min data-dependent reverse-phase nLC-MS/MS on Thermo Orbitrap XL and Thermo QExactive Plus for synchronous and asynchronous cells, respectively, equipped with Eksigent Spark autosampler, Eksigent 2D nanoLC, and Phoenix ST Nimbus dual column source. Briefly, samples were loaded onto laser-pulled reverse-phase nanocapillary (150 µm I.D., 360 µm O.D. x 25 cm length) with C18 (300 Å, 3 µm particle size) (AcuTech Scientific) for 30 min with mobile phase A (2% acetonitrile and 0.1% formic acid) at 500 nL/min. Peptides were analyzed over 180 min linear gradient of 0-40% mobile phase B (98% acetonitrile and 0.1% formic acid) at 300 nL/min. Electrospray ionization and source parameters for Orbitrap XL were as follows: spray voltage of 2.2 kV, capillary temperature of 200^{o}C, capillary voltage at 35 V, and tube lens at 90 V. Data-dependent MS/MS for Orbitrap XL was operated using the following parameters: full MS from 400-1700 m/z with 60,000 resolution at 400 m/z and target ion count of 3 x 10^5 or fill time of 700 ms, and twelve MS/MS with charge-state screening excluding +1 and unassigned charge

states, isolation width of 2.0 m/z, target ion count of 5,000 or fill time of 50 ms, CID collision energy of 35, and dynamic exclusion of 30 sec. For QExactive Plus, the electrospray ionization and source parameters were as follows: spray voltage of 1.6 kV, capillary temperature of 200^{o}C, and S-lens RF level of 50. Data-dependent MS/MS for QExactive Plus was operated using the following parameters: full MS from 400-1700 m/z with 70,000 resolution at 400 m/z and target ion count of 3 x 10^6 or fill time of 100 ms, and twenty MS/MS with charge-state screening excluding +1 and unassigned charge states, 17,500 resolution at 400 m/z, isolation width of 2.0 m/z, target ion count of 50,000 or fill time of 50 ms, HCD collision energy of 27, and dynamic exclusion of 30 sec. Raw data was searched against Uniprot human database using MaxQuant 1.5.3.30 with standard preset search parameters. Briefly, the search parameters were as follows: 3-plex dimethyl labeling to lysine and peptide N-terminus, trypsin cleavage allowing up to 2 missed cleavages, fixed modification of carbamidomethyl to cysteines, variable modifications of acetylation to protein N-terminus and methionine oxidation, 10 ppm mass error for full MS, 0.5 Da and 20 mmu mass errors for MS/MS for Orbitrap XL and QExactive Plus, respectively, score of 40 or greater for modified peptides, 1% false-discovery rate on peptide and protein identifications, and peptide match between run feature with 1.5 min time window.

Phosphoproteomic analyses. CCRF-CEM cells were prepared same as the asynchronous CEM cells total protein digests above, except that a total of 7.5 mg total protein from 1 x 10^8 cells was collected per treatment condition for phosphoproteomic analysis. tC18 Sep-Pak cartridges (Waters) were used for peptide desalting and Pierce Quantitative Colorimetric Peptide Assay was performed prior to phosphopeptide enrichment. Hydrophilic interaction chromatography (HILIC) and immobilized metal affinity chromatography (IMAC) were performed same as previously described[5]. Data dependent nLC-MS/MS was performed on Thermo QExactive Plus same as above. Raw data was searched against Uniprot human database using MaxQuant 1.5.3.30 with the following search parameters: trypsin cleavage allowing up to 2 missed cleavages, fixed modification of carbamidomethyl to cysteines, variable modifications of acetylation to protein N-terminus, methionine oxidation, and phosphorylation to serine, threonine, and tyrosine, 10 ppm and 20 mmu mass errors for full MS and MS/MS, respectively, score of 40 or greater for modified peptides, and 1% false-discovery rate on peptide and protein identifications. Identified phosphopeptides were manually quantified by area-based extracted ion chromatograms of the monoisotopic peak.

Plasma collection and pharmacokinetic assays. Blood was collected in heparin-EDTA tubes by retro-orbital technique at time points 0.25, 1, 6, and 24 h time points from the first set of mice and 0.5, 4, and 12 h from the second set of mice. Blood samples were spun at 2000 x g for 15

min and the plasma supernatants were collected. All plasma samples were frozen down at –20 ºC before sample processing. The stock solutions of 3-AP, VE-822, DI-82, 3-AP analog (NSC 266749), VE-821 (Selleckchem), DI-39 were prepared individually by dissolving the appropriate amount of each drug in a known volume of dimethyl sulfoxide (DMSO) to a 10 mM concentration and were stored at –20ºC before use. The 3-AP analog, VE-821 and DI-39 (internal standards) were diluted to 200 nM in methanol to make the internal solution. The calibration standards were prepared by spiking working stock solutions of 3-AP, VE-822 and DI-82 in plasma from untreated mice to give 0.01-10 pmol/µL range. Each 20 µL calibration standard sample was mixed with 60 µL of internal solution (methanol with 200 nM internal standards) and vortexed for 30 s. Following centrifugation at 15,000 x g for 10 min, approximately 60 μL of sample was carefully transferred into HPLC injector vials for LC-MS/MS-MRM analysis. Plasma samples were processed the same way as the calibration standard samples. 20 µL samples were injected onto a reverse phase column, (Thermo Scientific Hypersil GOLD column 3.0 μm; 2.1 x 100 mm) equilibrated in water/formic acid, 100/0.1, and eluted (200 µL/min) with an increasing concentration of solvent B (acetonitrile/formic acid, 100/0.1, v/v: min/% acetonitrile; 0/0, 5/0, 15/60, 16/100, 19/100, 20/0, and 25/0). The effluent from the column was directed to the Agilent Jet Stream ion source connected to the triple quadrupole mass spectrometer (Agilent 6460) operating in the multiple reaction monitoring (MRM) mode using previously optimized settings. The following drug precursor→fragment ion transitions were used: 3-AP (196→179), DI-82 (511→369), VE-822 (464→533), VE-821 (369→276), 3AP-analog (199→182), DI-39 (525→383). The peak areas for each drug (precursor→fragment ion transitions) at predetermined retention times were recorded using the software supplied by the instrument manufacturer (Agilent MassHunter).

FACS and flow cytometry analyses

Cell cycle histograms (measurements of DNA content). Cells were plated at a density of 0.5 x 10^6 cells/mL in respective media or drug treated media. Following 24 h incubation, cells were harvested and washed twice with PBS twice before staining with 0.5 ml of propidium iodide (Calbiochem, #P3566, 1 µg/mL) solution containing Ribonuclease A and 0.3% Triton-X 100. The samples were protected from light before acquisition by flow cytometry.

Cell cycle kinetics (pulse chase analysis) and cell cycle progression (synchronous chase pulse analysis) by intracellular detection of DNA-incorporated 5-ethynyl-2-deoxyuridine (EdU). CEM T-ALL cells were plated at a density of 0.5 x 10^6 cells/mL. Cells were pulsed with 10 µM EdU (Invitrogen) for 1 h, washed twice with PBS, and released in fresh media containing

5 μM deoxyribonucleosides, with and without drugs. Cells were collected at different time points following release in fresh media, and then fixed with 4% paraformaldehyde and permeabilized using saponin perm/wash reagent (Invitrogen). Cells were then stained with azide-Alexa Fluor 647 by Click reaction according to manufacturer's protocol (Invitrogen; Click-iT EdU Flow cytometry kit, #C10634). The total DNA content was assessed by staining the samples with FxCycle-Violet (Invitrogen, #F10347) at 1 μg/mL final concentration in PBS containing 2% FBS. To measure the cell cycle progression of a synchronous population of cells, cells were first arrested in the G1 phase following treatment with 1 μM Palbociclib for 18 h, then washed and released in fresh media supplemented with drugs. Before collecting and fixing the cells at different time points, the cells were pulse-labeled with 10 μM EdU for 1 h, and then labeled with azide-Alexa Fluor 647 (Invitrogen; Click-iT EdU Flow cytometry kit). Total DNA content was assessed by staining with FxCycle-Violet (Invitrogen) at 1 μg/mL final concentration in PBS containing 2% FBS.

pH2A.X staining. Cells were harvested, fixed and permeabilized with cytofix/cytoperm (BD biosciences, #554722) for 15 min on ice protected from light. Cells were washed, then resuspended in 100 μL 1X Perm/wash buffer (BD Sciences) and incubated for 15 min on ice. The cells were washed, then resuspended in 50 μL with phospho-Histone H2A.X (Ser139) antibody conjugated to fluorochrome FITC (EMD Millipore, #05-636, 1:800 dilutions in perm/wash) for 20 min in the dark at RT. Subsequently, cells were washed and stained with 0.5 mL of DAPI (Invitrogen, #D1306) for DNA content (1 μg/mL in 2% FBS in PBS) before data acquisition.

Measurement of single stranded DNA (ssDNA) levels using the F7-26 monoclonal antibody. Cells were harvested and fixed with ice-cold methanol:PBS (6:1 v/v) for 24h. Staining with F7-26 monoclonal mouse antibody was performed according to manufacturer's instructions (EMD Millipore, #MAB3299). Fixed cells were resuspended in 250 μL of formamide and heated in a water bath at 75 ºC for 10 min. Cells were then allowed to equilibrate to room temperature and then washed with 2 mL of 1% non-fat dry milk in PBS for 15 min. Subsequently, cells were resuspended in 100 μL of anti-ssDNA Mab F7-26 (EMD Millipore, 1:10 in 5% FBS in PBS) and incubated for 45 min at room temperature. Cells were washed with PBS and stained with 100 μL of fluorescence-conjugated goat anti-mouse IgM antibody (Santa Cruz Biotechnology, #sc-3768, 1:50) for 45 min at room temperature. Cells were then washed with PBS, stained with 0.5 mL of DAPI for DNA content (1 μg/mL in 2% FBS in PBS) before data acquisition.

Phospho-histone 3 staining. Cells were treated with drug combinations of three drugs. 24 h following treatment, cells were fixed and permeabilized with 1% PFA and 1X Perm/wash solution respectively. Following fixation and permeabilization, cells were stained intracellularly with pH3 Ser10 antibody conjugated to AF647 (Cell signaling, #12230). Cells were then washed with PBS, stained with 0.5 mL of DAPI for DNA content (1 µg/mL in 2% FBS in PBS) before data acquisition.

Annexin V staining. Cells were treated with the indicated treatments for 24 or 72 h, then collected and washed twice with 1 mL of FACS buffer (2% FBS in PBS). Induction of apoptosis and cell death were assayed by staining the cells with Annexin V-FITC and PI according to manufacturer's instructions (FITC Annexin V Apoptosis Detection Kit, BD Sciences, #556570).

FACS analysis. All flow cytometry data were acquired on five-laser LSRII cytometers (BD) for analysis, and analyzed using FlowJo software (Tree Star). The cell cycle durations were calculated using equations for multiple time-point measurements according to previously published methods (Terry and White, 2006).

Animal studies. Mice were housed under specific pathogen-free conditions and were treated in accordance with UCLA Animal Research protocol guidelines. All C57BL/6 female mice were purchased from the UCLA Radiation Oncology breeding colony. VE-822 (ApeXBio, 40 mg/kg), 3-AP (ApeXBio, dosage as indicated) and DI-82 (dCKi, Sundia Pharmaceuticals, 50 mg/kg) were administered by intraperitoneal (i.p.) injections or oral gavage to recipient animals. For oral administration, single agent or combination of drugs were solubilized in a formulation consisting of the following: PEG-200: Transcutol: Labrasol: Tween-80 mixed in 5:3:1:1 ratio. For i.p. administration, the drugs were solubilized in PEG-400 and 1 mM Tris-HCl in a 1:1 (v:v) ratio. Dasatinib (LC Laboratories) was solubilized in 80 mM citric acid (pH 3.1) and was administered at a dose of 10 mg/kg by oral gavage. 2 x 10^5 luciferase expressing $p185^{BCR\text{-}ABL}Arf^{-/-}$ pre-B-ALL cells were injected intravenously into C57BL/6 female mice for leukemia induction. The treatment was started 6 or 7 days after the intravenous inoculation of leukemia initiating cells, when animals had developed a significant leukemic burden as monitored by bioluminescence imaging (IVIS Bioluminescence Imaging scanner). The dosing schedules are indicated in the text and figure legends. The mice were observed daily and those that became moribund during the trials, (paralysis of hind limbs, significant body weight loss) were sacrificed immediately. Kaplan-Meier curves and bioluminescence quantifications were generated using Prism 6.0h (Graphpad Software).

Bioluminescence imaging (BLI). Mice were anesthetized with 2% isoflurane followed by intraperitoneal injection of 50 µL (50 mg/mL) substrate D-luciferin (Sigma, #L9504). The mice were imaged with the IVIS 100 Bioluminescence Imaging scanner 10 minutes after luciferin administration. All mice were imaged in groups of five with 1-minute exposure time, and the images were acquired at low binning.

Statistical Analyses. Data are presented as means ± SD with indicated biological replicates. Comparisons of two groups were calculated using indicated unpaired or paired two-tailed Student's t-test and *P* values less than 0.05 were considered significant. For some experiments, generated mean normalized values (ratios from two groups, treated to untreated) were compared to the hypothetical value 1 (indicating equal values between treated and untreated), calculated using one-sample t-test, and P values less than 0.05 were considered significant. Comparisons of more than two groups were calculated using one-way ANOVA followed by Bonferroni's multiple comparison tests, and *P* values less than 0.05/*m*, where *m* is the total number of possible comparisons, were considered significant. The Benjamini–Hochberg false discovery rate (FDR) method was used to adjust the *P* values for multiple testing in metabolomic and proteomic studies. An FDR q value ≤ 0.2 was used as a threshold for significance. All statistical analysis and generated graphs were performed either in R or Graphpad Prism 6.0h.

The rates of dCTP incorporation into the DNA were determined using linear regression with procedure GLM in SAS (v. 9.4). DNA % label was transformed using a shifted log addition of 1 due to the presence of zeros in the data set. Rates were calculated using the slope of the regression line for the log transformed data and are presented in the table with the associated standard errors, along with the ratio between the rate of incorporation into DNA by the *de novo* and salvage pathways (Table 1).

RESULTS

Inhibition of ATR and dCK impairs G1/S transition in T-ALL cells and alters substrate utilization for dCTP biosynthesis.

Human T-ALL cells CCRF-CEM (subsequently referred to as “CEM”) express dCK and exhibit constitutive phosphorylation of the ATR effector kinase CHEK1 on Serine 345 (pS345, Supplementary Fig. 2a), a marker of replication stress[34]. CHEK1 pS345 levels are reduced following exposure to VE-822, a specific ATR inhibitor[35] (Supplementary Fig. 2a). To investigate whether ATR inhibition increases the dependence of T-ALL cells on dCK activity at the G1/S transition, CEM cells were synchronized in G1 using Palbociclib, a CDK4/6 inhibitor[36,37], and then released from G1 arrest into media containing VE-822 and/or DI-82, a high affinity competitive dCK inhibitor (dCKi) developed by our group[38]. At various time points following G1 release, cells were pulsed for 1 h with 5’-ethynyl-2’-deoxyuridine (EdU) to analyze cell cycle kinetics by flow cytometry. Six hours after release from G1, ~25% of cells in the untreated and single drug treated groups advanced into early S-phase (designated as S1, in blue, Fig. 1a). In contrast, only 16% of cells treated with both VE-822 and dCKi entered S1. Twelve hours after release from G1 arrest, 16% fewer VE-822-treated cells entered the later part of S-phase (designated as S2, in red, Fig. 1b) compared to untreated cells. While at this time point dCK inhibition alone did not affect the number of cells that progressed beyond early S phase, progression to late S-phase was significantly impeded (Supplementary Fig. 2b). Co-inhibition of ATR and dCK decreased the percentage of cells that reached S2 by five-fold relative to untreated cells (Fig. 1b). The effects of ATR inhibition on cell cycle kinetics were partially rescued by nucleotide supplementation, in a dCK-dependent manner (Supplementary Fig. 2c and 2d).

To further investigate the functions of dCK and ATR at the G1/S transition in CEM cells, a non-targeted liquid chromatography mass spectrometry (LC-MS) assay was used to determine the utilization of labeled [$^{13}C_6$]glucose and [$^{13}C_9$,$^{15}N_3$]deoxycytidine, the main substrates for *de novo* and salvage nucleotide biosynthesis, respectively. Of the 166 metabolites identified in CEM cells treated with VE-822 and/or dCKi, 105 metabolites found in all four treatment groups contained glucose-derived ^{13}C atoms. While ATR inhibition did not decrease glucose uptake and labeling of glycolytic intermediates (Supplementary Fig. 3), it significantly decreased glucose utilization for 29 other metabolites (Fig. 1c and Supplementary Table 1). These metabolites included intermediates such as rUTP, rCTP, and rCDP in the *de novo* dCTP biosynthesis (Fig. 1d). These data indicate that ATR inhibition impacts glucose utilization for *de novo* nucleotide biosynthesis. However, several deoxyribonucleotides, including dCTP, were below the limit of detection of the

non-targeted LC-MS approach, raising the concern that the sensitivity of this assay is not sufficient to measure the contribution of the salvage pathway or the ratio of *de novo* and salvage biosynthesis to these pools. To address this problem, a newly developed targeted mass spectrometric assay was developed (Fig. 1e and Supplementary Fig. 4). In this assay, samples containing either extracted dNTPs or hydrolyzed DNA from labeled cells are separated by liquid chromatography for detection by a triple quadrupole mass spectrometer (QQQ) using multiple reaction monitoring (LC-MS/MS-MRM). The first (Q1) and third (Q3) quadrupoles function as mass filters, while the second (Q2) quadrupole serves as a collision chamber (Fig. 1e). For instance, to profile the biosynthetic composition of deoxycytidine (dC) derived from hydrolyzed DNA or dCTP, an intact, protonated dC ion is selected in Q1, followed by fragmentation of the glycosidic bond, which releases in Q2 a protonated nucleobase, cytosine, that is filtered in Q3 and detected to generate an ion chromatogram. The peak areas for the ion chromatograms of salvage [$^{13}C_9$,$^{15}N_3$]dC (red trace), *de novo* [$^{13}C_5$]dC (black trace, from [$^{13}C_6$]glucose) and unlabeled dC (gray trace) (Fig. 1e) are used to determine the relative contributions of the *de novo* and salvage routes both to dCTP pools and to dCTP incorporated into DNA.

Since dCK phosphorylates not only dC but also dA and dG[5], the targeted LC-MS/MS-MRM assay was first used to determine whether, in T-ALL cells, dCK mediates the salvage of multiple deoxyribonucleosides (dNs). However, salvaging of purine dNs via dCK occurred only if the catabolic enzymes which degrade these dNs, adenosine deaminase (ADA) and purine nucleoside phosphorylase (PNP), were inhibited pharmacologically (Supplementary Fig. 5 and 6). Since inactivating mutations in ADA and PNP have been associated with severe combined immunodeficiency[39], but not with cancer, we focused on examining the metabolic fate of dC as the most relevant dCK substrate in ATR-inhibited T-ALL cells for salvage biosynthesis. CEM cells were collected at multiple points after release from Palbociclib-induced G1 arrest into media containing VE-822 and/or dCKi, as well as substrates for the *de novo* and salvage pathways, [$^{13}C_6$]glucose and [$^{13}C_9$, $^{15}N_3$]dC, respectively. At each of the examined time points, free dCTP pools in untreated cells were predominantly synthesized by the salvage pathway from [$^{13}C_9$,$^{15}N_3$]dC via dCK, with only a small contribution from [$^{13}C_6$]glucose via the *de novo* pathway (Fig. 1f). While ATR inhibition alone did not alter free dCTP levels or their biosynthetic origins (e.g. *de novo vs*. salvage), dCKi either alone or in combination with VE-822, nearly eliminated the contribution of the salvage pathway and reduced the amount of free dCTP by ~50% at the 12 h time point.

In contrast to the free dCTP pool, which was predominantly derived from the salvage pathway, dCTP incorporated into newly replicated DNA of CEM cells was produced in equal proportions

by the *de novo* and salvage pathways (Fig. 1g and Table 1). This observation is consistent with previous findings that *de novo* synthesized dCTP is more readily incorporated in DNA than is dCTP synthesized by the salvage pathway[12]. ATR inhibition reduced the DNA incorporation of both *de novo* and salvage produced dCTP, yielding a combined 30% reduction in overall DNA labeling compared to untreated cells at the 12 h time point (Fig. 1g and Table 1). This reduction is consistent with the literature showing replication fork collapse and delays in restarting DNA replication following ATR inhibition in other cell types[40–43]. dCK inhibition abolished the incorporation of salvage produced dCTP into newly replicated DNA and triggered a compensatory increase in the DNA incorporation of *de novo* generated dCTP. This compensatory response was suppressed in cells treated with both VE-822 and dCKi (Fig. 1g and Table 1).

ATR inhibition alters protein and phosphorylation levels of *de novo* and salvage nucleotide biosynthetic enzymes.

To investigate the molecular mechanisms underlying the metabolic consequences of ATR and dCK inhibition, global changes in protein expression were assessed in CEM cells using quantitative nano-liquid chromatography tandem mass spectrometry (nLC-MS/MS) (Fig. 2a). Chemical isotope coding following reductive dimethylation of peptide N-termini and lysine primary amines with differential stable isotopes (light:medium:heavy) was used to compare expression of experimental (VE-822, dCKi, and VE-822 + dCKi) samples to controls (untreated, NT) by mixing equal proportions for triplex nLC-MS/MS quantitative analyses. The proteomics dataset was filtered for proteins identified in all treatment groups in three independent experiments with coefficients of variation <20%. This yielded 1757 proteins with relative fold changes in treated *vs*. untreated cells ranging from 0.45 to 1.83. Of these, about 3% (46 proteins) displayed statistically significant (as determined by one-way ANOVA and false discovery rate cut-offs) fold changes in expression (>20%) in at least one treatment group (Fig. 2b and Supplementary Table 2). Protein levels of both RNR subunits, RRM1 and RRM2, as well as thymidylate synthase (TYMS) decreased by more than 20% following ATR inhibition (Fig. 2c). Changes in the expression of *de novo* enzymes observed in synchronous cells also occurred with ATR inhibition in asynchronous CEM cells (Fig. 2d, Supplementary Table 3), thereby arguing against the possibility of experimental artifacts introduced by Palbociclib-mediated cell cycle synchronization. The reduction in RRM2 protein levels induced by ATR inhibition was accompanied by an ~50% decrease in the phosphorylation of RRM2 on threonine 33 (pT33) (Fig. 2e), a phosphosite previously linked to the stability of the RRM2 subunit[44].

ATR inhibition decreased dNTP levels in several solid tumor-derived cell lines and has been linked to reduced RRM2 levels[26,45]. However, it remains unclear to what degree RRM2 protein levels are rate-limiting for *de novo* dCTP biosynthesis. To further investigate the relationship between RRM2 protein levels and dCTP biosynthesis, we knocked down RRM2 in CEM cells using shRNA (Supplementary Fig. 7a). RRM2 levels in the CEM shRNA^{RRM2} cells were reduced by 35–50%, as determined by quantitative nLC-MS/MS and intracellular flow cytometry analyses (Supplementary Fig. 7a and 7b). The CEM shRNA^{RRM2} cells exhibited approximately 30% lower incorporation of *de novo* synthesized dCTP into newly replicated DNA compared to control cells (Supplementary Fig. 7c); a response comparable with the effects of pharmacological ATR inhibition (Fig. 1g). These findings suggest that the RRM2 regulation by ATR is an important determinant of *de novo* dCTP biosynthesis in T-ALL cells. Since ATR inhibition reduced RRM2 levels by only 20%, it is likely that there are other mechanisms by which ATR regulates *de novo* dCTP biosynthesis. These additional mechanisms could include reduced levels of the large RNR subunit, RRM1 (Fig. 2c and 2d), and/or changes in yet to be identified regulatory PTMs in RRM1 and RRM2 that are modulated directly or indirectly by ATR signaling.

In contrast to the reduced RRM1 and RRM2 levels in response to ATR inhibition, dCK protein levels were not affected (Fig. 2c and 2d). A recent study showed that ATR directly phosphorylates dCK on serine 74 (dCK pS74) to control its activity under replication stress[28]. We therefore quantified the effects of ATR inhibition on the biosynthetic output and phosphorylation status of dCK. Used as a positive control, the dCKi reduced dCK activity, as defined by contribution of labeled [$^{13}C_9$,$^{15}N_3$]dC to intracellular dCMP, by almost 90% (Fig. 2f, left panel). ATR inhibition in CEM cells reduced the dCK-labeled [$^{13}C_9$,$^{15}N_3$]dCMP pool by ~33% compared to untreated cells (Fig. 2f, left panel). The reduction in dCMP biosynthesis following ATR inhibition correlated with a ~36% decrease in dCK pS74 levels (Fig. 2f, right panel). Collectively, these data (summarized in Fig. 2g) show that, in T-ALL cells, ATR regulates *de novo* and salvage nucleotide biosynthetic pathways by diverse mechanisms involving alterations in total protein (ATR) and protein phosphorylation (dCK) levels. Nonetheless, both *de novo* and salvage pathways retain significant activity in ATR inhibited CEM cells and therefore, may allow these cells to survive therapeutic interventions that interfere with ATR signaling.

Effects of the RNR inhibitor 3-AP on *de novo* and salvage dCTP biosynthesis in CEM cells.

To identify the most potent clinically relevant RNR inhibitors that could be used to target the remaining *de novo* nucleotide biosynthetic activity in ATR inhibited CEM cells we evaluated four

compounds, each with a distinct mechanism of action: (3-AP)[46,47], hydroxyurea (HU)[48], gallium maltolate (GaM)[49], and thymidine (dT)[50] (Fig. 3a). Amongst these, 3-AP was the most potent, as indicated by its ability to induce S-phase arrest at concentrations as low as 0.5 μM (Fig. 3b and Supplementary Fig. 8). In contrast, 60 to 100-fold higher concentrations of HU, GaM, and dT were required to induce S-phase arrest. The effects of 3-AP on the utilization of [$^{13}C_6$]glucose and [$^{13}C_5$, $^{15}N_3$]dC for nucleotide biosynthesis in CEM cells were investigated (Fig. 3c), using the targeted LC-MS/MS-MRM assay. 3-AP doubled the rCTP and rCDP pools, likely reflecting an inefficient conversion of these pools to dCDP via RNR. However, the most significant change in 3-AP treated cells occurred downstream of RNR and involved a ~19-fold reduction in the incorporation of *de novo* produced dCTP into newly replicated DNA. Along with its effects on *de novo* biosynthesis, 3-AP triggered a compensatory upregulation of the salvage pathway. Salvage dC nucleotide pools doubled in size following 3-AP treatment, and the incorporation of salvage-produced dCTP into DNA increased by >1.5-fold, thereby providing a potential mechanism of resistance to RNR inhibition by 3-AP (Fig. 3c).

Co-targeting ATR, RNR and dCK in CEM cells induces significant alterations in nucleotide metabolism followed by replication stress overload and caspase-8 mediated apoptosis.

Having identified 3-AP as a clinically relevant and potent RNR inhibitor that can be used to directly target the remaining *de novo* activity in ATR treated T-ALL cells, we next quantified the impact of combined ATR, dCK and RNR inhibition on the *de novo* and salvage dCTP biosynthesis in asynchronous CEM cells (Fig. 4a and Supplementary Table 4). ATR inhibition decreased the [$^{13}C_6$]glucose labeling of the rCDP pool by 40% (Fig. 4a, rCDP panel), an effect similar to that observed in the synchronous model (Fig. 1d). In contrast, RNR inhibition increased the size of the rCDP pool (Fig. 4a, rCDP panel, 3-AP). While neither ATR nor RNR inhibition alone had a statistically significant impact on the *de novo* contributions to the dCDP, dCMP and dCTP pools, these pools were nearly abolished when both ATR and RNR were inhibited simultaneously. However, the salvage biosynthetic contributions to the dCMP, dCDP and dCTP pools remained substantial in the absence of the dCKi. In fact, RNR inhibition, alone or combined with ATR inhibition, increased the salvage contributions to the dCMP, dCDP, and dCTP pools by approximately two-fold, indicative of a compensatory mechanism. dCK inhibition abolished this adaptive mechanism to augment these deoxyribonucleotide pools. Consequently, the rate of dCTP incorporation into newly replicated DNA was lowest when all three enzymes were inhibited (Fig. 4a, DNA panel).

Persistent nucleotide insufficiency triggers replication stress characterized by the accumulation of single-stranded DNA (ssDNA) at stalled replication forks, which progresses to DNA double stranded breaks (DSBs)[51]. To investigate these events following ATR, dCK, and RNR inhibition, we used flow cytometry and antibodies against ssDNA[52] as an indicator of replication stress, and phosphorylated histone H2A.X on serine 139 (pH2A.X) as an indicator of DNA damage (Fig. 4b). RNR inhibition by 3-AP increased the percentage of $ssDNA^+$ cells by more than two-fold as early as 0.5 h after treatment, and by greater than three-fold at the 4 h time point. Combined inhibition of ATR and dCK also increased the $ssDNA^+$ and $ssDNA^+;pH2A.X^+$ cell populations at the 0.5 and 4 h time points. Addition of an RNR inhibitor resulted in a rapid and massive (>12-fold) expansion of $ssDNA^+$ population at the 0.5 h time point compared to untreated cells, an effect which was further amplified at the later time point (Fig. 4b). Along with these changes, RNR inhibition triggered rapid induction of CHEK1 pS345, a direct downstream target of ATR (Fig. 4c). This PTM was abrogated by VE-822 treatment at the 0.5 h time point and partially inhibited at the 4 h time point. The rebound in CHEK1 pS345 expression at the 4 h time point was likely mediated by the ATR related kinase, ataxia telangiectasia mutated (ATM), which also phosphorylates CHEK1 on serine 345[53]. ATM was activated in cells treated with the triple combination therapy, as indicated by an increase in phosphorylation of CHEK2 on threonine 68 (pT68, Fig. 4c); a direct target of activated ATM. The induction of CHEK2 pT68 in cells treated with the triple combination therapy coincided with an increase in the $pH2A.X^+$ population (Fig. 4b) and with cleavage of the apoptotic markers caspase 8 (but not caspase 9), caspase 3, and Poly (ADP-ribose) polymerase (PARP) (Fig. 4c). Consistent with these observations, co-targeting ATR, dCK, and RNR resulted in the highest percentage of apoptotic cells, as measured by Annexin V staining (Supplementary Fig. 9a). The cytotoxic effect of ATR inhibitors has been attributed to the induction of premature mitotic entry of cells undergoing DNA replication, an event that exacerbates the level of replication stress and DNA damage[54,55]. Consistent with this model, ATR inhibition increased the percentage of S-phase CEM cells with phosphorylation of histone 3 on serine 10 (H3 pS10), a marker for mitotic kinase activation. This effect was significantly amplified in the triple combination therapy and correlated with the induction of apoptosis (Supplementary Fig. 9b).

ATR inhibition alone is marginally effective in a systemic primary B-ALL mouse model. To investigate the *in vivo* efficacy and tolerability of co-targeting alternative nucleotide biosynthetic pathways and ATR, we used a previously described primary *BCR-ABL*-expressing *Arf*-null pre-B ($p185^{BCR\text{-}ABL}Arf^{-/-}$) model which is difficult-to-treat and thought to be representative of the human disease[31,33]. When compared with 31 cancer cell lines of different origins, $p185^{BCR\text{-}ABL}Arf^{-/-}$ cells were amongst the most sensitive to ATR inhibition by VE-822, with an IC_{50}

value of ~300 nM (Fig. 5a). However, despite its high potency in culture against pre-B-ALL cells, VE-822 alone was only marginally efficacious *in vivo*. C57BL/6 mice inoculated with luciferase expressing p185$^{BCR\text{-}ABL}$*Arf*$^{-/-}$ cells succumbed to disease within 17 days; all VE-822 treated mice died of leukemia within 38 days after inoculation (Fig. 5b–d). We then investigated whether targeting the activities of *de novo* and salvage pathways can improve the efficacy of ATR inhibition in p185$^{BCR\text{-}ABL}$*Arf*$^{-/-}$ cells. Similar to the findings in the human T-ALL cells, targeting these biosynthetic pathways along with ATR was necessary to achieve maximal induction of cell death (Fig. 5e) and complete inhibition of cell growth (Supplementary Fig. 10a and 10b).

Co-targeting ATR, dCK, and RNR is well-tolerated and promotes long-term survival in a systemic primary B-ALL mouse model.

To translate the above cell culture findings into an *in vivo* setting, we first developed a new drug formulation consisting of PEG-200, Transcutol, Labrasol, and Tween-80 blended in a ratio of 5:3:1:1 to solubilize three different drugs (3-AP, VE-822, and dCKi) and achieve therapeutically relevant plasma concentrations via oral delivery (Fig. 6a). Based on the observed plasma pharmacokinetic parameters, 3-AP and dCKi were administered twice/day while VE-822 was administered once/day (Fig. 6b). Treatment was initiated on day 7 post-inoculation of pre-B-ALL when all mice showed evidence of systemic disease, as indicated by whole body bioluminescence imaging (BLI, Fig. 6c, top row, right panel). While mice in the control group succumbed to disease within 17 days, mice in the combination treatment group had significantly lower disease burden on day 17 (Fig. 6c and 6d). All treated mice remained disease-free for 442 days after treatment withdrawal, 42 days post-inoculation of pre-B-ALL (Fig. 6e). The combination therapy was well-tolerated, as indicated by maintenance of body weight during treatment (Fig. 6f) and long term survival (over 1 year and currently ongoing) without any detectable pathology. We also assessed the efficacy of the combination therapy when all 3 components were administered once daily. Although this therapeutic scheme appeared to be slightly less efficacious than the twice/day schedule for 3-AP and dCKi, it was well tolerated and four out of five mice had no detectable disease 313 days after treatment withdrawal (Supplementary Fig. 11). Importantly, removing the dCKi from the combination therapy significantly reduced the therapeutic efficacy *in vivo* (Supplementary Fig. 12), a result consistent with cell culture findings (Fig. 4, Fig, 5e, Supplementary Fig. 9 and 10).

While BCR-ABL tyrosine kinase inhibitors are becoming standard care for patients with Philadelphia chromosome positive ALL[56], therapeutic resistance in pre-B-ALL is common and is caused by the rapid emergence of the T315I BCR-ABL kinase domain (“gatekeeper”) mutation which renders this class of kinase inhibitors ineffective[32,56]. To test the combination of VE-822,

dCKi, and 3-AP against kinase inhibitor resistant ALL we generated p185$^{BCR\text{-}ABL}$*Arf*$^{-/-}$ T315I mutant cells by exposing the leukemia bearing mice to dasatinib and harvesting drug-resistant cells from bone marrow (Supplementary Fig. 13a–c). Mice were inoculated with the T315I-positive cells and treated with the combination therapy (Supplementary Fig. 13d–g). The combination therapy was effective against the highly aggressive dasatinib resistant *in vivo* pre-B-ALL model with 13 of 20 mice being disease-free over 365 days post-inoculation of leukemia cells (Supplementary Fig. 13). To determine whether mice that did not achieve complete remissions harbor ALL cells that have acquired resistance to the triple combination, we harvested leukemia cells from the bone marrow of the moribund mice. These cells were then used to test the efficacy of the combination treatment in cell culture, and compare it with the original dasatinib-resistant p185$^{BCR\text{-}ABL}$*Arf*$^{-/-}$ pre-B-ALL cells. The harvested leukemia cells responded to the combination treatment as well as did the parental cells (Supplementary Fig. 14). One potential reason for the incomplete response in some of the treated mice is the rapid engraftment of p185$^{BCR\text{-}ABL}$*Arf*$^{-/-}$ T315I+ pre-B-ALL cells in the brain coupled with the suboptimal penetrability of 3-AP and potentially, dCKi across the blood-brain-barrier.

DISCUSSION

Here we show that ATR inhibition in leukemia cells reduces the output of both *de novo* and salvage pathways. However, significant remaining activities of both pathways were sufficient to prevent ATR inhibition-induced DNA replication shutdown in cell culture, and were sufficient to permit disease-induced lethality in a systemic mouse model of pre-B-ALL. Combining ATR inhibition with specific inhibitors of *de novo* (RNR) and salvage (dCK) rate-limiting enzymes led to rapid accumulation of ssDNA, a hallmark of replication stress[22], followed by extensive DNA damage, caspase-8 and PARP cleavage, and apoptosis. This synthetically lethal combination therapy was well-tolerated *in vivo* and promoted long-term disease free survival in mice with systemic p185$^{BCR\text{-}ABL}$*Arf*$^{-/-}$ pre-B-ALL, as well as in a mouse model of targeted-therapy (dasatinib) pre-B-ALL resistance. Collectively our results quantify the control exerted by ATR on convergent nucleotide biosynthetic routes, and provide the rationale to co-target both signaling (ATR) and metabolic (RNR and dCK) mechanisms in acute leukemia for optimal therapeutic efficacy.

In mammalian cells dCTP and other dNTPs are present in low concentrations (1-50 pmol of dCTP/10^6 cells); amounts far below those required to complete one round of genome duplication (~1089 pmol of dCTP/10^6 cells)[14,57]. This apparent discrepancy between dNTP supply and demand can be explained by a model in which dNTP production is tightly coupled with utilization for DNA synthesis – an “on demand” model. A key prediction of this model is that even small disruptions of dNTP production could significantly impact DNA integrity, unless the demand for dNTPs is reduced by preventing new origin firing, a process regulated by ATR and its effector kinases[43]. This prediction is supported by the synthetic lethality observed with ATR inhibition and pharmacological targeting of the *de novo* and salvage pathways observed in cell culture (Fig. 5e, Supplementary Fig. 9, 10, and 14) and *in vivo* (Fig. 6c–f, Supplementary 11–13). These findings also suggest that more accurate estimates of the nucleotide biosynthetic capacity of cancer cells should account both for alternative free nucleotide pools and for their potential differential accessibility for substrates that are incorporated into replicated DNA (Fig. 1e–g, Fig. 3c, and Fig. 4a).

To what extent are our findings of differential utilization of *de novo* and salvage pathways in leukemia applicable to solid tumors? An examination of three patient-derived primary cells point to significant nucleotide biosynthetic diversity in solid tumors (Supplementary Fig. 15a). HK-374 glioblastoma multiforme (GBM) cells[58] preferentially use the *de novo* pathways to generate most of their dATP, dGTP, and dCTP pools, with only the dTTP pool displaying a significant salvage

component. A distinct nucleotide biosynthetic profile is present in two melanoma patient-derived primary cells, M299 and M417 (Supplementary Fig. 15a). In M299 cells, the salvage contribution to all four dNTPs exceeds 50%. Except for dATP, a similarly increased reliance on salvage biosynthesis was evident in M417 cells (Supplementary Fig. 15a). In contrast, *de novo* pyrimidine biosynthesis is almost completely absent in M417 cells, with greater than 98% of the dTTP and dCTP pools originating from salvage pathways. Stable isotope labeling studies using [$^{15}N_2$]orotate show that both M417 and M229 patient-derived primary cells efficiently used this substrate to produce dCTP, thereby suggesting a block in *de novo* pyrimidine biosynthesis in M417 cells either at the level of carbamoylphosphate synthetase II (CAD) or at the level of dihydroorotate dehydrogenase (Supplementary Fig. 15b and 15c). Indeed, M417 cells were subsequently found to harbor a homozygous nonsense mutation (Q140*) in CAD (Supplementary Fig. 15d). Predictably, the defect in *de novo* pyrimidine biosynthesis rendered M417 cells hypersensitive to dCK inhibition (Supplementary Fig. 15e). Confirmation of these findings in larger panels of cell lines and patient derived primary samples would provide the rationale for developing new metabolically targeted therapies and clinically applicable biomarkers to define specific nucleotide biosynthetic subtypes (e.g. predominant *de novo*, predominant salvage, and both *de novo* and salvage) in solid tumors. Such biomarkers could be provided by Positron Emission Tomography (PET) imaging using new probes for nucleotide metabolism developed by us[59,60] as well as by others[61].

Post-translational regulation and modifications (PTMs) can have profound and dynamic effects on the activity of metabolic networks[62]. Both dCK[30] and RRM2[44,63] contain multiple PTMs. Among the four phosphorylation sites reported for dCK[30], phosphorylation on serine 74 (pS74) is an important determinant of dCK substrate specificity and catalytic activity[29]. Both ATR and ATM have been reported to phosphorylate dCK on S74 in response to replication stress and DNA damage respectively[28,64]. Our data show that the ATR inhibitor VE-822 reduces dCK activity by ~33%, an effect likely attributed to a two-fold decrease in dCK pS74 (Fig. 2f). However, it remains unknown what kinases are responsible for the remaining dCK pS74 present in VE-822 treated leukemia cells. ATM is a potential candidate, given that phosphorylation of CHEK2 on T68 is detected in ATR inhibited cells (Fig. 4c). Further studies are needed to confirm this hypothesis. In this context, it may also be informative to analyze the activity of dCK following ATR inhibition in tumors harboring inactivating mutations in ATM[65–67]. Concerning RNR regulation, the observed consequences of ATR inhibition in T-ALL cells include the following: a decrease in RRM2 protein levels (Fig. 2c and 2d), reduced RRM1 protein levels (Fig. 2c and 2d), and a significant reduction in RRM2 pT33 (Fig. 2e), a CDK-mediated phosphorylation event which promotes RRM2 proteasomal degradation via interactions with the $SCF^{Cyclin\ F}$ ubiquitin

ligase complex[44]. It is currently unknown whether the reduction in RRM2 levels by ATR inhibition in leukemia cells occurs via a post-translational mechanism concerning protein stability and/or by a transcriptional mechanism downstream of E2F family members[68,69]. Moreover, further studies are needed to determine the significance of the observed reductions in RRM1 protein levels following ATR inhibition (Fig. 2c and 2d) and to identify the mechanism responsible for this effect.

Our results provide quantitative insights into alterations of nucleotide biosynthetic pathways induced in leukemia cells by inhibiting ATR and rate-limiting *de novo* (RNR) and salvage (dCK) enzymes. These findings support a new therapeutic strategy that uses existing inhibitors to exploit the dependency of leukemia cells on intact *de novo* and salvage biosynthetic pathways and replication stress response mechanisms. This strategy fits within the concept of targeting non-oncogene addiction proposed by Elledge and colleagues[13]. Further refinements in this strategy and expanding its applicability beyond leukemia may come from follow-up studies to define clinically applicable companion biomarkers capable of delineating nucleotide biosynthetic and replication stress subtypes that are predictive of responses in human tumors.

FIGURES

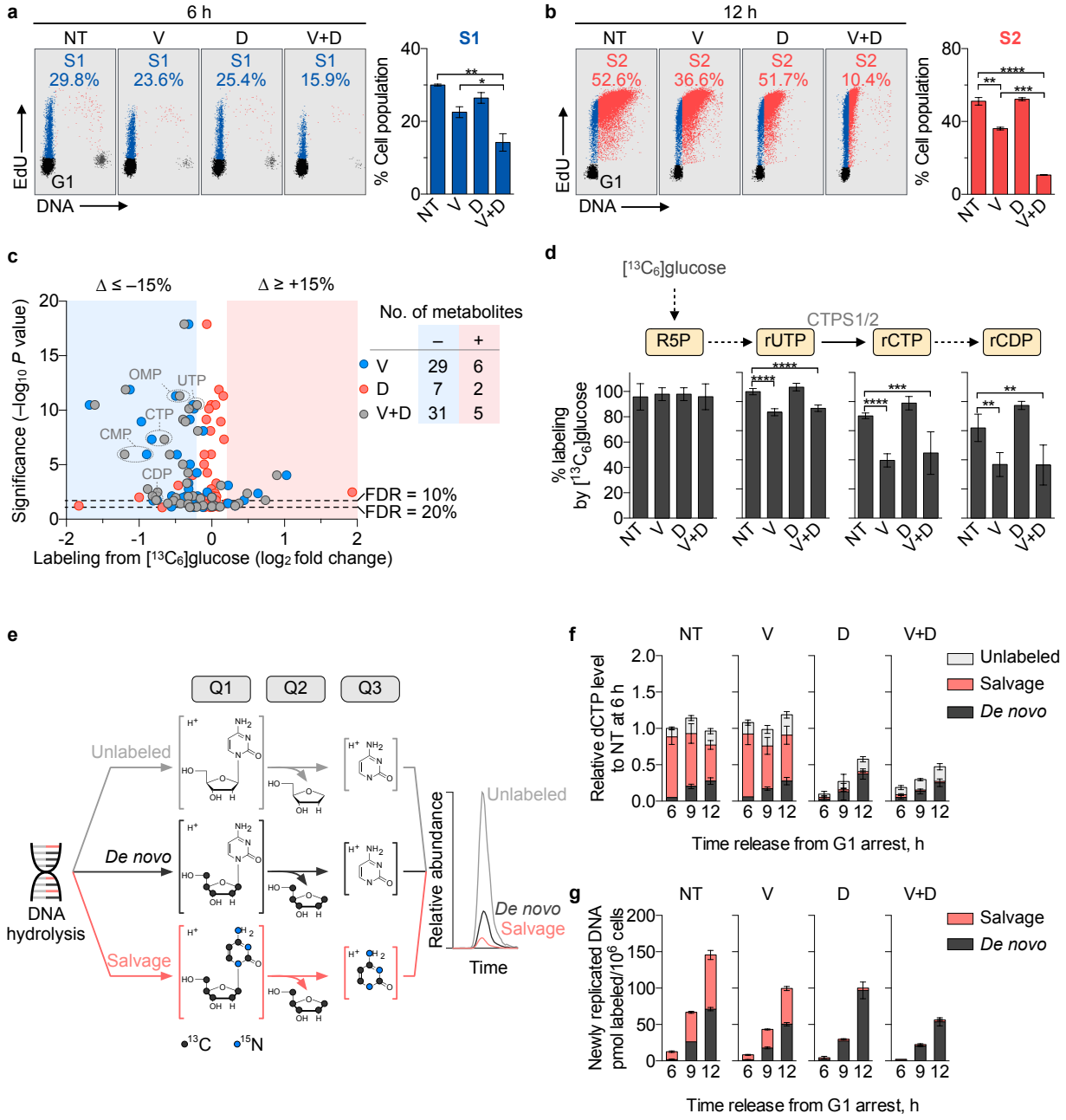

Fig. 1.1. Effects of ATR and dCK inhibition on G1-S transition and substrate utilization for dCTP biosynthesis. (a and b) Flow cytometry analysis of EdU incorporation in CEM T-ALL cells treated with VE-822 (1 μM) and/or dCKi (DI-82,1 μM) for 6 **(a)** and 12 h **(b)** following release from G1 arrest, respectively. Bar graphs summarize the percentage of cell populations

in S1 (early S-phase) and S2 (mid to late S-phase) at 6 and 12 h (mean ± s.d., n = 2, one-way ANOVA, Bonferroni corrected). Plots are representative of two independent experiments. **(c)** Comparison of metabolite labeling by [$^{13}C_6$]glucose in CEM T-ALL cells treated with VE-822 and/or dCKi for 12 h following release from G1 arrest. Number of metabolites exhibiting alterations in [$^{13}C_6$]glucose labeling greater than 15% with significance at a false discovery rate (FDR) ≤ 20% are indicated. **(d)** Percent glucose labeling of ribonucleotides intermediates in the *de novo* dCTP biosynthesis (mean ± s.d., n = 6, one-way ANOVA, Bonferroni corrected). **(e)** Workflow for targeted LC-MS/MS-MRM analysis of dCTP incorporated into newly replicated DNA using a triple quadrupole mass spectrometer (QQQ). See text for details and Supplementary Fig. 4 for the LC-MS/MS-MRM analysis of dCTP pools. **(f and g)** Contributions of the *de novo* and salvage pathways to dCTP pools **(f)** and dCTP incorporated into newly synthesized DNA **(g)** in CEM cells treated with VE-822 and/or dCKi after release from G1 arrest (mean ± s.d., n = 3). Results are representative of two independent experiments.

NT = Not treated, V = VE-822, D = dCKi, V+D = VE-822 + dCKi.

* $P < 0.05$; ** $P < 0.01$; *** $P < 0.001$; **** $P < 0.0001$.

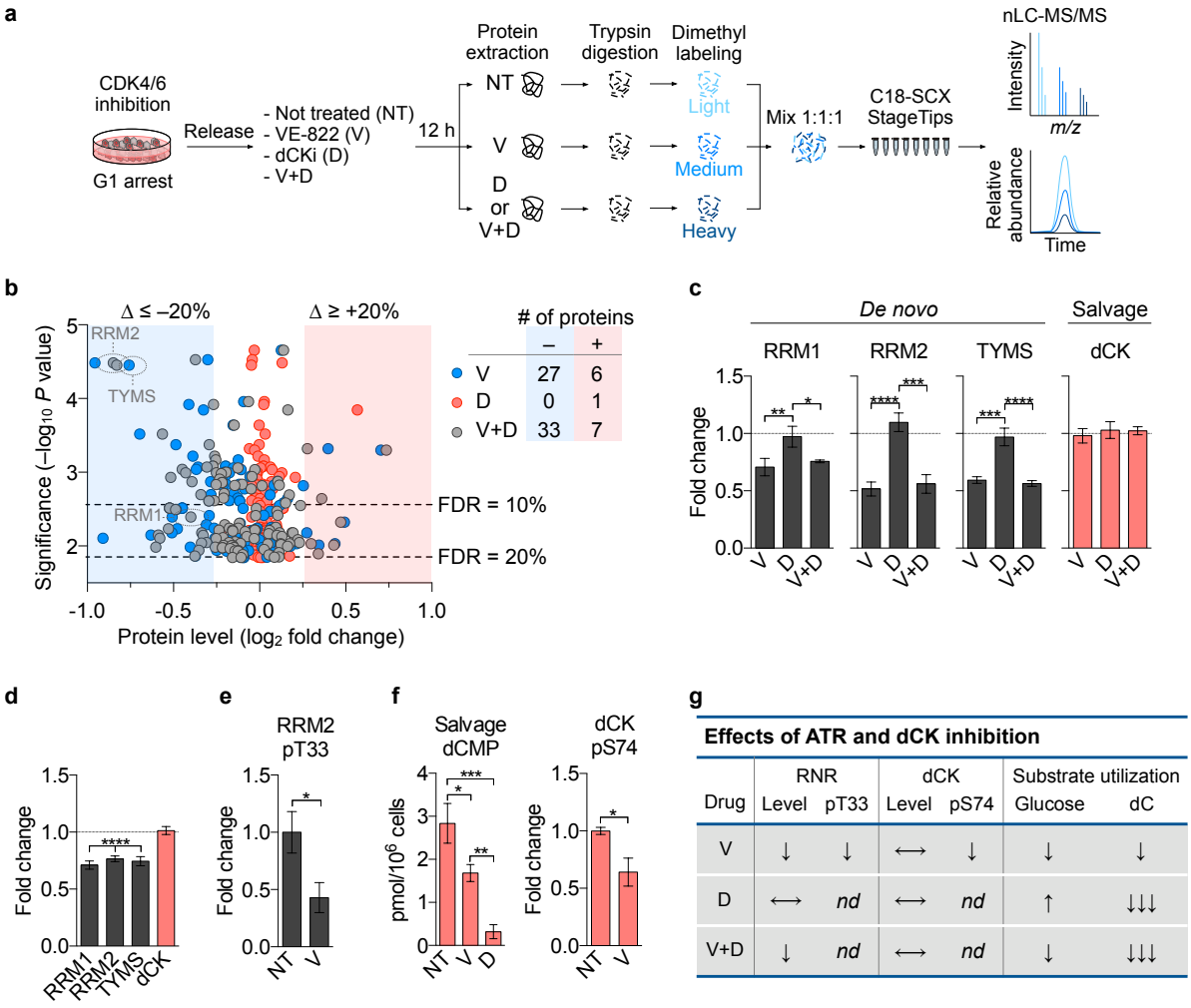

Fig. 1.2. Alterations in total protein and phosphoprotein levels following ATR and dCK inhibition. (a) Workflow for quantitative global proteomics using nLC-MS/MS. See text for details. **(b)** Comparison of protein levels in CEM cells treated with VE-822 and/or dCKi for 12 h following release from G1 arrest. Number of proteins exhibiting fold changes greater than 15% changes with significance at a false discovery rate (FDR) ≤ 20% are indicated. **(c)** Protein levels of nucleotide biosynthetic enzymes (mean ± s.d., n = 3, one-way ANOVA, Bonferroni corrected). **(d)** Protein levels in asynchronous CEM cells treated with VE-822 (1 μM) for 12 h (mean ± s.d., n = 3, one sample t-test to assess if the mean of the protein level normalized to untreated control is equal to one). **(e)** Relative level of RRM2 pT33 normalized to RRM2 protein level from **(d)**, in asynchronous CEM cells treated with VE-822 (1 μM) for 12 h (mean ± s.d., n = 3,

unpaired two-tailed Student's t-test). **(f, left panel)** Salvage produced [$^{13}C_9$,$^{15}N_3$]dCMP in asynchronous CEM cells treated with VE-822 or dCKi for 12 h (mean ± s.d., n = 3, one-way ANOVA, Bonferroni corrected). **(f, right panel)** Relative levels of dCK pS74, after normalized to dCK protein level from **(d)**, in asynchronous CEM cells treated with VE-822 (1 μM) for 12 h (mean ± s.d., n = 3, unpaired two-tailed Student's t-test). **(g)** Summary of the observed effects of ATR and dCK inhibition in CEM cells. ↓ partial decrease/inhibition, ↓↓↓ nearly complete inhibition, ↑ increase, ↔ no change, *nd* not determined.

NT = Not treated, V = VE-822, D = dCKi, V+D = VE-822 + dCKi.

* $P < 0.05$; ** $P < 0.01$; *** $P < 0.001$; **** $P < 0.0001$.

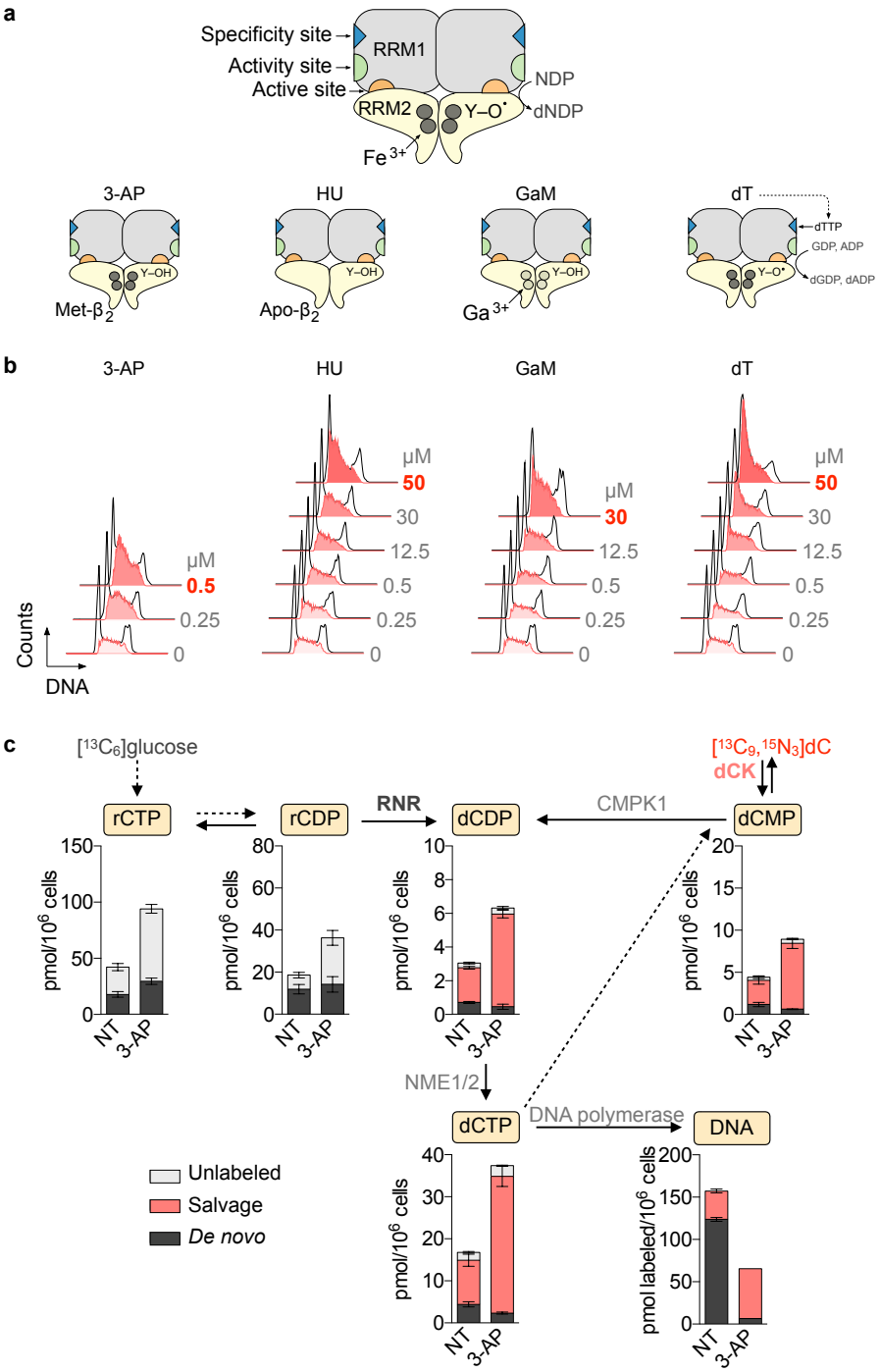

Fig. 1.3. 3-AP potently inhibits RNR and enhances salvage nucleotide biosynthesis. (a) Mechanisms of action of four RNR inhibitors. The two RNR subunits, RRM1 (α) and RRM2 (β) form a catalytically active $\alpha_2\beta_2$ complex. Each RRM1 subunit contains two allosteric regulatory sites (the specificity and activity sites), as well as the active site, where nucleotide reduction

occurs. The active form of the RRM2 dimer (holo-β_2) houses the di-iron cofactor and the tyrosyl radical (Y-O•). 3-AP forms a complex with Fe^{2+} which interferes with the regeneration of the tyrosyl radical in RRM2 therefore promoting the formation of an inactive met-β small subunit which retains its di-iron center[7]. Hydroxyurea (HU) scavenges the RRM2 tyrosyl radical and depletes the di-iron center to form an inactive apo-β form. Gallium maltolate (GaM) releases Ga^{3+} which mimics Fe^{3+} and disrupts the RRM2 di-iron center. Thymidine (dT) is converted via the salvage pathway to thymidine triphosphate (dTTP) which binds to the allosteric specificity site on RRM1 to favor GDP reduction over pyrimidine (CDP and UDP) reduction, thereby resulting in dCTP insufficiency. **(b)** Effects of RNR inhibitors on cell cycle progression. CEM cells were incubated for 24 h with indicated concentrations of RNR inhibitors followed by cell cycle analyses using flow cytometry. Shown in bold red are the concentrations of each RNR inhibitor required to induce a greater than 45% increase in the S-phase population, indicative of S-phase arrest due to nucleotide insufficiency. Cell cycle plots are representative of two independent experiments. See Supplementary Fig. 8 for quantification. **(c)** LC-MS/MS-MRM analysis of dCTP biosynthesis in CEM cells treated with 500 nM 3-AP for 12 h (mean ± s.d., n = 3). NT: not treated.

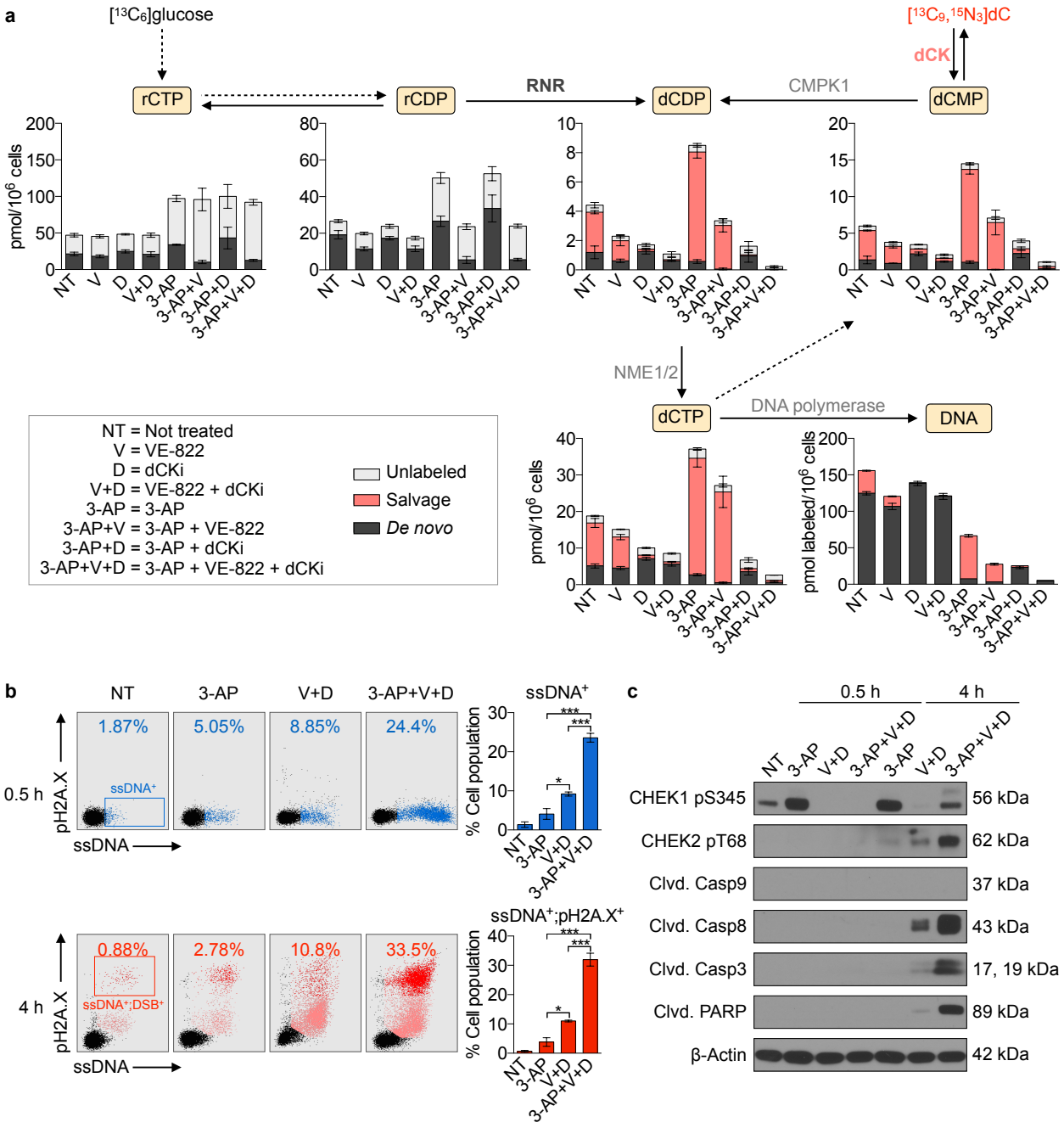

Fig. 1.4. Synthetic lethality induced by combined inhibition of ATR, dCK and RNR. (a) LC-MS/MS-MRM analysis of dCTP biosynthesis in CEM cells treated as indicated in the text for 12 h (mean ± s.d., n = 3). Results are representative of two independent experiments. **(b, left panels)** Flow cytometry analyses of ssDNA (F7-26) and pH2A.X levels in CEM cells treated as

indicated for 0.5 and 4 h. **(b, right panels)** Bar graphs summarizing the percentage of $ssDNA^+$ and $ssDNA^+$;$pH2A.X^+$ cells at 0.5 and 4 h, respectively (mean ± s.d., n = 2, one-way ANOVA, Bonferroni corrected). ssDNA-pH2A.X plots are representative two independent experiments. **(c)** Representative immunoblots of CEM cells treated as indicated in the text for 0.5 and 4 h. * $P < 0.05$; ** $P < 0.01$; *** $P < 0.001$; **** $P < 0.0001$.

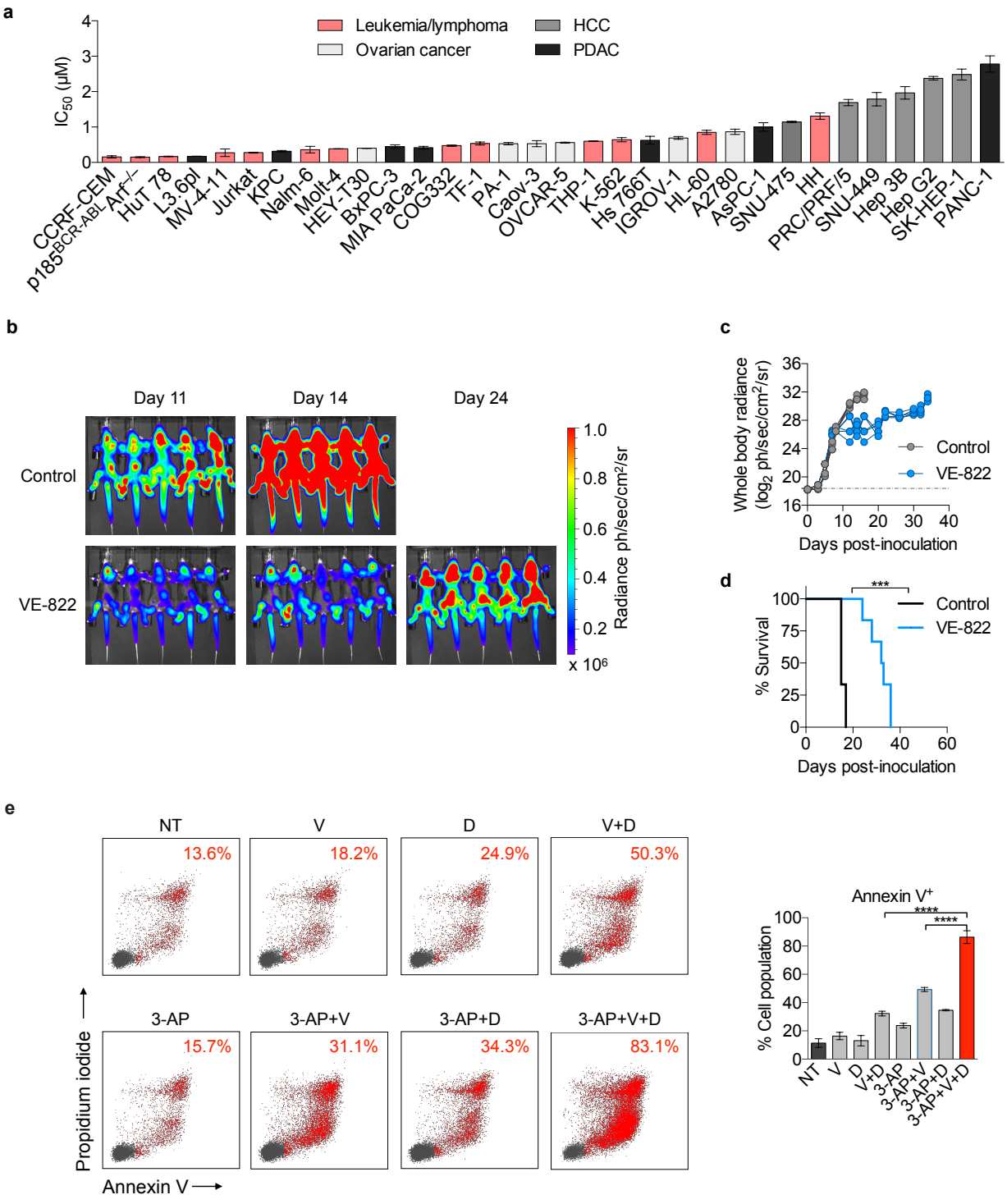

Fig. 1.5. ATR inhibition alone is effective but not sufficient to achieve disease-free survival in a systemic primary B-ALL model. (a) IC_{50} values of VE-822 in a panel of cancer cell lines and patient-derived samples (CellTiter-Glo assay at 72 h, mean ± s.d., n = 3). **(b and c)** Bioluminescence images **(b)** and quantification of whole-body radiance **(c)** of leukemia

bearing mice treated with 40 mg/kg VE-822 (n = 6) or vehicle (control, n = 6). VE-822 was administered once daily. **(d)** Kaplan-Meier survival analysis of C57BL/6 mice bearing p185$^{BCR\text{-}ABL}$*Arf*$^{-/-}$ systemic pre-B-ALL treated with 40 mg/kg/day VE-822 (n = 6) or vehicle (control, n = 6). Median survival for the control group was 15 days after treatment initiation and 32.5 days for the VE-822 group (Mantel-Cox test). **(e)** Apoptosis induction in p185$^{BCR\text{-}ABL}$*Arf*$^{-/-}$ pre-B-ALL cells treated as indicated (350 nM 3-AP, 100 nM VE-822, and 1 μM dCKi) for 72 h using flow cytometry for Annexin V and PI staining (mean ± s.d., n = 2, one-way ANOVA, Bonferroni corrected).

* $P < 0.05$; ** $P < 0.01$; *** $P < 0.001$; **** $P < 0.0001$.

HCC hepatocellular carcinoma; **PDAC** pancreatic ductal adenocarcinoma.

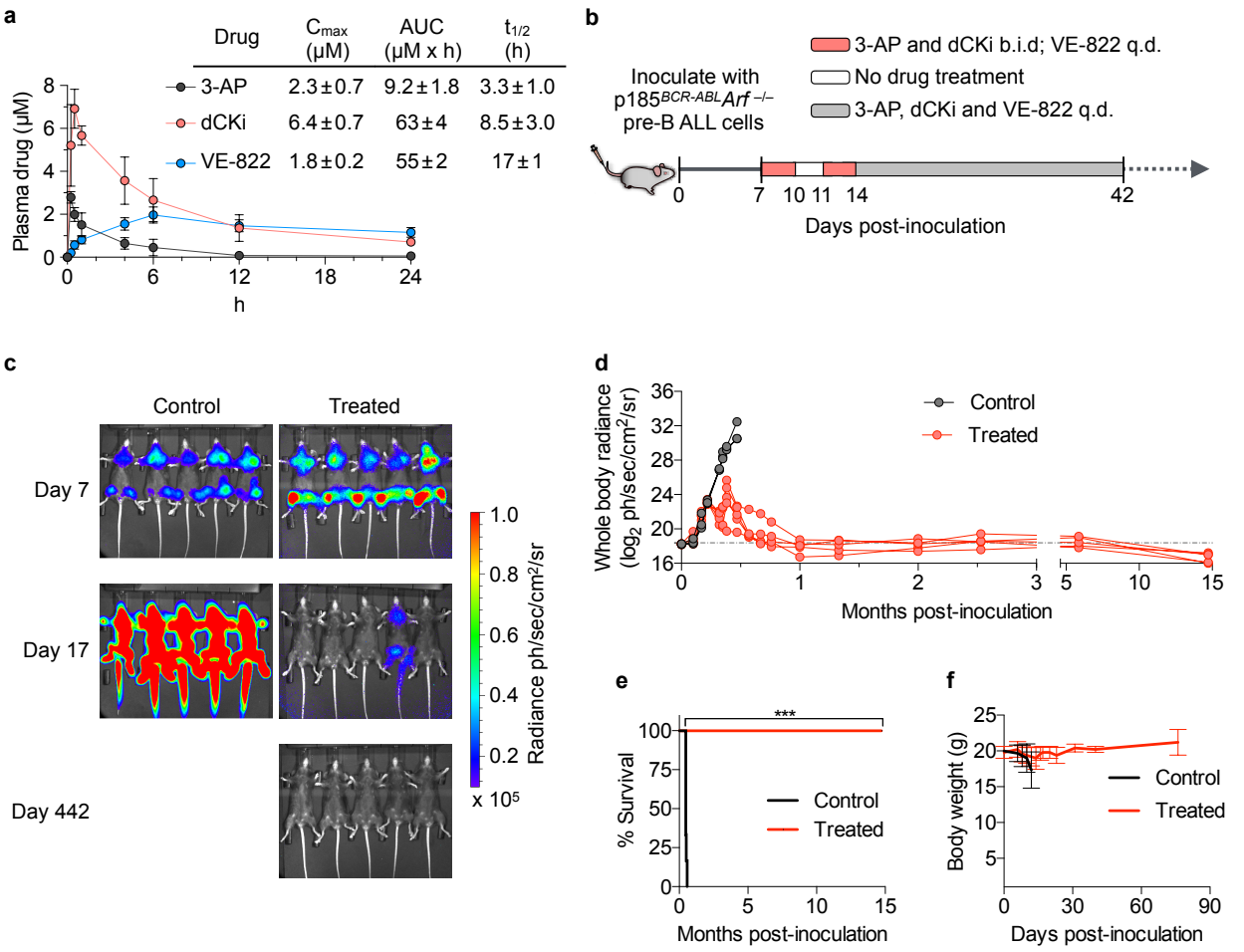

Fig. 1.6. The triple combination therapy is effective and well-tolerated in a systemic primary B-ALL model. (a) Plasma pharmacokinetic parameters for 3-AP (15 mg/kg), VE-822 (40 mg/kg) and dCKi (50 mg/kg) in C57BL/6 mice (n ≥ 3) after single dose oral co-administration (mean ± s.d., n ≥ 3). **(b)** Doses and schedules for the triple combination therapy of leukemia bearing mice. **(c and d)** Bioluminescence images **(c)** and quantification of whole body radiance **(d)** of leukemia bearing mice treated with the combination therapy (treated, n = 5) or vehicle (control, n = 5) at indicated days after tumor inoculation. See also Supplementary Fig. 11–13. **(e and f)** Kaplan-Meier survival analysis **(e)** and body weight measurements **(f)** of leukemia bearing mice treated with the combination therapy (treated, n = 5) or vehicle (control, n = 5). Median survival for the control group was 14 days after treatment initiation, whereas median

survival for the treated group remains undefined (Mantel-Cox test).* $P < 0.05$; ** $P < 0.01$; *** $P < 0.001$; **** $P < 0.0001$. **q.d.** once/day; **b.i.d.** twice/day.

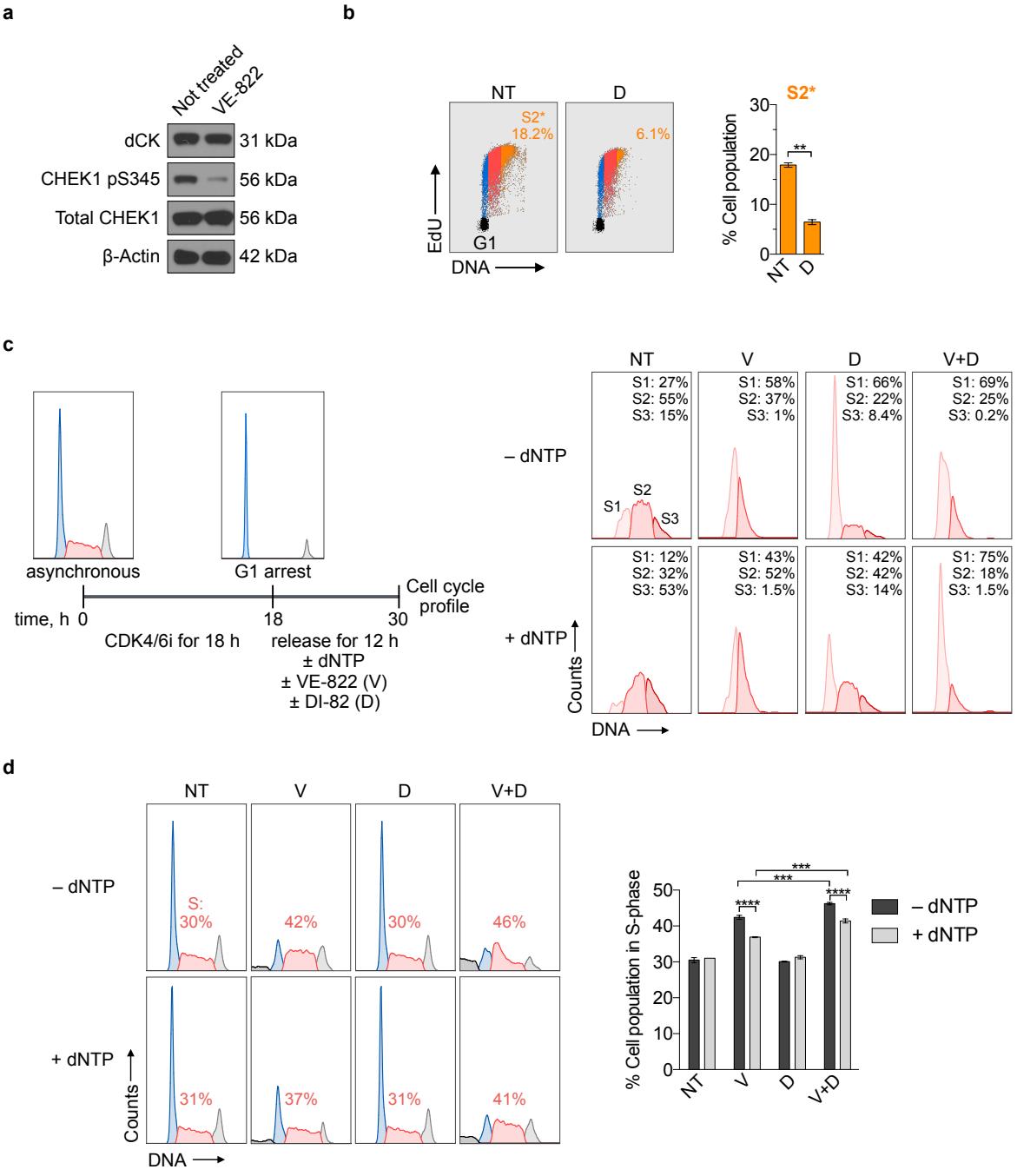

Fig. S1.1. Constitutive ATR activation in CEM T-ALL cells and its role in cell cycle progression. (a) Representative pS345 CHEK1 immunoblots of CEM cells ± VE-822 (1 μM) for 24 h. **(b)** Flow cytometry analysis of EdU incorporation in CEM T-ALL cells treated with VE-822 (1 μM) and/or dCKi (DI-82,1 μM) for 12 h following release from G1 arrest. Bar graphs

summarize the percentage of cell populations in S3 (late S-phase) 12 h (mean ± s.d., n = 2, one-way ANOVA, Bonferroni corrected). Plots are representative of two independent experiments. **(c)** Cell cycle analyses of synchronous CEM T-ALL cells treated with VE-822 (1 μM) and/or dCKi (DI-82,1 μM) in the presence or absence of 10 μM dNTPs for 12 h following release from G1 arrest. **(d)** Cell cycle analyses of asynchronous CEM T-ALL cells treated with VE-822 (1 μM) and/or dCKi (DI-82,1 μM) in the presence or absence of 10 μM dNTPs for 12 h. Bar graph summarize the percentage of cell populations in S-phase at 12 h (mean ± s.d., n = 2, one-way ANOVA, Bonferroni corrected).

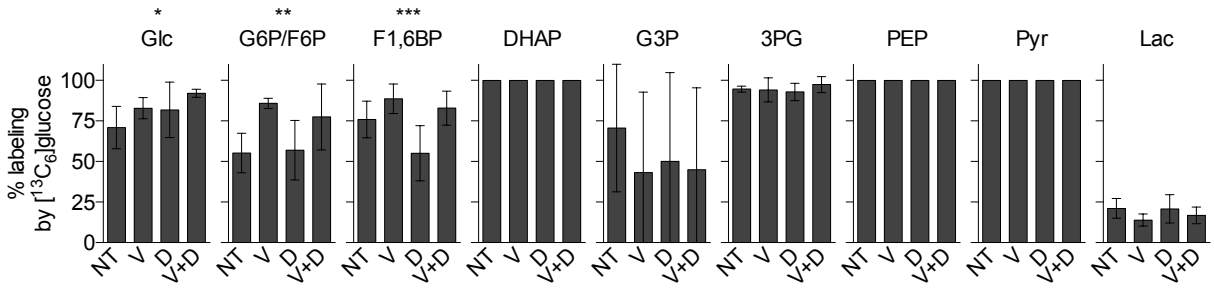

Fig. S1.2. ATR inhibition minimally impacts glucose labeling in the glycolysis of CEM T-ALL cells. Percent glucose labeling of glycolytic metabolites (mean ± s.d., n = 6, one-way ANOVA).

Glc glucose; **G6P/F6P** glucose 6-phosphate/fructose 6-phosphate; **F1,6BP** fructose 1,6-bisphosphate; **DHAP** dihydroacetone phosphate; **G3P** glyceraldehyde 3-phosphate; **3PG** 3-phosphoglycerate; **PEP** phosphoenolpyruvate; **Pyr** pyruvate; **Lac** lactate.

* $P < 0.05$; ** $P < 0.01$; *** $P < 0.001$.

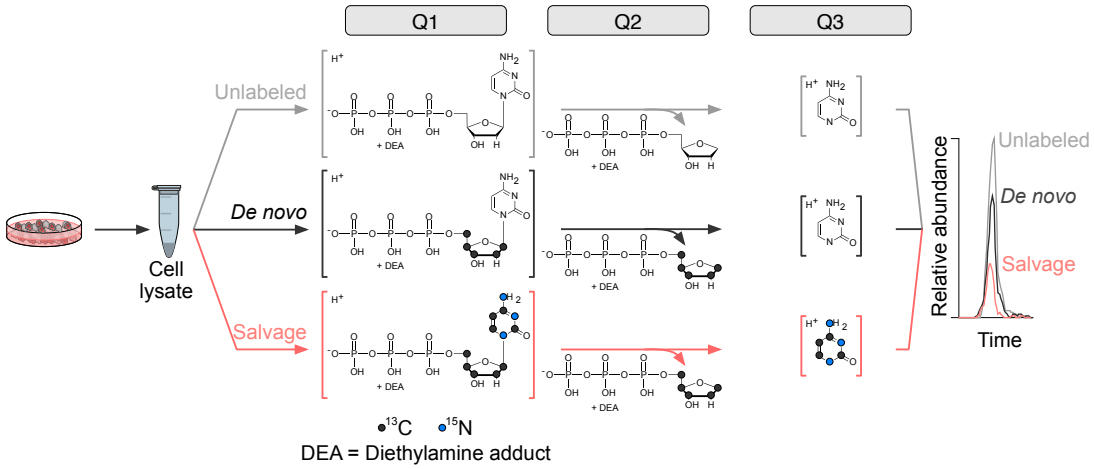

Fig. S1.3. Workflow for the targeted mass spectrometric analysis used in Fig. 2 to measure dCTP pools. Optimally, nucleotides should be monitored in the positive mode to precisely measure the labeled atoms on the nucleobase and sugar moieties. To enable such measurements, we expanded on the work by Cohen and colleagues[1] who reported the use of ion pairing reagents. With the addition of diethylamine (DEA) in the mobile phase, nucleotides have their negative charge phosphate group masked by DEA and their nucleobase becomes protonated. Under these conditions, nucleotides with the DEA adduct were monitored in the positive mode as $[NTP{-}DEA{-}H]^+$ and the fragmentation of the adduct nucleotide ions resulted in protonated nucleobases.

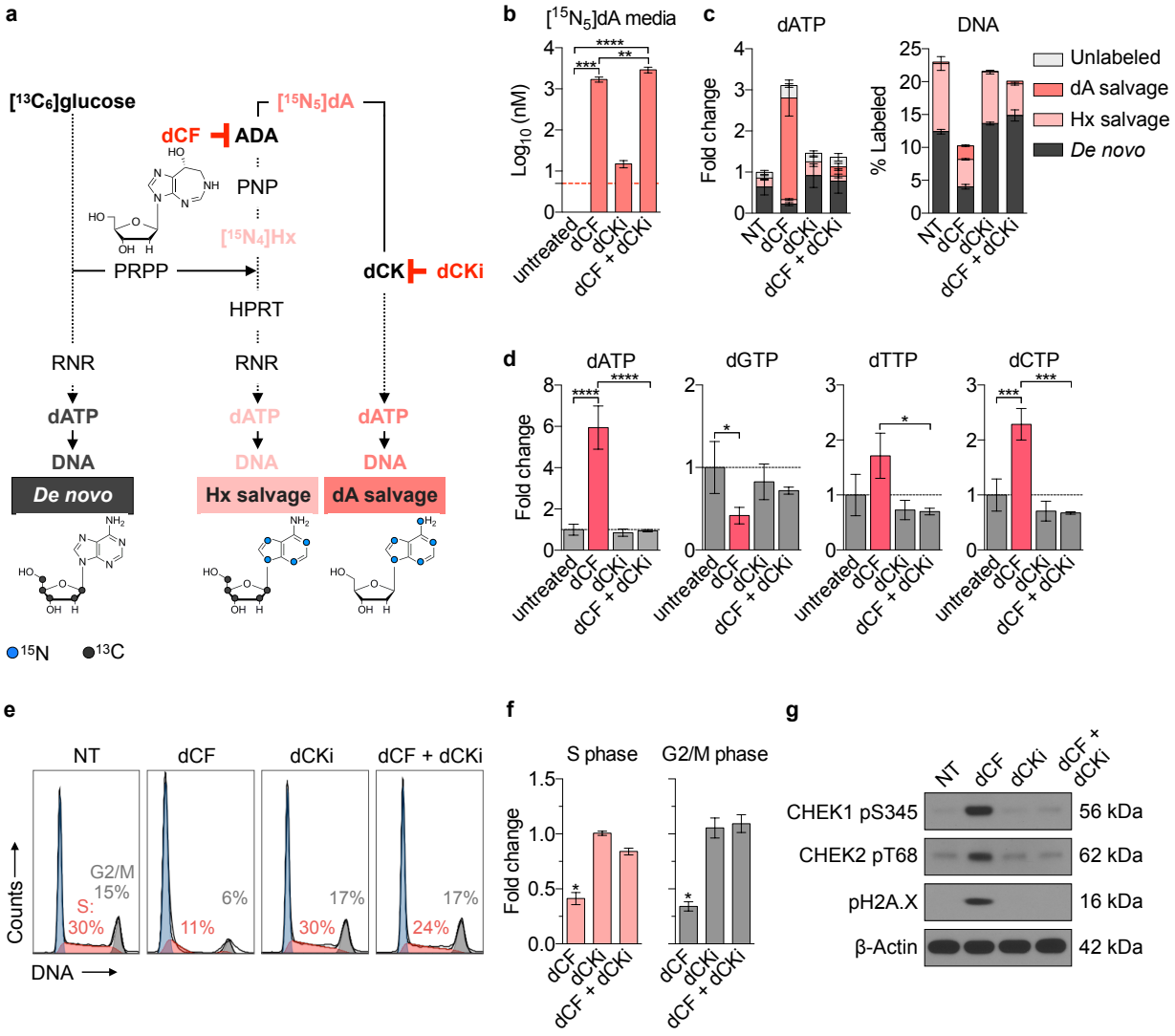

Fig. S1.4. dCK-dependent dATP production from dA requires ADA inhibition (companion for Fig. 1). (a) Schematic representation and the ^{13}C and ^{15}N labeling pattern of the *de novo* and salvage dATP biosynthetic pathways. dA can be salvaged as a nucleobase through the actions of ADA, PNP, and HPRT or as an intact deoxyribonucleoside via dCK. The former salvage pathway is blocked by Pentostatin (dCF), a specific adenosine deaminase (ADA) inhibitor; the latter salvage pathway is blocked by DI-82, a dCK inhibitor (dCKi). **(b–d)** Jurkat cells were treated with dCF (10 μM) ± dCKi (1 μM) in culture media containing 11 mM [$^{13}C_6$]glucose and 5 μM [$^{15}N_5$]dA for 18 h. **(b)** [$^{15}N_5$]dA levels in the cell culture media 18 h after

treatment initiation (mean ± s.d., n = 3, one-way ANOVA, Bonferroni corrected). **(c)** Biosynthetic routes to produce free dATP and dATP incorporated into newly replicated DNA 18 h after treatment initiation: *de novo* from [$^{13}C_6$]glucose via RNR, [$^{15}N_5$]dA salvage via dCK catalyzed phosphorylation, and HPRT mediated salvage of [$^{15}N_5$]hypoxanthine (Hx) produced from [$^{15}N_5$]dA following deamination, and glycosidic bond cleavage catalyzed by ADA and PNP, respectively (mean ± s.d., n = 3). **(d)** Fold changes in total dNTP levels 18 h after treatment initiation (mean ± s.d., n = 3, one-way ANOVA, Bonferroni corrected). **(e)** Cell cycle analyses of Jurkat cells treated as indicated for 24 h. **(f)** Quantification of cells in S (left panel) and G2/M (right panel) after the indicated treatments for 24 h (mean ± s.d., n = 2). **(g)** Representative immunoblots of CHEK1, CHEK2 and H2A.X phosphorylation; cells were treated as indicated for 24 h.

* $P < 0.05$; ** $P < 0.01$; *** $P < 0.001$; **** $P < 0.0001$.

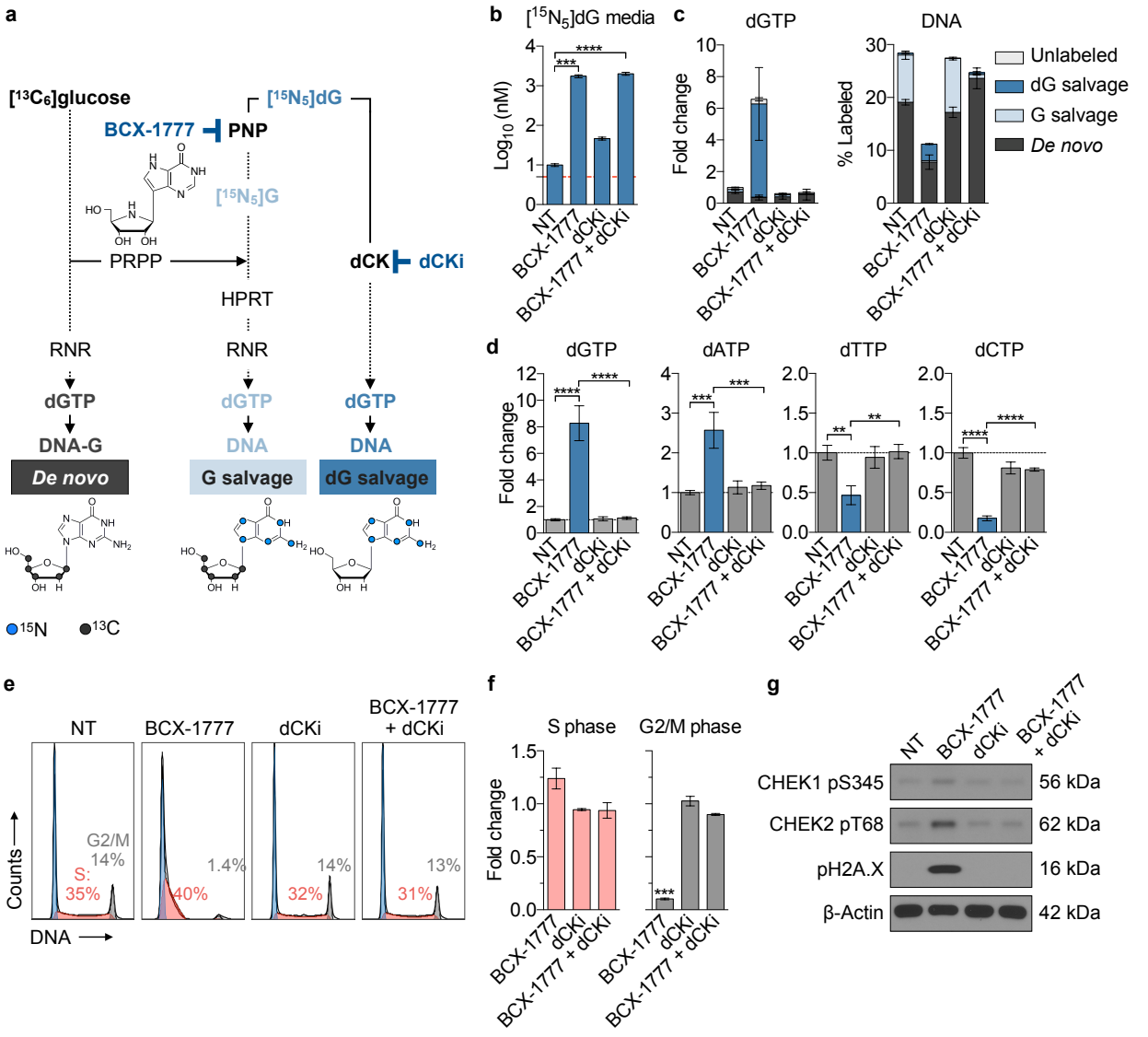

Fig. S1.5. dCK-dependent production from dG requires PNP inhibition (companion for Fig. 1). (a) Schematic representation and the ^{13}C and ^{15}N labeling pattern of the *de novo* and salvage dGTP biosynthetic pathways. dG can be salvaged as a nucleobase through the actions of PNP and HPRT or as an intact deoxyribonucleoside via dCK. The former salvage pathway is blocked by BCX-1777, a specific inhibitor of PNP; the latter salvage pathway is blocked by DI-82, a dCK inhibitor (dCKi). **(b–d)** Jurkat cells were treated with BCX-1777 (100 nM) ± dCKi (1 μM) in culture media containing 11 mM [$^{13}C_6$]glucose and 5 μM [$^{15}N_5$]dA for 18 h. **(b)** [$^{15}N_5$]dG concentration in the cell culture media 18 h after treatment initiation (mean ± SD, n = 3, one-way ANOVA, Bonferroni corrected). **(c)** Biosynthetic routes to produce free dGTP and dGTP incorporated into newly replicated DNA 18 h after treatment initiation: *de novo* from

[$^{13}C_6$]glucose via RNR, [$^{15}N_5$]dG salvage via dCK catalyzed phosphorylation, and HPRT mediated salvage of [$^{15}N_5$]G produced from [$^{15}N_5$]dG following glycosidic bond cleavage catalyzed by PNP (mean ± SD, n = 3). (**d**) Fold changes in total dNTP levels 18 h after treatment initiation (mean ± SD, n = 3, one-way ANOVA, Bonferroni corrected). (**e**) Cell cycle analyses of Jurkat cells treated as indicated for 24 h. **(f)** Quantification of cells in the S (left panel) and G2/M (right panel) after the indicated treatments for 24 h (mean ± SD, n = 2, one-way ANOVA, Bonferroni corrected). (**g**) Representative immunoblots of CHEK1, CHEK2 and H2A.X phosphorylation; cells were treated as indicated for 24 h

* $P < 0.05$; ** $P < 0.01$; *** $P < 0.001$; **** $P < 0.0001$.

PNP purine phosphorylase; **Hx** hypoxanthine; **HPRT** hypoxanthine phosphoribosyltransferase.

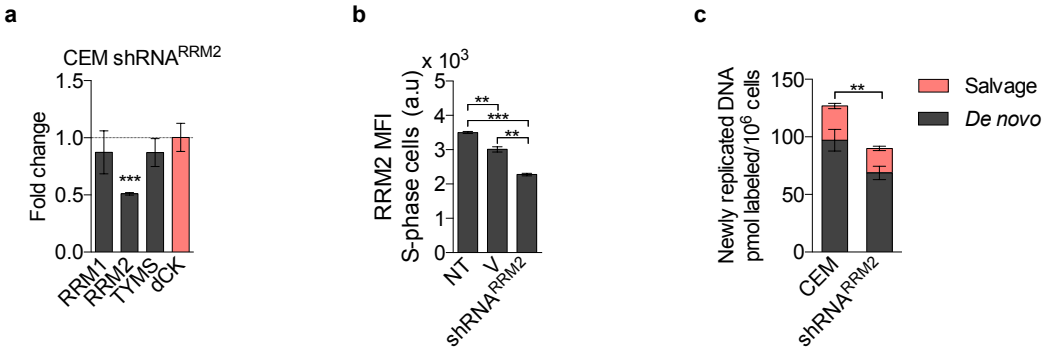

Fig. S1.6. Effects of knocking down RRM2 using shRNA on RRM2 protein levels and RNR-produced dCTP incorporated into newly replicated DNA of CEM T-ALL cells. (a) Protein levels in CEM shRNA^{RRM2} cells as determined by nLC-MS/MS (mean ± SD, n = 3, one sample t-test to assess if the mean of the protein level normalized to parental CEM is equal to one). **(b)** Mean fluorescence intensity (MFI) of RRM2 levels in S-phase parental CEM cells treated with 1 μM VE-822 for 12 h (V) and CEM shRNA^{RRM2} cells (mean ± SD, n = 2, one-way ANOVA, Bonferroni corrected). **(c)** Contributions of the *de novo* and salvage pathways to dCTP incorporated into newly replicated DNA in parental CEM and CEM shRNA^{RRM2} cells (mean ± SD, n = 3, two-way ANOVA, Bonferroni corrected, comparing *de novo* contribution between parental CEM and CEM shRNA^{RRM2}).

* $P < 0.05$; ** $P < 0.01$; *** $P < 0.001$; **** $P < 0.0001$.

RRM1 ribonucleotide reductase subunit 1; **RRM2** ribonucleotide reductase subunit 2; **TYMS** thymidylate synthase; **dCK** deoxycytidine kinase.

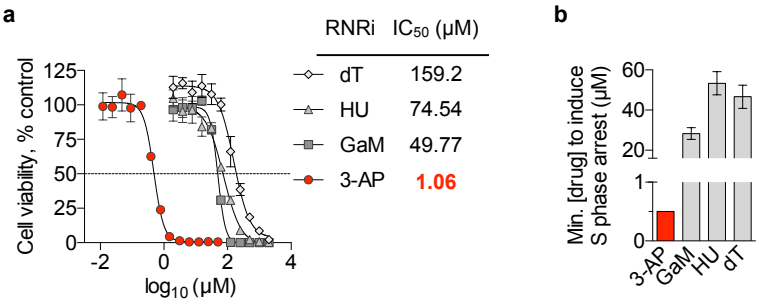

Fig. S1.7. IC_{50} values and minimal concentrations of RNR inhibitors required to cause S-phase arrest (see in Fig. 3b and main text for details). (a) IC_{50} values of dT, HU, GaM, and 3-AP in CEM cells (CellTiter-Glo assay at 72 h, mean ± SD, n = 3). **(b)** Minimal concentrations of the four RNR inhibitors required for the induction of S-phase arrest observed in Fig. 3b (see main text for details, mean ± SD, n = 2, one-way ANOVA, $P < 0.0001$).
dT thymidine; **HU** hydroxyurea; **GaM** gallium maltolate.

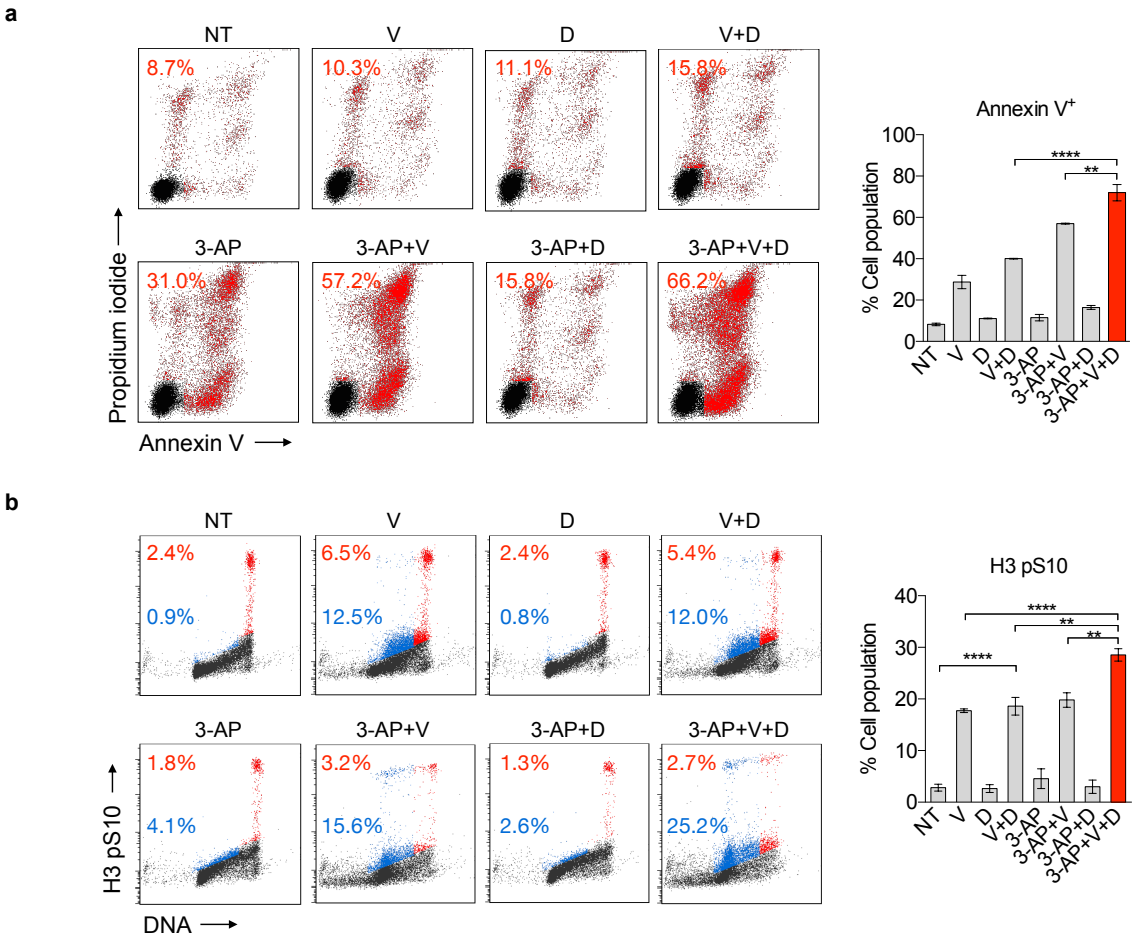

Fig. S1.8. Analyses of apoptosis induction and premature mitotic entry in CEM cells treated with ATR, dCK and RNR inhibitors as indicated in Fig. 4. (a) Apoptosis induction in CEM cells treated as indicated (500 nM 3-AP, 1 μM VE-822, and 1 μM dCKi) for 24 h using flow cytometry for Annexin V and PI staining (mean ± SD, n = 2, one-way ANOVA, Bonferroni corrected). **(b)** Phosphorylated H3 on serine 10 (pS10 H3) levels in CEM cells treated as indicated (500 nM 3-AP, 1 μM VE-822, and 1 μM dCKi) for 24 h using flow cytometry (mean ± SD, n = 2, one-way ANOVA, Bonferroni corrected).

NT: not treated control, V: VE-822, D: dCKi.

* $P < 0.05$; ** $P < 0.01$; *** $P < 0.001$; **** $P < 0.0001$.

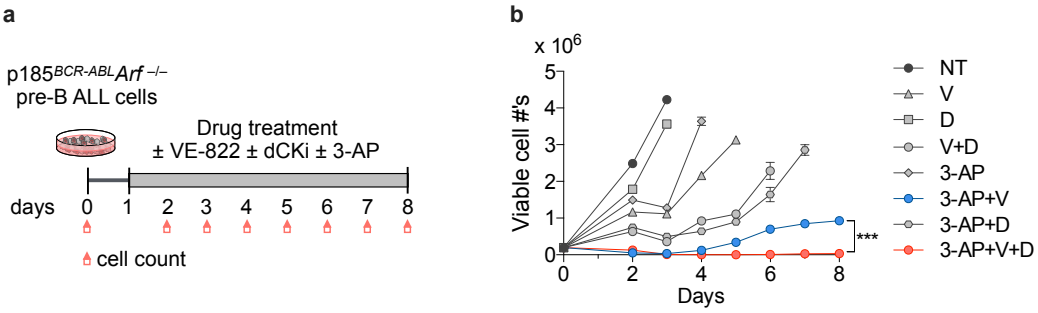

Fig. S1.9. Optimal therapeutic efficacy against p185$^{BCR\text{-}ABL}$*Arf* $^{-/-}$ pre-B-ALL cells in culture requires combined inhibition of ATR, RNR and dCK (companion for Fig. 5). (a and b)

Treatment scheme **(a)** and growth curves **(b)** of p185$^{BCR\text{-}ABL}$*Arf*$^{-/-}$ pre-B-ALL treated as indicated (mean ± SD, n = 2, unpaired two-tailed Student's t-test comparing 3-AP+V and 3-AP+V+D at day 8).

NT: not treated control, V: VE-822, D: dCKi.

*** $P < 0.001$.

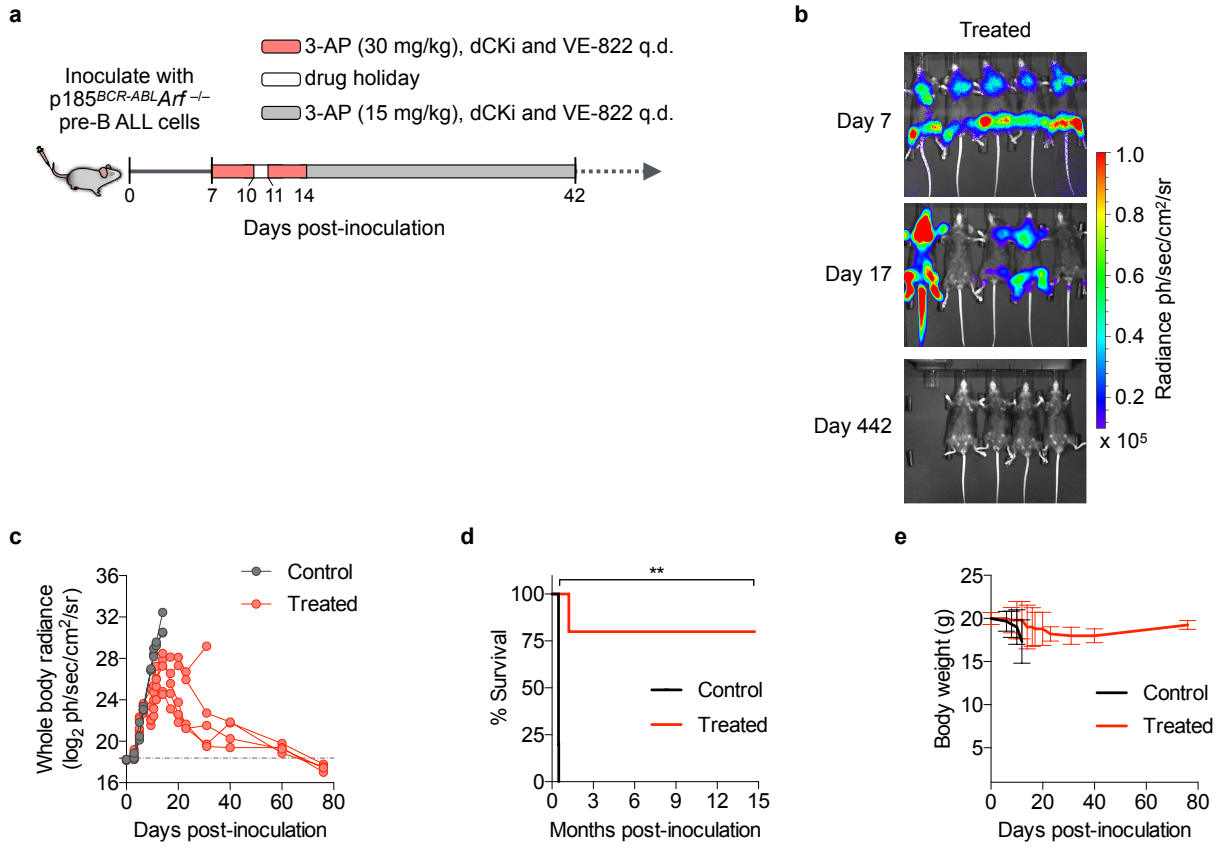

Fig. S1.10. Co-targeting ATR, dCK and RNR is effective and well-tolerated in a systemic primary B-ALL model (companion for Fig. 6). (a, b, c) Schematic representation of the therapeutic regimen **(a)**, bioluminescence images **(b)**, and quantification of whole-body radiance **(c)** of leukemia bearing mice treated with a slight modification of the therapeutic regime shown in **Fig. 6b** (3-AP, 30 mg/kg q.d., treated, n = 5). **(d and e)** Kaplan-Meier survival analysis **(d)** and body weight measurements **(e)** of leukemia bearing mice treated with the combination therapy (treated, n = 5) or vehicle (control from **Fig. 6c**, n = 5). Median survival for the control group is 14 days after treatment initiation, whereas median survival for the treated group remains undefined (Mantel-Cox test).

** $P < 0.01$.

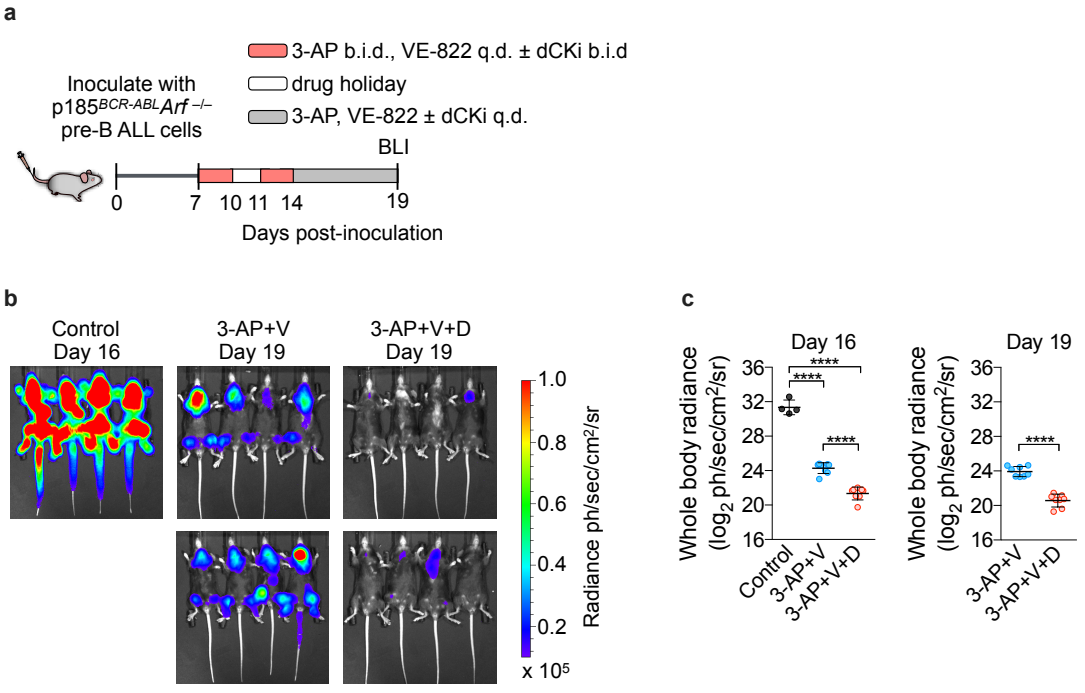

Fig. S1.11. Optimal therapeutic efficacy against p185$^{BCR\text{-}ABL}$*Arf* $^{-/-}$ pre-B-ALL cells *in vivo* requires combined inhibition of ATR, RNR and dCK (companion for Fig. 6). (a) Schematic representation of the therapeutic regimen; **(b)** bioluminescence images **(c)**, and quantification of whole-body radiance of leukemia bearing mice treated with 15 mg/kg 3-AP + 40 mg/kg VE-822 (3-AP+V, n = 8), 15 mg/kg 3-AP + 40 mg/kg VE-822 + 50 mg/kg dCKi (3-AP+V+D, n = 8), and vehicle (control, n = 4). Drugs were formulated in PEG-200, Transcutol, Labrasol, and Tween-80 blended in a ratio of 5:3:1:1 and were administered orally. One-way ANOVA, Bonferroni corrected for the BLI comparisons among three groups at day 16 and unpaired two-tailed Student's t-test for the BLI comparison of 3-AP+V and 3-AP+V+D at day 19. Mice from control group were sacrificed before day 19 due to high leukemic burden.
* $P < 0.05$; ** $P < 0.01$; *** $P < 0.001$; **** $P < 0.0001$.

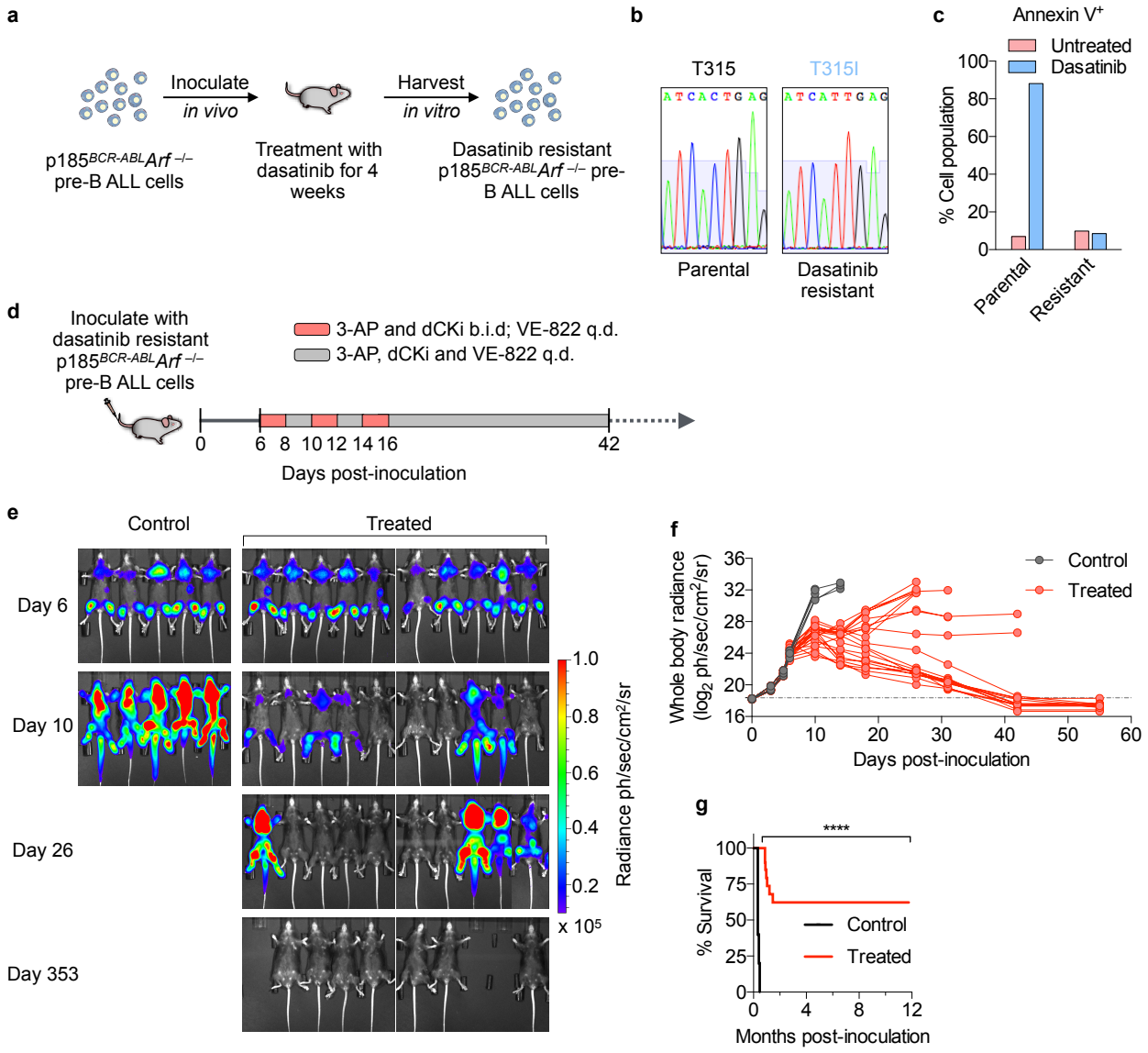

Fig. S1.12. The combination therapy is efficacious against a dasatinib-resistant pre-B-ALL mouse model. (a) Generation of dasatinib-resistant p185$^{BCR\text{-}ABL}$*Arf*$^{-/-}$ pre-B-ALL cells. Leukemia bearing C57BL/6 mice, were treated with 10 mg/kg dasatinib q.d. (once/day) for 20 days. Upon presentation of resistance, leukemia cells were harvested from the bone marrow. **(b)** Sequencing of ABL kinase domain of dasatinib-resistant p185$^{BCR\text{-}ABL}$*Arf*$^{-/-}$ pre-B-ALL cells showed the T315I gate-keeper mutation. **(c)** Apoptosis induction in p185$^{BCR\text{-}ABL}$*Arf*$^{-/-}$ pre-B-ALL parental and resistant cells treated as indicated (dasatinib, 1 nM) for 24 h using flow cytometry for Annexin V and PI staining. **(d)** Doses and schedule of the combination treatment (3-AP, dCKi and VE-822) against dasatinib-resistant leukemia bearing mice. **(e and f)** Bioluminescence

images **(e)** and quantification of whole body radiance **(f)** of dasatinib-resistant leukemia bearing mice treated with the combination therapy (treated, n = 20) or vehicle (control, n = 5) at indicated days after tumor inoculation. 10 representative mice are shown for the treated group. **(g)** Kaplan-Meier survival analysis of dasatinib-resistant leukemia bearing mice treated with the combination therapy (treated, n = 20) or vehicle (control, n = 5). Median survival for the control group is 14 days after treatment initiation, whereas median survival for the treated group remains undefined (Mantel-Cox test).

**** $P < 0.0001$.

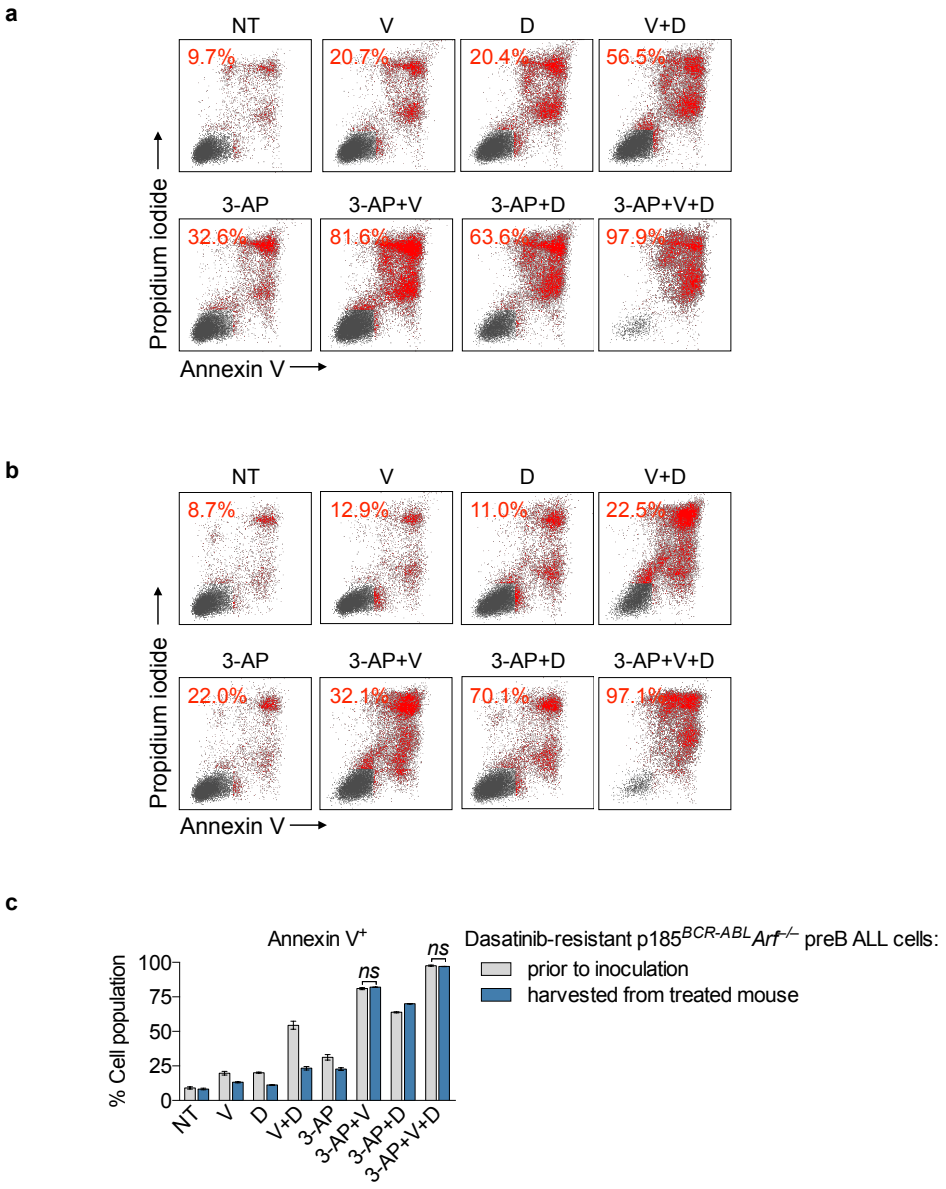

Fig. S1.13. Dasatinib resistant pre-B-ALL cells recovered from a leukemic mouse which was treated with the triple combination therapy and eventually succumbed to disease retain sensitivity to the triple combination therapy. (a) Apoptosis induction of dasatinib-resistant p185$^{BCR\text{-}ABL}$*Arf*$^{-/-}$ pre-B-ALL cells, prior to inoculation in mice, treated as indicated (350 nM 3-AP, 100 nM VE-822, and 1 μM dCKi) for 72 h using flow cytometry for Annexin V and PI staining. **(b)** Apoptosis induction of dasatinib-resistant p185$^{BCR\text{-}ABL}$*Arf*$^{-/-}$ pre-B-ALL cells, harvested from bone marrow of a leukemic mouse treated with the triple combination therapy and eventually succumbed to disease from Supplementary Fig. 13, treated as indicated (350 nM 3-AP, 100 nM VE-822, and 1 μM dCKi) for 72 h using flow cytometry for Annexin V and PI

staining. **(c)** Bar graph summarizes the percentage of Annexin V^+ cell population from **(a)** and **(b)** (mean ± SD, n = 2, one-way ANOVA, Bonferroni corrected).
ns not significant.

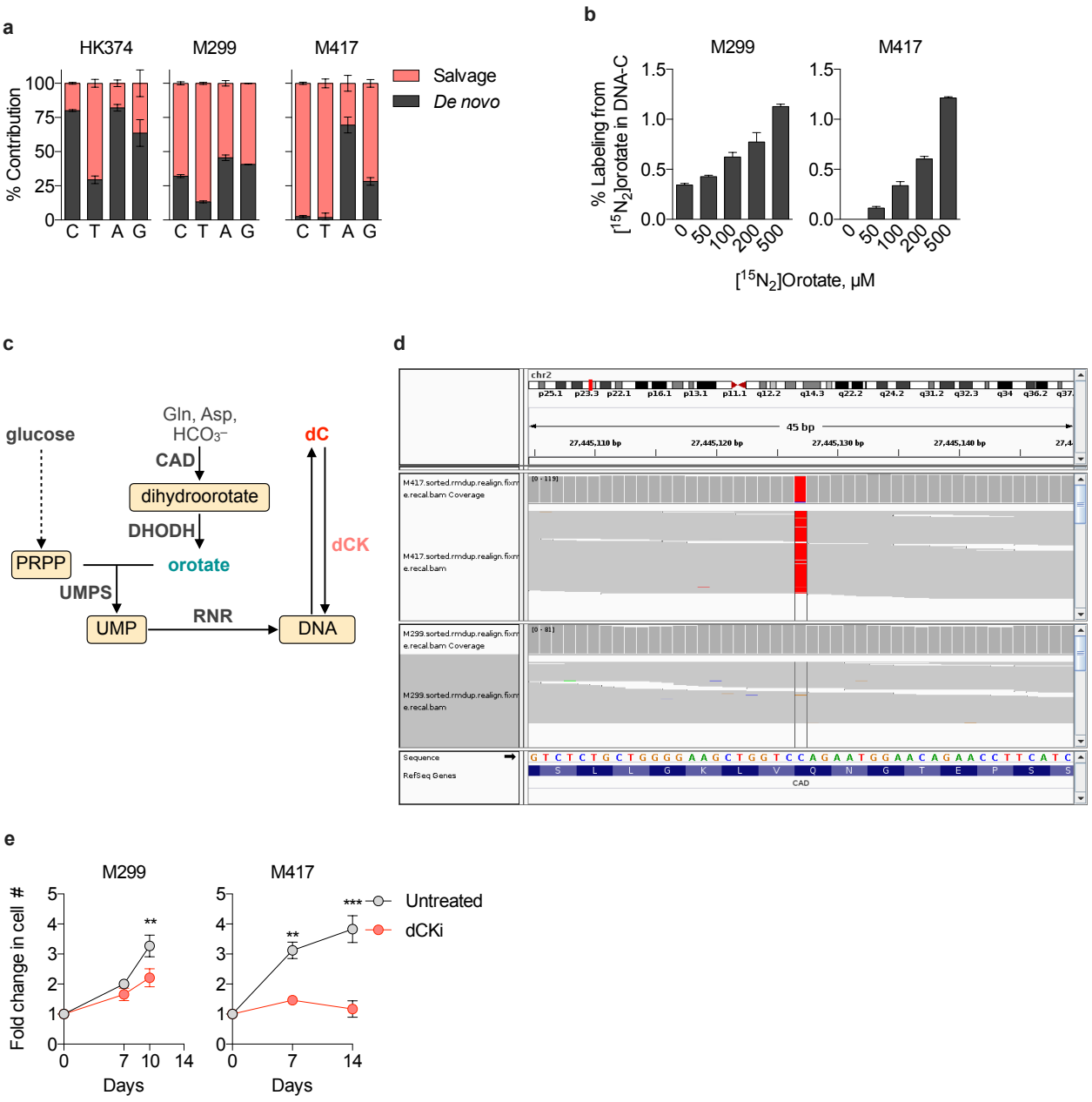

Fig. S1.14. Nucleotide biosynthetic diversity in patient-derived samples. (a) Profiling the differential contributions of the *de novo* and salvage pathways to newly replicated DNA in patient-derived primary glioblastoma (HK374) and melanoma (M299 and M417) cells (mean ± SD, n = 3). Cells were incubated in culture media containing 11 mM [$^{13}C_6$]glucose and 5 μM each of the following labeled nucleosides: [$^{13}C_9$,$^{15}N_3$]dC, [$^{13}C_{10}$,$^{15}N_2$]dT, [$^{13}C_{10}$,$^{15}N_5$]dA, [$^{15}N_5$]dG. **(b)** [$^{15}N_2$]orotate enrichment in dCTP incorporated into newly replicated DNA in M299 and M417 cells at 18 h (mean ± SD, n = 3). Cells were incubated in culture media containing 11 mM [$^{13}C_6$]glucose with indicated varying concentration of [$^{15}N_2$]orotate. **(c)** Schematic representation

of the *de novo* and salvage nucleotide pathway involving CAD, DHODH, and UMPS to newly replicated DNA. **(d)** IGV plot from exome sequencing of M417 showing homozygous CAD mutation (Q140*), present in 104 out of 108 reads. Results for M299 shown as negative reference. **(e)** Growth curves for M299 and M417 treated with vehicle or 1 μM dCKi (mean ± SD, n = 2).

* $P < 0.05$; ** $P < 0.01$; *** $P < 0.001$; **** $P < 0.0001$.

CAD carbamoyl-phosphate synthetase 2, aspartate transcarbamylase, and dihydroorotase; **DHODH** dihydroorotate dehydrogenase; **UMPS** uridine monophosphate synthase; **PRPP** 5'-phosphoribosyl pyrophosphate; **UMP** uridine monophosphate.

REFERENCES

1. Kumar, D., Viberg, J., Nilsson, A. K. & Chabes, A. Highly mutagenic and severely imbalanced dNTP pools can escape detection by the S-phase checkpoint. *Nucleic Acids Res* **38**, 3975-3983 (2010).

2. Reichard, P. Interactions between deoxyribonucleotide and DNA synthesis. *Annu Rev Biochem* **57**, 349-374 (1988).

3. Nordlund, P. & Reichard, P. Ribonucleotide reductases. *Annu. Rev. Biochem.* **75**, 681-706 (2006).

4. Aye, Y., Li, M., Long, M. J. & Weiss, R. S. Ribonucleotide reductase and cancer: biological mechanisms and targeted therapies. *Oncogene* **34**, 2011-2021 (2015).

5. Sabini, E., Hazra, S., Ort, S., Konrad, M. & Lavie, A. Structural basis for substrate promiscuity of dCK. *J Mol Biol* **378**, 607-621 (2008).

6. Tennant, D. A., Durán, R. V. & Gottlieb, E. Targeting metabolic transformation for cancer therapy. *Nat Rev Cancer* **10**, 267-277 (2010).

7. Barretina, J. et al. The Cancer Cell Line Encyclopedia enables predictive modelling of anticancer drug sensitivity. *Nature* **483**, 603-607 (2012).

8. Fernandez-Banet, J. et al. OASIS: web-based platform for exploring cancer multi-omics data. *Nat Methods* **13**, 9-10 (2016).

9. Cerami, E. et al. The cBio cancer genomics portal: an open platform for exploring multidimensional cancer genomics data. *Cancer Discov* **2**, 401-404 (2012).

10. Gao, J. et al. Integrative analysis of complex cancer genomics and clinical profiles using the cBioPortal. *Sci Signal* **6**, pl1 (2013).

11. Boroughs, L. K. & DeBerardinis, R. J. Metabolic pathways promoting cancer cell survival and growth. *Nat Cell Biol* **17**, 351-359 (2015).

12. Nathanson, D. A. et al. Co-targeting of convergent nucleotide biosynthetic pathways for leukemia eradication. *J Exp Med* **211**, 473-486 (2014).

13. Luo, J., Solimini, N. L. & Elledge, S. J. Principles of cancer therapy: oncogene and non-oncogene addiction. *Cell* **136**, 823-837 (2009).

14. Austin, W. R. et al. Nucleoside salvage pathway kinases regulate hematopoiesis by linking nucleotide metabolism with replication stress. *J Exp Med* **209**, 2215-2228 (2012).

15. Toy, G. et al. Requirement for deoxycytidine kinase in T and B lymphocyte development. *Proc Natl Acad Sci U S A* **107**, 5551-5556 (2010).

16. Ben-Sahra, I., Howell, J. J., Asara, J. M. & Manning, B. D. Stimulation of de novo pyrimidine synthesis by growth signaling through mTOR and S6K1. *Science* **339**, 1323-1328 (2013).

17. Robitaille, A. M. et al. Quantitative phosphoproteomics reveal mTORC1 activates de novo pyrimidine synthesis. *Science* **339**, 1320-1323 (2013).

18. Saha, A. et al. Akt phosphorylation and regulation of transketolase is a nodal point for amino acid control of purine synthesis. *Mol Cell* **55**, 264-276 (2014).

19. Cunningham, J. T., Moreno, M. V., Lodi, A., Ronen, S. M. & Ruggero, D. Protein and nucleotide biosynthesis are coupled by a single rate-limiting enzyme, PRPS2, to drive cancer. *Cell* **157**, 1088-1103 (2014).

20. Liu, Y. C. et al. Global regulation of nucleotide biosynthetic genes by c-Myc. *PLoS One* **3**, e2722 (2008).

21. Aird, K. M. et al. Suppression of nucleotide metabolism underlies the establishment and maintenance of oncogene-induced senescence. *Cell reports* **3**, 1252-1265 (2013).

22. Dobbelstein, M. & Sørensen, C. S. Exploiting replicative stress to treat cancer. *Nat Rev Drug Discov* **14**, 405-423 (2015).

23. Weber, A. M. & Ryan, A. J. ATM and ATR as therapeutic targets in cancer. *Pharmacol Ther* **149**, 124-138 (2015).

24. Branzei, D. & Foiani, M. Maintaining genome stability at the replication fork. *Nat Rev Mol Cell Biol* **11**, 208-219 (2010).

25. Pfister, S. X. et al. Inhibiting WEE1 Selectively Kills Histone H3K36me3-Deficient Cancers by dNTP Starvation. *Cancer Cell* (2015).

26. Buisson, R., Boisvert, J. L., Benes, C. H. & Zou, L. Distinct but Concerted Roles of ATR, DNA-PK, and Chk1 in Countering Replication Stress during S Phase. *Mol Cell* **59**, 1011-1024 (2015).

27. Bester, A. C. et al. Nucleotide deficiency promotes genomic instability in early stages of cancer development. *Cell* **145**, 435-446 (2011).

28. Beyaert, M., Starczewska, E., Van Den Neste, E. & Bontemps, F. A crucial role for ATR in the regulation of deoxycytidine kinase activity. *Biochem Pharmacol* **100**, 40-50 (2016).

29. Hazra, S., Szewczak, A., Ort, S., Konrad, M. & Lavie, A. Post-translational phosphorylation of serine 74 of human deoxycytidine kinase favors the enzyme adopting the open conformation making it competent for nucleoside binding and release. *Biochemistry* **50**, 2870-2880 (2011).

30. Smal, C. et al. Identification of in vivo phosphorylation sites on human deoxycytidine kinase. Role of Ser-74 in the control of enzyme activity. *J Biol Chem* **281**, 4887-4893 (2006).

31. Boulos, N. et al. Chemotherapeutic agents circumvent emergence of dasatinib-resistant BCR-ABL kinase mutations in a precise mouse model of Philadelphia chromosome-positive acute lymphoblastic leukemia. *Blood* **117**, 3585-3595 (2011).

32. Hughes, T. P. et al. BCR-ABL1 mutation development during first-line treatment with dasatinib or imatinib for chronic myeloid leukemia in chronic phase. *Leukemia* **29**, 1832-1838 (2015).

33. Williams, R. T., Roussel, M. F. & Sherr, C. J. Arf gene loss enhances oncogenicity and limits imatinib response in mouse models of Bcr-Abl-induced acute lymphoblastic leukemia. *Proc Natl Acad Sci U S A* **103**, 6688-6693 (2006).

34. Dai, Y. & Grant, S. New insights into checkpoint kinase 1 in the DNA damage response signaling network. *Clin Cancer Res* **16**, 376-383 (2010).

35. Fokas, E. et al. Targeting ATR in vivo using the novel inhibitor VE-822 results in selective sensitization of pancreatic tumors to radiation. *Cell Death Dis* **3**, e441 (2012).

36. Fry, D. W. et al. Specific inhibition of cyclin-dependent kinase 4/6 by PD 0332991 and associated antitumor activity in human tumor xenografts. *Mol Cancer Ther* **3**, 1427-1438 (2004).

37. Toogood, P. L. et al. Discovery of a potent and selective inhibitor of cyclin-dependent kinase 4/6. *J Med Chem* **48**, 2388-2406 (2005).

38. Nomme, J. et al. Structure-guided development of deoxycytidine kinase inhibitors with nanomolar affinity and improved metabolic stability. *J Med Chem* **57**, 9480-9494 (2014).

39. Giblett, E. R. ADA and PNP deficiencies: how it all began. *Ann N Y Acad Sci* **451**, 1-8 (1985).

40. Eykelenboom, J. K. et al. ATR activates the S-M checkpoint during unperturbed growth to ensure sufficient replication prior to mitotic onset. *Cell Rep* **5**, 1095-1107 (2013).

41. Koundrioukoff, S. et al. Stepwise activation of the ATR signaling pathway upon increasing replication stress impacts fragile site integrity. *PLoS Genet* **9**, e1003643 (2013).

42. Marheineke, K. & Hyrien, O. Control of replication origin density and firing time in Xenopus egg extracts: role of a caffeine-sensitive, ATR-dependent checkpoint. *J Biol Chem* **279**, 28071-28081 (2004).

43. Shechter, D., Costanzo, V. & Gautier, J. ATR and ATM regulate the timing of DNA replication origin firing. *Nat Cell Biol* **6**, 648-655 (2004).

44. D'Angiolella, V. et al. Cyclin F-mediated degradation of ribonucleotide reductase M2 controls genome integrity and DNA repair. *Cell* **149**, 1023-1034 (2012).

45. Zhang, Y. W., Jones, T. L., Martin, S. E., Caplen, N. J. & Pommier, Y. Implication of checkpoint kinase-dependent up-regulation of ribonucleotide reductase R2 in DNA damage response. *J Biol Chem* **284**, 18085-18095 (2009).

46. Cory, J. G. et al. Inhibitors of ribonucleotide reductase. Comparative effects of amino- and hydroxy-substituted pyridine-2-carboxaldehyde thiosemicarbazones. *Biochem Pharmacol* **48**, 335-344 (1994).

47. Liu, M. C., Lin, T. S., Cory, J. G., Cory, A. H. & Sartorelli, A. C. Synthesis and biological activity of 3- and 5-amino derivatives of pyridine-2-carboxaldehyde thiosemicarbazone. *J Med Chem* **39**, 2586-2593 (1996).

48. Koc, A., Wheeler, L. J., Mathews, C. K. & Merrill, G. F. Hydroxyurea arrests DNA replication by a mechanism that preserves basal dNTP pools. *J Biol Chem* **279**, 223-230 (2004).

49. Chitambar, C. R. Gallium compounds as antineoplastic agents. *Curr Opin Oncol* **16**, 547-552 (2004).

50. Kufe, D. W. et al. High-dose thymidine infusions in patients with leukemia and lymphoma. *Blood* **55**, 580-589 (1980).

51. Toledo, L. I. et al. ATR prohibits replication catastrophe by preventing global exhaustion of RPA. *Cell* **155**, 1088-1103 (2013).

52. Grigoryan, R. S., Yang, B., Keshelava, N., Barnhart, J. R. & Reynolds, C. P. Flow cytometry analysis of single-strand DNA damage in neuroblastoma cell lines using the F7-26 monoclonal antibody. *Cytometry A* **71**, 951-960 (2007).

53. Kulkarni, A. & Das, K. C. Differential roles of ATR and ATM in p53, Chk1, and histone H2AX phosphorylation in response to hyperoxia: ATR-dependent ATM activation. *Am J Physiol Lung Cell Mol Physiol* **294**, L998-L1006 (2008).

54. Mankouri, H. W., Huttner, D. & Hickson, I. D. How unfinished business from S-phase affects mitosis and beyond. *EMBO J* **32**, 2661-2671 (2013).

55. Ruiz, S. et al. A Genome-wide CRISPR Screen Identifies CDC25A as a Determinant of Sensitivity to ATR Inhibitors. *Mol Cell* **62**, 307-313 (2016).

56. Talpaz, M. et al. Dasatinib in imatinib-resistant Philadelphia chromosome-positive leukemias. *N Engl J Med* **354**, 2531-2541 (2006).

57. Cohen, A., Barankiewicz, J., Lederman, H. M. & Gelfand, E. W. Purine metabolism in human T lymphocytes: role of the purine nucleoside cycle. *Can J Biochem Cell Biol* **62**, 577-583 (1984).

58. Laks, D. R. et al. Inhibition of Nucleotide Synthesis Targets Brain Tumor Stem Cells in a Subset of Glioblastoma. *Molecular cancer therapeutics* **15**, 1271-1278 (2016).

59. Kim, W. et al. [18F]CFA as a clinically translatable probe for PET imaging of deoxycytidine kinase activity. *Proc Natl Acad Sci U S A* **113**, 4027-4032 (2016).

60. Radu, C. G. et al. Molecular imaging of lymphoid organs and immune activation by positron emission tomography with a new [18F]-labeled 2'-deoxycytidine analog. *Nat Med* **14**, 783-788 (2008).

61. Shields, A. F. et al. Imaging proliferation in vivo with [F-18]FLT and positron emission tomography. *Nat Med* **4**, 1334-1336 (1998).

62. Humphrey, S. J., James, D. E. & Mann, M. Protein Phosphorylation: A Major Switch Mechanism for Metabolic Regulation. *Trends Endocrinol Metab* **26**, 676-687 (2015).

63. Tang, L.-Y. et al. Quantitative phosphoproteome profiling of Wnt3a-mediated signaling network indicating the involvement of ribonucleoside-diphosphate reductase M2 subunit phosphorylation at residue serine 20 in canonical Wnt signal transduction. *Molecular & Cellular Proteomics* **6**, 1952-1967 (2007).

64. Bunimovich, Y. L. et al. Deoxycytidine kinase augments ATM-Mediated DNA repair and contributes to radiation resistance. *PLoS One* **9**, e104125 (2014).

65. Fokas, E. et al. Targeting ATR in DNA damage response and cancer therapeutics. *Cancer Treat Rev* **40**, 109-117 (2014).

66. Foote, K. M. et al. Discovery of 4-{4-[(3R)-3-Methylmorpholin-4-yl]-6-[1-(methylsulfonyl)cyclopropyl]pyrimidin-2-yl}-1H-indole (AZ20): a potent and selective inhibitor of ATR protein kinase with monotherapy in vivo antitumor activity. *J Med Chem* **56**, 2125-2138 (2013).

67. Reaper, P. M. et al. Selective killing of ATM- or p53-deficient cancer cells through inhibition of ATR. *Nat Chem Biol* **7**, 428-430 (2011).

68. Humbert, P. O. et al. E2f3 is critical for normal cellular proliferation. *Genes Dev* **14**, 690-703 (2000).

69. Ishida, S. et al. Role for E2F in control of both DNA replication and mitotic functions as revealed from DNA microarray analysis. *Mol Cell Biol* **21**, 4684-4699 (2001).

CHAPTER 2

Development and preclinical pharmacology of a novel dCK inhibitor, DI-87

ABSTRACT

Introduction: Deoxycytidine kinase (dCK) is essential for DNA synthesis through salvage pathways and DI-87 is a novel dCK inhibitor in preclinical development.

Methods: Following synthesis, DI-87 was tested in cell culture to determine *in vitro* IC50 and protein binding. Oral DI-87 was administered to NSG mice with plasma and tumor PK assessed over 24 hrs by mass spectrometry. NSG mice with CEM tumors were administered varying doses of DI-87 followed by the [^{18}F]CFA PET probe and PET imaging. NSG mice with CEM tumors were administered oral DI-87 and intraperitoneal thymidine concurrently and tumor growth monitored.

Results: The R-enantiomer had an *in vitro* EC50 of 10.2 nM with relatively low protein binding and was used for subsequent studies. Peak DI-87 plasma concentrations were observed between 1-3 hr and 3-9hr in plasma and tumor, respectively. Tumor concentrations were less than one third of plasma concentrations. Full dCK inhibition by PET imaging occurred between 10 and 25 mg/kg and decreasing doses led to faster recovery of activity. Full recovery of enzyme activity occurred by 36 hr with full inhibition being maintained at the 12 hr time point at the 25 mg/kg dose. Maximal growth inhibition occurred with full dCK inhibition over the dosing range (25 mg/kg BID) when DI-87 was given in combination therapy with thymidine; thus increased doses led to more persistent dCK inhibition with predictable increased growth inhibition.

Conclusions: DI-87 is a promising new compound for combination therapy for tumors expressing DCK.

INTRODUCTION

Nucleotide biosynthesis is essential for growing tumors and consists of redundant and convergent biosynthesis pathways. Deoxyribonucelotide triphosphates (dNTPs) are required for DNA replication and repair. They can be synthesized either *de novo* or via salvage pathways. The *de novo* pathway produces dNTPs from glucose and amino acids. It is dependent on ribonucleotide reductase (RNR) which is the rate limiting step in this pathway (1). Therapeutics have been developed to block RNR such as 3-aminopyridine-2-carboxaldehyde thiosemicarbazone (3AP) (2), however tumors develop resistance through upregulation of salvage pathways which produce dNTPs from preformed deoxyribonucelosides in the extracellular environment. Deoxycytidine kinase (dCK) is an enzyme important in the production of deoxycytidine triphosphate (dCTP). DI-39, a reversible high-affinity dCK inhibitor, has previously been shown to inhibit tumor growth when given in combination therapy with thymidine to mice with acute lymphoblastic leukemia (ALL) xenografts (3). DI-87 is novel small molecule dCK inhibitor developed to be more soluble and metabolically stable than DI-39.

Positron emission tomography (PET) scanning and tracers can assist in assessing drug effects on target pathways. [^{18}F]Clofarabine ([^{18}F]CFA) has previously been developed as a PET probe for dCK inhibition (4) and has higher specificity for human dCK compared to previous generation PET probes. This probe is a purine analog which is phosphorylated by dCK to form CFA-PO4 and retained in cells thereby generating PET detectable signal. Such tracers can help determine dose-response relationships by directly interrogating the target pathway being altered by the drug. As a salvage pathway important for nucleotide synthesis in healthy tissue, it is important to characterize dose-response relationships for dCK inhibition to determine the optimal inhibition necessary to maximally suppress tumor growth without leading to excess toxicity.

The aim of the current study is to provide a better understanding of preclinical pharmacokinetics and dose-response relationships of the prototype dCK inhibitor, DI-87. The study utilizes PET imaging to measure dCK inhibition and PK-PD modeling to quantify relationships between drug levels in tissue and plasma with dCK activity and tumor shrinkage.

METHODS AND MATERIALS

General chemical methods: Unless otherwise noted, reactions were carried out in oven-dried glassware under an atmosphere of nitrogen using commercially available anhydrous solvents. Solvents used for extractions and chromatography were not anhydrous. 4,6-diamino-2-mercaptopyrimidine was obtained from drying the hydrate over dynamic vacuum at 110 °C for 20 h. All other reagents obtained from commercial suppliers were reagent grade and used without further purification unless specified. Reactions and chromatography fractions were analyzed by thin-layer chromatography (TLC) using Merck precoated silica gel 60 F254 glass plates (250 μm). Visualization was carried out with ultraviolet light, vanillin stain, permanganate stain, or p-anisaldehyde stain. Flash column chromatography was performed using E. Merck silica gel 60 (230−400 mesh) with compressed air. All compounds were characterized by 1H and 13C NMR recorded on ARX500 (500 MHz) or Avance500 (500 MHz) spectrometers, and electrospray mass spectrometry data were collected with a Waters LCT Premier XE time-of-flight instrument controlled by MassLynx 4.1 software. Samples were dissolved in methanol and infused using direct loop injection from a Waters Acquity UPLC into the Multi-Mode Ionization source. The purity of all final compounds was determined to be >95%. Analytical HPLC analysis was performed on a Knauer Smartline HPLC system with a Phenomenex reverse-phase Luna column (5 μm, 4.6 × 250 mm) with inline Knauer UV (254 nm) detector. Mobile phase: A: 0.1% TFA in H2O, B: 0.1% TFA in MeCN.

Synthesis of 4-methoxy-3-(2-morpholinoethoxy)benzonitrile (1). To a solution containing 4-methoxy-3-hydroxybenzonitrile and Cs_2CO_3 (1.5 eq) was added 4-(2-chloroethyl)morpholine hydrochloride (1.5 eq). The reaction solution was stirred at 70 °C for 12 hours, quenched with DI water, extracted with ethyl acetate and purified by flash chromatography.

Synthesis of 4-methoxy-3-(2-morpholinoethoxy)benzothioamide (2). To a solution of **1** in pyridine was added Et_3N (1.1 eq) and ammonium sulfide solution (20 wt% in water, 3.0 eq). Reaction solution was stirred for 12 hours at 60 °C, concentrated en vacuo, and the resulting residue was taken up in ethyl acetate and washed with DI water and brine. The organic layer was concentrated and purified by flash chromatography.

Synthesis of 1-(2-(4-methoxy-3-(2-morpholinoethoxy)phenyl)-5-methylthiazol-4-yl)ethan-1-one (3). To a solution of **2** in ethanol was added 4-bromopentane-2,3-dione (1.5 eq)

and reaction solution heated to reflux for 4 hours. The reaction solution was then concentrated en vacuo, and the resulting residue was purified by flash chromatography.

Synthesis of (S)-1-(2-(4-methoxy-3-(2-morpholinoethoxy)phenyl)-5-methylthiazol-4-yl)ethan-1-ol (4). To a solution of (*R*)-(+)-2-methyl-CBS-oxazaborolidine (9.0 eq) in THF at -78 °C was added borane–THF complex (1.0M solution in THF, 6.0 eq), followed by a solution of **3** (1.0 eq) in THF. Upon completion, reaction was quenched with DI water and concentrated en vacuo. The resulting residue was concentrated by flash chromatography.

Synthesis of (S)-1-(2-(4-methoxy-3-(2-morpholinoethoxy)phenyl)-5-methylthiazol-4-yl)ethyl 2,2,2-trifluoroacetate (5). To a solution of **4** in DCM at 0 °C was added trifluoroacetic anhydride (TFAA, 5.0 eq) dropwise and stirred for 30 minutes. Reaction solution then allowed to room temperature prior to quenching with a saturated aqueous solution of sodium bicarbonate, which was extracted with ethyl acetate. Organic layer washed with brine, concentrated, and used directly in next step due to instability of the trifluoroacetate.

Synthesis of (R)-2-((1-(2-(4-methoxy-3-(2-morpholinoethoxy)phenyl)-5-methylthiazol-4-yl)ethyl)thio)pyrimidine-4,6-diamine (6, (*R*)-DI-87). To a solution of **5** in DMF was added 4,6-diamino-2-mercaptopyrimidine (1.5 eq) and reaction solution stirred at 80 °C. Upon completion, reaction solution was concentrated en vacuo and purified by flash chromatography. Additional purification by chiral reverse-phase liquid chromatography afforded (*R*)-DI-87 in >99% ee.

[MOVE DETAILS OF SYNTHESIS TO APPENDIX??] – Shall we make a new section?

dCK Uptake Assay Performed in Cell Culture: Cells were seeded at a density of 50,000 cells/ well in Millipore MultiScreen GV 96 well plates. 0.25 µCi of 3 H-dC (Moravek Biochemicals) were added to the cells simultaneously with concentrations of dCK inhibitor at a final volume of 100 µL/well. After 1 h at 37 °C, cells were washed four times with ice cold phosphate-buffered saline (PBS) using the Millipore Vacuum Manifold. The amount of incorporated probe was measured by scintillation counting with the PerkinElmer Microbeta.

Cell proliferation assay: Cells were plated at $1x10^3$ cells / well in at 50 µl / well in white opaque 384-well plates and treated as described. Following incubation with 10 nM Gemcitabine ± 1 µM (R)-DI-87 for 72 hours, 50 µl of CellTiter-Glo reagent (Diluted 1:5 in dH_2O) was added to each

well, plates incubated at room temperature for 5 m and luminescence was measured using a BioTek microplate luminescence reader.

Animals: Animal studies were conducted under the approval of the UCLA Animal Research Committee and were performed in accordance with the guidelines from the Division of Laboratory Animal Medicine at UCLA. All NOD scid gamma (NSG) mice were purchased from the UCLA Radiation Oncology breeding colony.

Mouse xenograft tumor models and treatments: Mice had three separate evaluation protocols which included pharmacokinetics, dCK activity, and growth inhibition studies. The human cell line CCRF-CEM (CEM) was purchased from American Type Culture Collection (ATCC). The cell line was maintained in 10% FBS in RPMI-1640 and were grown at 37°C, 20% O_2, and 5% CO_2. CEM tumor xenografts were developed in 8-12 week-old male or female NSG mice by implanting 2×10^6 CEM cells in 100 µL of a 50/50 (vol/vol) mixture of PBS and matrigel (BD Biosciences) for subcutaneous injections in left shoulders (for imaging and PK studies) or both shoulders (for growth inhibition studies). (R)-DI-87 (dCKi, Sundia Pharmaceuticals) was administered by oral gavage to recipient animals. For oral administration of (R)-DI-87, the drug was solubilized in the formulation containing PEG-200: Transcutol: Labrasol: Tween-80 mixed in 5:3:1:1 ratio. For imaging studies, the mice were treated with indicated doses of (R)-DI-87 after the tumor size reached 250 mm^3. For growth inhibition and pharmacokinetic studies, treatments were started after the tumors reached 50 mm^3.

Pharmacokinetic studies of (R)-DI-87 in mice: (R)-DI-87 plasma and tumor concentrations were assessed at 1, 3, 6, 9 and 24 h following oral administration of 10, 25, or 50 mg/kg of (R)-DI-87 to female NSG mice with CEM tumors (N=5 mice per time point). At each time point, a cohort of mice was sacrificed by cervical dislocation; thus, a single plasma and tumor concentration were obtained from each mouse. Blood samples were collected in heparin-EDTA tubes by the retro-orbital technique and spun at 6000 x g for 15 min prior to collecting the plasma supernatants. All plasma samples were frozen down at –20ºC before sample processing. The stock solutions of (R)-DI-87 and DI-82 (internal standard) were prepared by dissolving the appropriate amount of each drug in a known volume of dimethyl sulfoxide (DMSO) to a 10 mM concentration and were stored at –20ºC before use. DI-82 (internal standard) was diluted to 200 nM in methanol to make the internal solution. The calibration standards were prepared by spiking working stock solutions of (R)-DI-87 in plasma from untreated mice to give 0.01-10 pmol/µL range. Each 20 µL calibration standard sample was mixed with 60 µL of internal solution (methanol with 200 nM internal standard) and vortexed for

30 s. Following centrifugation at 15,000 x g for 10 min, approximately 60 µL of sample was carefully transferred into HPLC injector vials for LC-MS/MS-MRM analysis. Plasma samples were processed the same way as the calibration standard samples. 20 µL samples were injected onto a reverse phase column, (Thermo Scientific Hypersil GOLD column 3.0 µm; 2.1 x 100 mm) equilibrated in 0.1% water/formic acid, and eluted (200 µL/min) with an increasing concentration of solvent B (acetonitrile/formic acid, 100/0.1, v/v: min/% acetonitrile; 0/0, 5/0, 15/60, 16/100, 19/100, 20/0, and 25/0). The effluent from the column was directed to the Agilent Jet Stream ion source connected to the triple quadrupole mass spectrometer (Agilent 6460) operating in the multiple reaction monitoring (MRM) mode using previously optimized settings. The following drug precursor→fragment ion transitions were used: DI-82 (511→369), (R)-DI-87(503→361). The peak areas for each drug (precursor→fragment ion transitions) at predetermined retention times were recorded using the software supplied by the instrument manufacturer (Agilent MassHunter) (5).

Tumors were harvested after dissection of mice, weighed, and snap-frozen in liquid nitrogen. PBS containing internal standard (200 µL for 50 mg tumor) was added to the excised tumor and homogenized using a bead beater (BioSpec). The samples were spun down to collect supernatants. The supernatant was further diluted 5 times in PBS (with internal standard), and four parts of methanol (with internal standard) was added and incubated -80ºC overnight to precipitate proteins. The samples were spun at maximum speed (16000g) at 4ºC, and supernatant collected. Twenty microliter samples were injected onto a reverse phase column equilibrated in water 0.1% formic acid for LC-MS/MS-MRM analysis in positive ion mode as above and compared to calibration standards.

DCK activity with MicroPET/CT: DCK activity was evaluated following oral administration of 5, 10, or 25 mg/kg of DI-87 to male NSG mice implanted with CEM tumors (N=4 mice per time point). The NSG mice were anesthetized 3 hours prior to imaging and intravenously administered 740 kBq of [^{18}F]CFA PET probe (4). Thus each mouse was representative of a single time point and concentration. MicroPET/CT experiments were conducted using G8 microPET/CT system (6,7). The mice were then positioned in an imaging chamber and data was acquired with the G8 microPET/CT system (Sofie Biosciences). MicroPET data was acquired for 10 min and reconstructed with a statistical maximum *a posteriori* probability algorithm (MAP) into multiple frames. The spatial resolution of PET is ~1.5 mm with 0.4 mm voxel size. CT images are a low-dose 400 µm resolution acquisition with 200 µm voxel size. MicroPET and CT images were co-registered and then quantified by manually drawing three-dimensional regions

of interest using Osirix software. The color scale was proportional to tissue concentration, with red being the highest and yellow, green and blue corresponding to the lower values.

Growth inhibition studies: Male NSG mice implanted with CEM tumors as above were used for the growth inhibition studies. Combination therapy with DI-87 and thymidine were used Treatments of (R)-DI-87 and/or thymidine were started after the tumors reached 50 mm^3. (R)-DI-87 was administered at varying doses orally once a day (QD) or twice a day (BID) for 16-18 days while thymidine (2 g/kg) solubilized in saline was administered intraperitoneally BID after start of treatment (3). Control mice received either thymidine intraperitoneal saline (i.p.) injections alone, oral (R)-DI-87 with i.p saline injections, or i.p. thymidine alone. Tumor growth CT measurements were compared among different treatment groups (n=5 mice or 10 tumors/ group). Tumor growth was monitored daily by caliper measurements ([(length × width2)/2]) and bi-weekly by CT measurements.

Pharmacokinetic and pharmacodynamic modeling: Using the computer program NONMEM (version 7.3) with a GNU Fortran G77 Compiler, DI-87 concentration-time data were modeled using first-order conditional estimation method (FOCE) with interaction. Plasma concentrations were assessed with standard PK models which included a depot compartment representing the gut. Tumor concentrations were evaluated with the additional of a separate tumor compartment once plasma concentrations had been characterized (ADVAN6, TRANS1 subroutine). An exponential-normal distribution error model was used for inter-subject variability.

A combined pharmacokinetic-pharmacodynamic (PK-PD) model was developed using the final DI87 plasma-tumor PK parameter estimates (Figure 1). The effect compartment (DCK inhibition or growth inhibition) was linked to the tumor concentrations. Linear (slope), Emax, and sigmoid Emax models were tested to determine which were the best fits to the data (see equations below) (8). The final model was used to simulate DCK inhibition and growth inhibition from a representative mouse for each of the tested DI-87 concentrations.

PD models:

A. Linear (Slope): SLOPE*CONC

B. Emax: Emax*CONC/(EC50+CONC)

C. Sigmoid Emax: $Emax*(CONC^{EXP})/(EC50^{EXP}+CONC^{EXP})$

RESULTS

Development of a highly potent, orally bioavailable dCK inhibitor, (*R*)-DI-87

(*R*)-DI-87 (Figure 2A) was synthesized as follows: an SN2 reaction between 4-methoxy-3-hydroxybenzonitrile and 4-(2-chloroethyl) morpholine furnished **1**. Heating with an aqueous solution of ammonium sulfide gave thioamide **2**, which was subjected to Hantzsch thioazole formation conditions to yield thiazole **3**. Asymmetric Corey-Bakshi-Shibata (CBS) reduction of the ketone resulted in the *S*-alcohol **4**, which was converted into the trifluoroacetate **5** and displaced *via* SN2 reaction by 4,6-diamino-2-mercaptopyrimidine to furnish (*R*)-DI-87 (**6**) (Figure 2B). The IC50 values for each enantiomer of DI-87 were determined using a dC uptake assay in CEM cells. (*S*)-DI-87 exhibited a much higher IC50 value (468±2.1 nM) relative to (*R*)-DI-87 (3.15±1.2 nM) (Figure 2C). (*R*)-DI-87 treatment rescued CEM cells from the anti-proliferative effects of gemcitabine, a dCK-dependent nucleoside analog prodrug, with an EC50 of 10.2 nM **(**Figure 2D). Additionally, we observed that protein binding of (*R*)-DI-87 is comparatively lower than its predecessor, (*R*)-DI-82, as measured by IC50 of the respective dCK inhibitor in presence of bovine serum albumin (BSA) (Figure 2E).

Pharmacokinetics of DI-87

DI-87 concentrations in plasma and tumor were determined for 3 dose levels (10, 25, and 50 mg/kg) (Figure 3). Plasma and tumor concentrations were obtained at a single time point from each mouse. Plasma DI-87 concentrations exhibited linear PK and increased proportionally with higher doses. Plasma concentrations peaked between 1 and 3 hours. Tumor concentrations were lower than plasma concentrations and had a later, more sustained peak at 3-9 hours. Tumor concentrations varied with tumor size, but overall exhibited linear pharmacokinetics. In particular, the 50 mg/kg dose was administered to mice with larger tumors (>1.5 cm^3), so although the tumor concentrations were similar to the 25 mg/kg dose, the total drug amount in the tumors was higher for the 50 mg/kg dose. Plasma and tumor PK was also evaluated in male mice at the 10 mg/kg dose with essentially identical results to that seen in female mice (data not shown).

A population PK model was initially developed for plasma concentrations. A one compartment structural model fit the data well. An additional compartment was added to model tumor concentrations. The parameter estimates for the combined tumor and plasma population PK model are shown in Table 1. KA was fixed to the parameter estimate obtained from the plasma PK model. The typical value of clearance was 0.46 L/hr/kg and plasma volume of distribution was 2.78 L/kg. Actual tumor volumes were used for the tumor volume in the model. Plasma concentrations were over 3.5 fold higher than tumor concentrations.

DCK inhibition studies

DI-87 was administered to mice in three separate doses (25 mg/kg, 10 mg/kg and 5 mg/kg) to establish a dose response curve. The [^{18}F]CFA PET probe was administered 3 hours prior to imaging. Representative mice at each time point and concentration are shown in Figure 4A. The data from all mice is represented graphically in Figure 4B. The dose of 25 mg/kg exhibits full DCK inhibition until 27 hrs after the dose and activity fully recovers at 36 hrs. The 10 mg/kg dose results in full inhibition with recovery initiating at the 12 hr time point. The 5 mg/kg dose results in minimal DCK inhibition with rapid recovery.

The PET signal intensity quantitative data was used in a combined population PK-PD model. PK parameters from the final combined plasma-tumor model were fixed and PD parameters were estimated in NONMEM. A sigmoid Emax indirect response PD model (9) was found to fit the DCK inhibition data the best:

DA/DT=Kin *(1- Sigmoid Emax) - Kout*A

Final parameter estimates from the model are shown in Table 1f. Emax was 1.20 and EC50 was 0.31 mcg/mL. The Hill coefficient was 58.6 consistent with the full DCKi seen at the 6 hr time point for the 25 and 10 mg/kg doses and represents that DCK inhibition is essentially a step function at higher concentrations with the transition from no inhibition to full inhibition being achieved over a relatively narrow range of concentrations. Figure 4C is a simulation of the final model to demonstrate PET signal intensity and the dose response curve for DCK inhibition seen with the 5, 10, and 25 mg/kg doses.

Growth inhibition studies

Based on the results of the DCK inhibition experiments, we predicted close to full DCK inhibition with 25 mg/kg DI-87 and performed growth inhibition studies with 25 mg/kg daily of DI-87 in combination with a fixed dose of i.p. thymidine since DI-87 alone exhibits minimal growth inhibition. DI-87 at 10 mg/kg (oral) was given in combination with i.p. thymidine to demonstrate a dose-response relationship with reduced DCKi inhibition. Control mice received either intraperitoneal (i.p.) saline injections alone, oral DI-87 with i.p saline injections, or thymidine alone. A second experiment was performed to validate the results and explore full DCK inhibition throughout the dosing interval with 25 mg/kg BID of DI-87 administered in combination with a fixed dose of thymidine. DI-87 at 10 mg/kg was again given in combination with i.p. thymidine to demonstrate a dose-response relationship with reduced DCKi inhibition and the same controls were used as experiment 1. Tumor size was measured every 3 days after the

initiation of drug administration. Mice administered thymidine alone or DI-87 alone had similar tumor growth curves to the control (data not shown). Increasing DI-87 doses resulted in reduced cell growth in both experiments consistent with the DCK inhibition seen in the PET scans (Figure 5A).

The tumor sizes from both experiments were used in a combined PK-PD model. PK parameters from the final combined plasma-tumor model were fixed and PD parameters were estimated in NONMEM. A superexponential function was found to describe the growth of the control data the best: $Growth(t)=exp(k1*t^{k2})$. An Emax indirect response PD model (9) was found fit the growth inhibition data the best:

DA/DT=KIN - KOUT * (1 + Emax)-(56*k1*k2*(TIME**(k2-1))))*A

Final parameter estimates from the model are shown in Table 1. Emax was 1.06 and EC50 was 3.63 mcg/mL. The final model was used for simulations of the three concentrations tests (10 mg/kg daily, 25 mg/kg daily, 25 mg/kg BID). Figure 5B demonstrates that the final model fit the experimental data well. Thus, more growth inhibition results from maximal DCK inhibition over the 24 hr dosing period consistent with the 25 mg/kg BID dose.

DISCUSSION

Restricting the amount of dNTPs available for incorporation into newly synthesized DNA leads to replication stress, which can be therapeutically leveraged against rapidly replicating malignant cells. Cancer cells can utilize either *de novo* and salvage biosynthesis of dNTPs, meaning that any therapeutic strategy attempting to restrict their supply must simultaneously inhibit both pathways – this may explain the limited clinical efficacy of inhibiting RNR, a key enzyme in the *de novo* pathway. We therefore developed pharmacological inhibitors of dCK, the rate-limiting enzyme in the salvage pathway biosynthesis of dCTP, to be used in combination with RNR inhibition. We have previously reported the development of DI-39 (3) and DI-82 (Nomme et al., 2014), potent inhibitors of dCK (dCKi) which had poor solubility and sub-optimal drug-like properties. To address these shortcomings, we developed (*R*)-DI-87, a potent, specific, soluble, and bioavailable dCK inhibitor which has recently gained FDA IND approval and will be evaluated in clinical trials shortly.

In line with our previous studies, we determined that the *R*-enantiomer of DI-87 had a significantly higher affinity for dCK when compared with the *S*-enantiomer. The affinity of DI-87 for dCK was further confirmed through a rescue assay in which the growth of CEM cells treated with gemcitabine with and without DI-87 supplementation was monitored. Supplementation with DI-87 led to a complete rescue of growth, indicating that the activity of dCK, the key enzyme responsible for the cytotoxic effects of gemcitabine, was being blocked. Previous generations of reversible dCK inhibitors developed by our group had comparable potency, but did not have optimal biochemical properties. In particular, DI-82 was an effective dCK inhibitor but was heavily protein bound. By comparison, DI-87 was significantly more potent in the presence of bovine serum albumin.

We evaluated the preclinical pharmacology of DI-87. Plasma and tumor concentrations of DI-87 exhibited linear PK. Plasma concentrations peaked 3 hours after administration, while tumor concentrations remained at peak levels between hours 3 and 9. Thus, the tumor-to-plasma concentration ratio changed depending upon sampling time. Tumor concentrations were significantly lower than plasma concentrations for all concentrations observed. The PET probe [^{18}F]CFA was used to quantify dCK activity in tumors and thus effects on the target pathway. Given the differential peaks in plasma and tumor concentrations, linking DI-87 tumor concentrations to dCK inhibition provided a more physiologic and mechanistic approach. Our population PK-PD modeling allowed us to describe limited tumor data and link these concentrations to dCK inhibition. Full dCK inhibition was observed over a range of concentrations and decreasing doses led to faster recovery of activity. At the highest dose

tested, full recovery of enzyme activity occurred by 36 hours with full inhibition being maintained at the 12 hour time point. Our PK-PD model suggested a threshold or rapid switching on-off effect. Maximal growth inhibition occurred with full dCK inhibition over the dosing range when DI-87 was given in combination therapy with thymidine, and lower doses led to diminished dCK inhibition with predictable decrease in growth inhibition.

dCK is an intriguing target in anti-cancer therapy, as it is a rate limiting enzyme within the salvage pathway of dNTP biosynthesis, and multiple cell lines in the Cancer Cell Line Encyclopedia and tumor samples from The Cancer Genome Atlas express this enzyme at higher levels when compared to normal tissues (10). Among the listed cancers, leukemias and lymphomas are most prominently featured. While targeting the salvage pathway of dNTP biosynthesis through dCK inhibition is a relatively new approach, the key enzyme of the parallel *de novo* pathway, ribonucleotide reductase (RNR), has been an important target in anticancer therapies for decades. The RNR inhibitor hydroxyurea (HU) has been used in clinics worldwide and continues to progress to clinical phase studies, as Triapine (3-AP). While these compounds are able to inhibit RNR, they each possess dose-limiting toxicity and limited efficacy. A major resistance mechanism to RNR inhibition therapy is presence of an active dCK-mediated salvage pathway, which may explain the failure of RNR inhibitors such as 3-AP in clinical trials. In an effort to circumvent this resistance mechanism, we developed inhibitors of dCK and demonstrated that combined administration with RNR inhibitors significantly improved their therapeutic efficacy.

While the previously developed DI-39 and DI-82 had suboptimal pharmacologic properties, they remained effective dCK inhibitors. DI-87 improves upon these properties while maintaining low-nM affinity for dCK. When evaluated as single agents, these dCK inhibitors were well tolerated at higher doses in preclinical studies, but had essentially no ability to inhibit growth (data not shown). By blocking dCK, the kinase required for the metabolic switch to nucleotide salvage pathway dCTP synthesis, in combination with blockade of the *de novo* pathway using thymidine as an inhibitor of RNR, we were able to achieve growth inhibition at higher doses of combination therapy over the course of the growth inhibition study. The current study evaluated an ALL xenograft, the CEM cell line, however dCK has been shown to be active in a wide variety of tumors cells including lymphomas, colon cancer, and gastric cancer (11,12). DI-87 thus appears to have potential as a cancer therapeutic in combination therapy.

Pre-clinical studies are used to guide first-in-human phase I clinical trials, and several algorithms are used for determining the appropriate dose of a therapeutic agent. One approach

utilizes one-tenth of the dose that results in 10% lethality (LD10) in mice as a starting dose. However, if toxicology studies in non-rodent species show significant toxicity or limited lethality, one sixth to one third of the lowest dose that results in toxicity, the toxic dose low (TDL), is used as the starting dose (13). While these guidelines have been used for cytotoxic chemotherapy, appropriate rules and models to use for first-in-human studies of molecularly targeted agents are less clear (14) and use in combination further complicates choosing the initial first dose in humans. Molecularly targeted therapies can often result in significantly lower toxicity compared with cytotoxic chemotherapy, thus the use of LD10 may result in a very high recommended first dose since effective doses may be much lower than the maximum tolerable dose due to maximal target engagement and receptor occupancy (15). The dosing schedule will also require optimization based on maintaining inhibition rather than recovery from toxicity. Thus understanding and optimizing dosing based on mechanisms of action for molecularly targeted therapies is essential in preclinical and clinical drug development (16).

The PET probe used in the current study is a tool to help provide mechanistically driven rational dosing of DI-87 and similar compounds prior to clinical trials. The use of non-invasive PET probes and scans can greatly aid in drug development. Imaging studies in early phase development can confirm that molecules reach the target tissue, do not accumulate in target sites, determine dose-target occupancy, and help critically evaluate similar drug candidates based on responses (17). Our group developed [^{18}F]FAC (1-(2'-deoxy-2'-[^{18}F]fluoro-β-D-arabinofuranosyl)cytosine) as the first dCK specific PET probe (6). This compound has been used in preclinical drug development of small molecule dCK inhibitors (18). We subsequently developed a more specific probe, [^{18}F]CFA, which was used in the current study to evaluate dCK activity in tumors when given a small molecule dCK inhibitor. This probe is also being studied in a clinical trial to evaluate changes in dCK activity with cancer immunotherapy at our institution (19). PET probes in preclinical and clinical studies can aid in understanding how drug distribution in target tissues and response on the target pathway is modified in the presence of multiple drugs as compared to single agent therapy. They can help evaluate the degree of synergy, appropriate timing of therapies, and dosing amount. Our growth inhibition studies utilized a fixed dose of thymidine with varying doses of DI-87 and dual inhibition led to effective growth inhibition when full dCK inhibition was achieved throughout the dosing interval.

The current study was limited in that each time point represented a separate mouse since the half-life of the probe did not allow for multiple images within the same mouse. The probe required time for optimal diffusion in the tumor, thus we were unable to quantify dCK inhibition at very early time points. PK in the tumor was evaluated in separate mice rather than using a

probe to follow drug levels over time. However similar results were obtained between replicate experiments and results between mice were similar at each time point, thus this was unlikely to be a major limitation. While a fixed dose of intraperitoneal thymidine was used for growth inhibition in the current study, either an IV or oral RNR inhibitor will be necessary for combination therapy in further clinical development.

In summary, the current study describes the preclinical development and pharmacology of a novel dCK inhibitor, DI-87. It provides additional evidence for the value of PET probes in assisting with preclinical drug development. By using a probe specific for dCK activity, we were able to find a DI-87 dose that resulted in maximal dCK inhibition throughout the dosing interval and accurately predict appropriate dosing for growth inhibition studies. We have developed PK-PD models for both dCK inhibition and growth inhibition and both can be used to optimize dosing schedules for preclinical studies. Thus, DI-87 is a promising new compound for combination therapy in tumors expressing DCK.

Table 1: PK-PD modeling parameter estimates

Plasma-Tumor PK model parameters		
	Parameter Estimate	**Standard Error**
CL (L/hr/kg)	0.46	0.03
V (L/kg)	2.78	0.22
KA (hr)	0.66 (FIXED)	.
Q (L/hr/kg)	0.0045	0.0013
Scalar	3.69	0.40
Eta1 (Scalar)	34.6%	0.08
Proportional Error	49.9%	0.04
DCK inhibition PK-PD model		
Kout	0.12	0.00011
Emax	1.20	0.00200
EC50	0.31	0.00009
Gamma (Hill coefficient)	58.60	0.18500
Kin	0.76	0.00078
Additive Error	0.88	0.00025
Growth Inhibition PK-PD Model		
Kout	0.372	0.0973
Emax	1.06	0.2030
Growth Function Exp 1	0.00498	0.0011
Growth Function Exp 2	1.47	0.0399
EC50	3.63	1.19
Intersubject Variability (Emax)	14.1%	2.65%
Additive Error	0.20	0.02

FIGURES

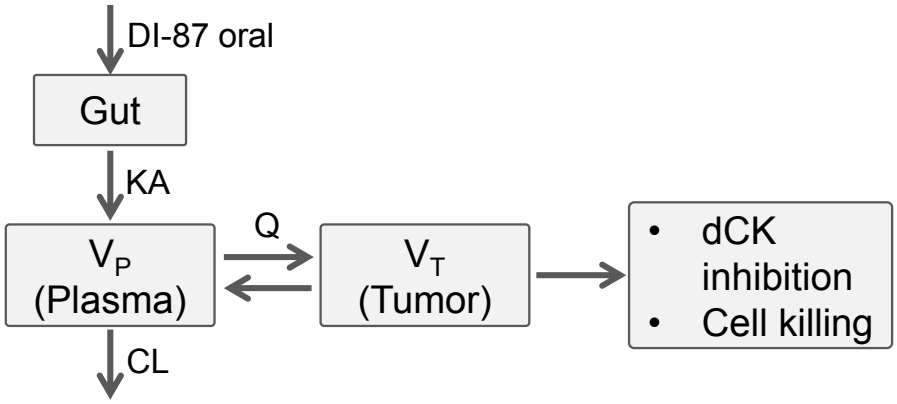

Fig. 2.1. Schematic of population PK-PD model. DI-87 is an oral drug which is absorbed from the gut with an absorption constant (KA). It distributes between the plasma volume (Vp) and tumor volume (Vt) with an intercompartmental clearance Q and is eventually cleared from the plasma compartment (CL). Tumor DI-87 concentrations lead to drug effect (DCK inhibition or growth inhibition). DCK inhibition with modeled with a sigmoid Emax indirect response model while growth inhibition was modeled with an Emax indirect response model.

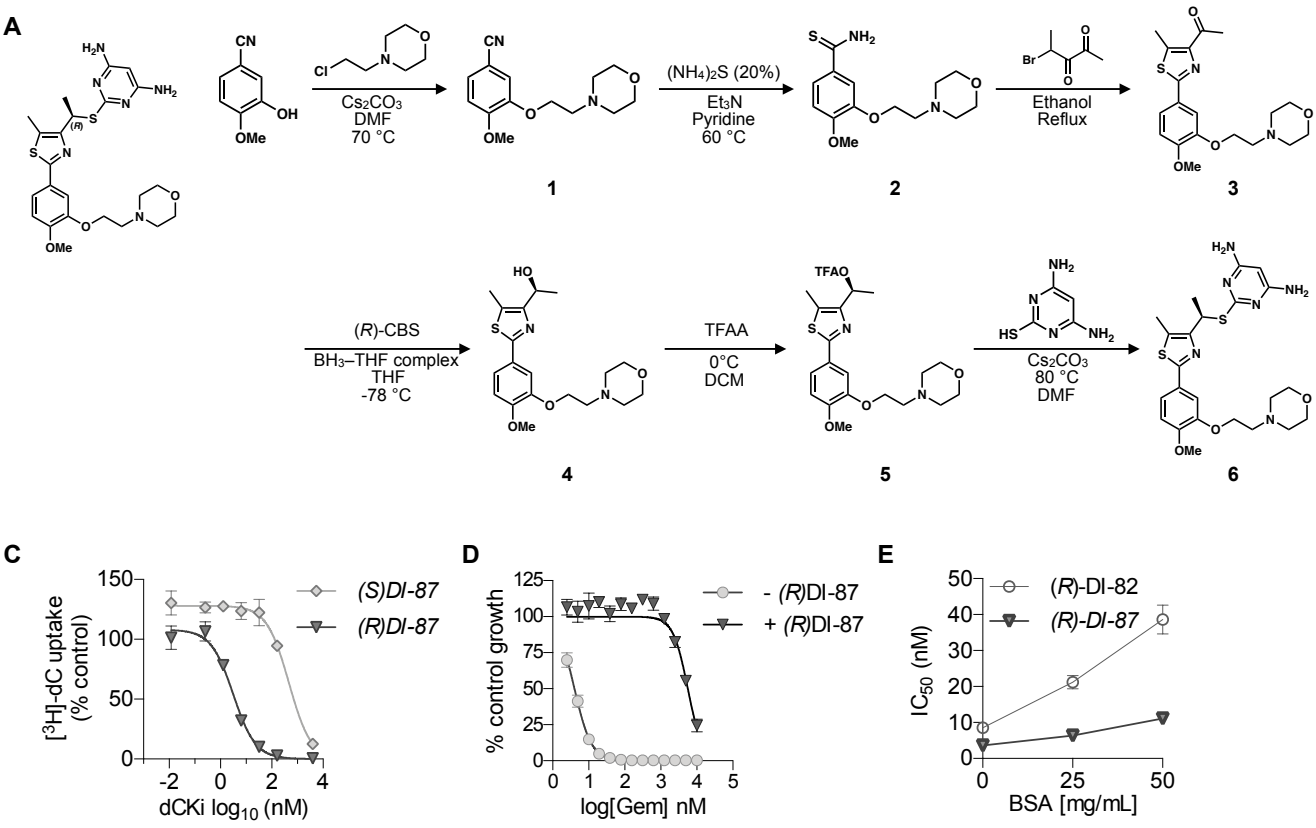

Fig. 2.2. Synthesis and *in vitro* activity of DI-87. (A) Structure of DI87. (B) Synthetic route of DI-87. (C) IC_{50} values determined using ^{3}H-dC uptake assay in CEM T-ALL cells to measure inhibition of dCK activity. (D) Dose response of DI-87 in CEM T-ALL cells treated with 10 nM Gemcitabine (n=4; mean±SD) for 72h determined using Cell Titer Glo. (E) Protein binding of DI-87 and *(R)*DI-82 assessed by comparing IC_{50} of the compounds in presence of 25 and 50 mg/mL BSA (n=2; mean±SD).

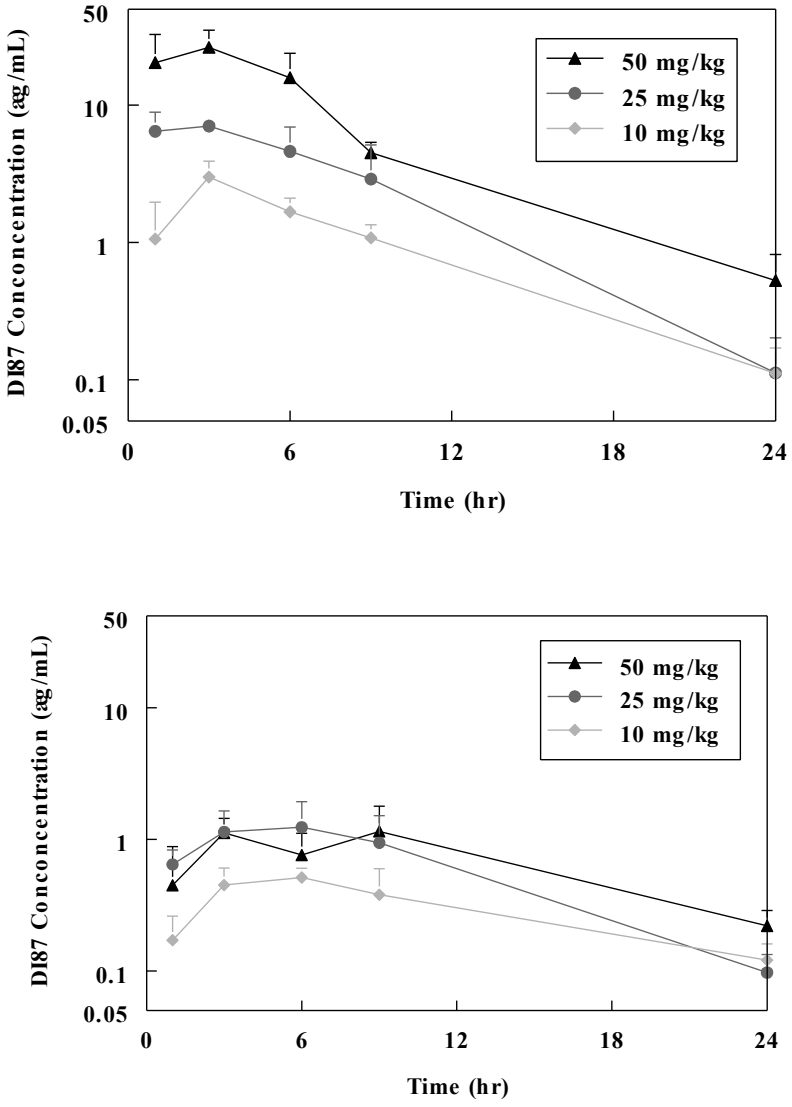

Fig. 2.3. Plasma and tumor concentrations. Each data point represents the plasma and tumor concentrations from a single mouse (n=5 per time point). Plasma concentrations are higher than tumor concentrations and have an earlier peak. Plasma and tumor PK was linear over the range of concentrations studied. Tumor sizes for the 50 mg/kg dose were larger than those for the 25 mg/kg dose resulting in similar mcg/mL concentrations despite more overall drug in the 50 mg/kg dosage tumors.

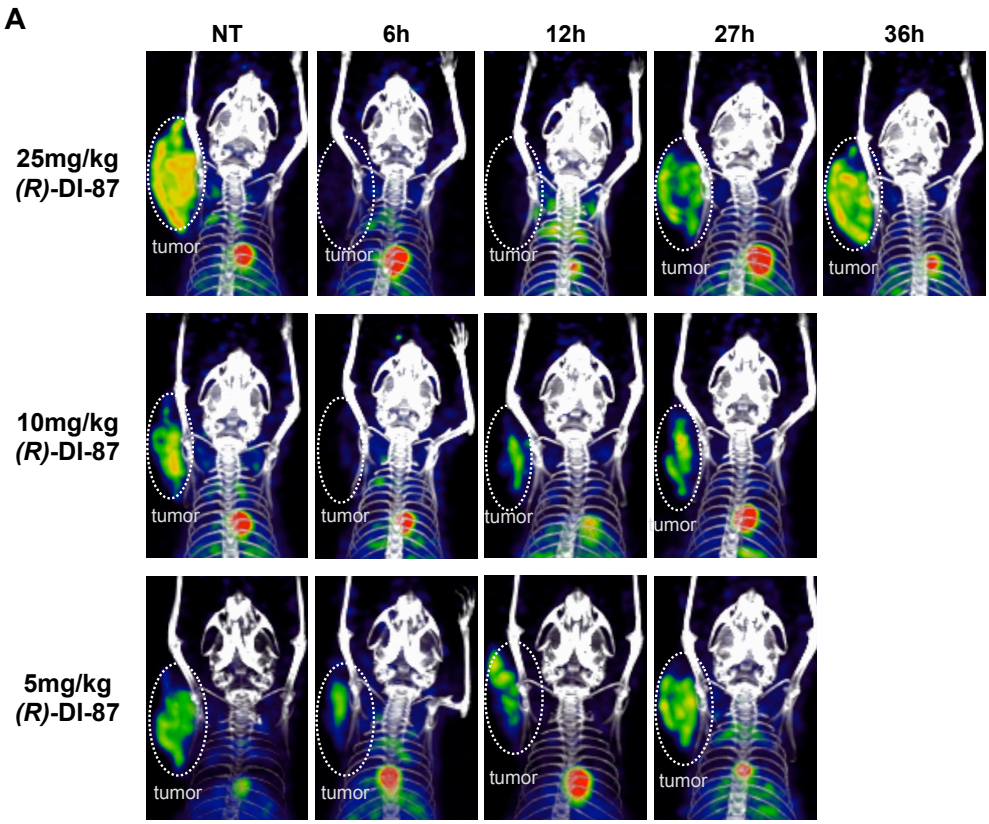
A
NT
6h
12h
27h
36h
25mg/kg
(R)-DI-87
10mg/kg
(R)-DI-87
5mg/kg
(R)-DI-87
tumor

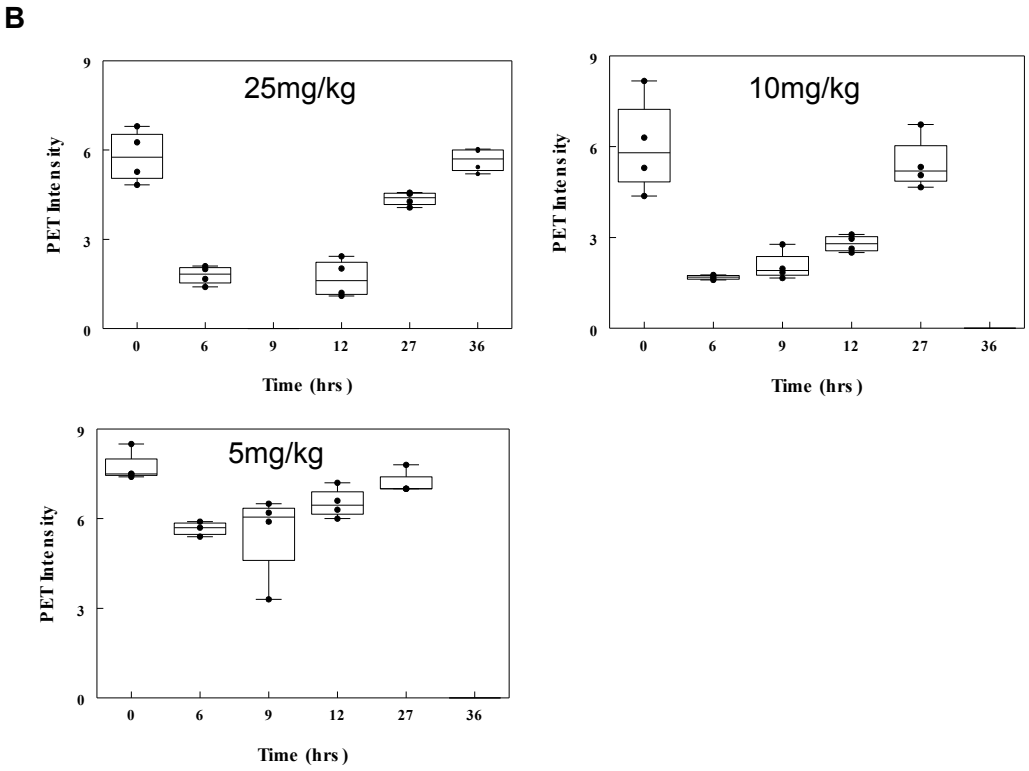
B
25mg/kg
10mg/kg
5mg/kg
PET Intensity
Time (hrs)
0
3
6
9
12
27
36

C

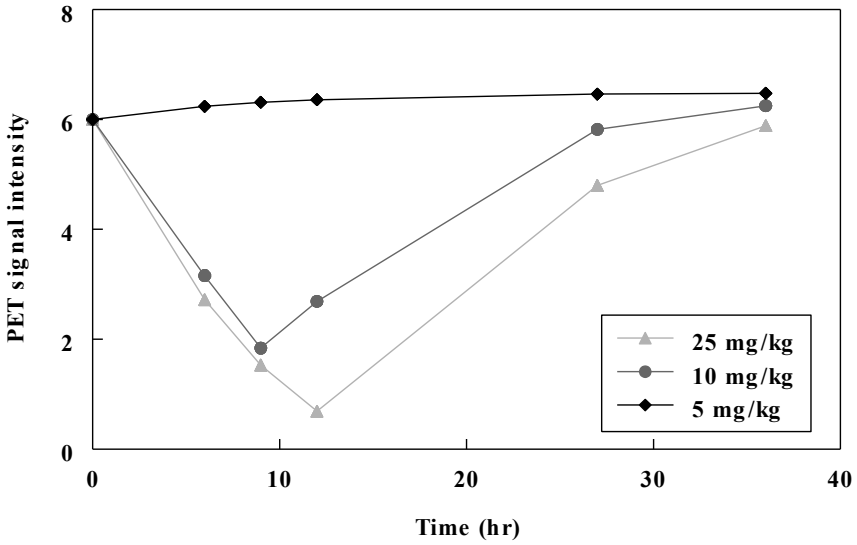

Fig. 2.4. dCK inhibition studies. A. dCK activity in tumors. DI-87 was administered as a single dose to mice and PET scans were completed following drug administration. dCK activity from representative mice over time is shown for 25 mg/kg, 10mg/kg, and 5 mg/kg. B. dCK activity as measured by PET scans. dCK inhibition was prolonged with higher doses of drug (25 mg/kg vs. 10 mg/kg). Minimal inhibition was seen at 5 mg/kg. C. Simulation of dCK activity for three doses of DI-87.

A

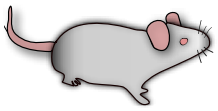

CEM s.c. tumors
in flanks

30 mice
2 tumors each mouse

6 groups
(n=5 mice; 10 tumors)

1. Control
2. dT (2g/kg i.p. b.i.d.)
3. (R)-DI-87 (10mg/kg p.o. q.d.)
4. (R)-DI-87 (25 mg/kg p.o. q.d.)
5. dT + (R)-DI-87 (10 mg/kg)
6. dT + (R)-DI-87 (25 mg/kg)

B

10mg/kg (R)-DI-87

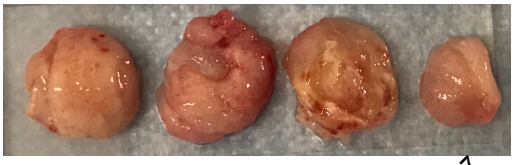

Control (R)-DI-87 dT dT+(R)-DI-87

25mg/kg (R)-DI-87

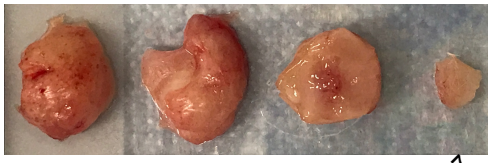

Control (R)-DI-87 dT dT+(R)-DI-87

C

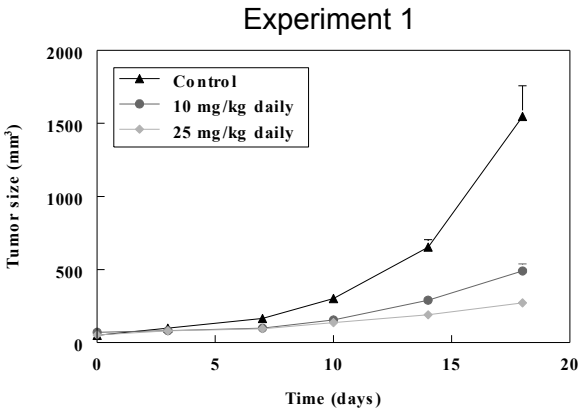

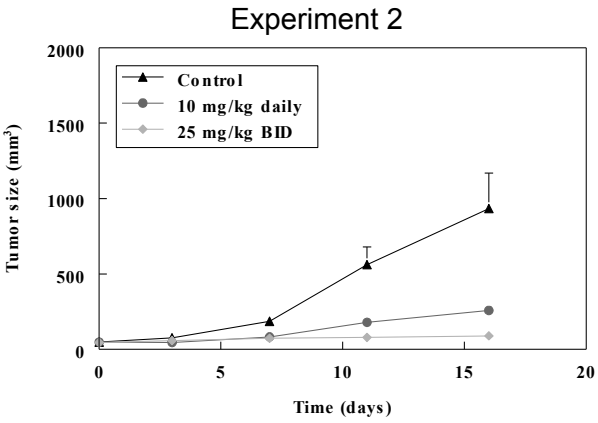

D

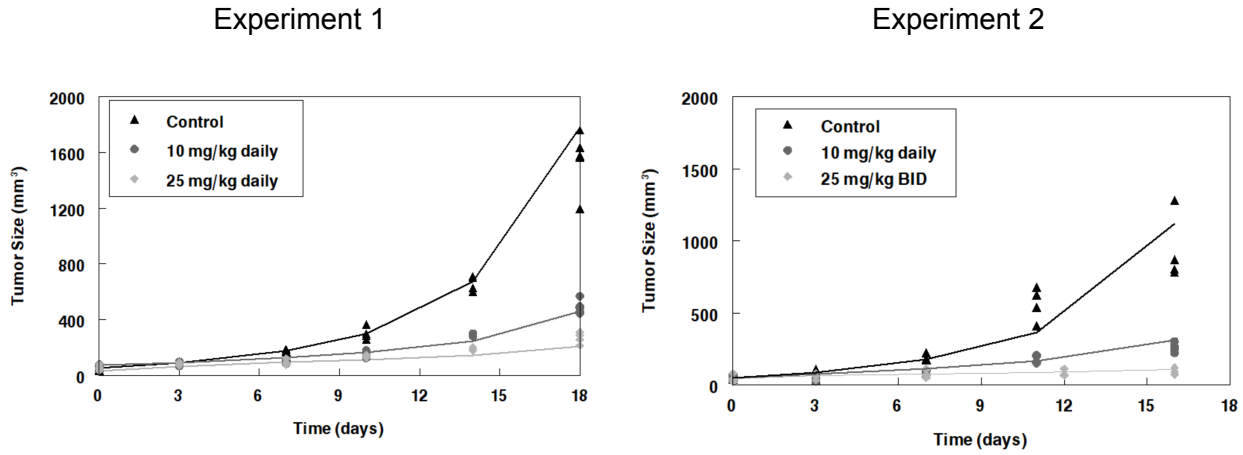

Fig. 2.5. Growth inhibition experiments. A. Scheme of treatment study of dT+DI-87, DI87 was administered as multiple doses in combination with thymidine to mice. Experiment compared 10 mg/kg daily to 25 mg/kg daily dosing of DI-87. B. Representative tumors after 1 week of treatment with agents as indicated. C. Quantification of tumor volume after 1 week of treatment with agents as indicated. Data represent the mean and standard deviation of 5 mice. D. Growth inhibition model simulations. Solid lines represent simulations from final PK-PD model and symbols represent data from: Experiments 1 and 2. Overall the model represents data well.

REFERENCES

1. Reichard P. Interactions between deoxyribonucleotide and DNA synthesis. Annu Rev Biochem 1988;**57**:349-74.

2. Chao J, Synold TW, Morgan RJ, Jr., Kunos C, Longmate J, Lenz HJ, et al. A phase I and pharmacokinetic study of oral 3-aminopyridine-2-carboxaldehyde thiosemicarbazone (3-AP, NSC #663249) in the treatment of advanced-stage solid cancers: a California Cancer Consortium Study. Cancer Chemother Pharmacol 2012;**69**:835-43.

3. Nathanson DA, Armijo AL, Tom M, Li Z, Dimitrova E, Austin WR, et al. Co-targeting of convergent nucleotide biosynthetic pathways for leukemia eradication. J Exp Med 2014;**211**:473-86.

4. Kim W, Le TM, Wei L, Poddar S, Bazzy J, Wang X, et al. [18F]CFA as a clinically translatable probe for PET imaging of deoxycytidine kinase activity. Proc Natl Acad Sci U S A 2016;**113**:4027-32.

5. Le TM, Poddar S, Capri JR, Abt ER, Kim W, Wei L, et al. ATR inhibition facilitates targeting of leukemia dependence on convergent nucleotide biosynthetic pathways. Nat Commun 2017;**8**:241.

6. Radu CG, Shu CJ, Nair-Gill E, Shelly SM, Barrio JR, Satyamurthy N, et al. Molecular imaging of lymphoid organs and immune activation by positron emission tomography with a new [18F]-labeled 2'-deoxycytidine analog. Nat Med 2008;**14**:783-8.

7. Shu CJ, Campbell DO, Lee JT, Tran AQ, Wengrod JC, Witte ON, et al. Novel PET probes specific for deoxycytidine kinase. J Nucl Med 2010;**51**:1092-8.

8. Upton RN, Mould DR. Basic concepts in population modeling, simulation, and model-based drug development: part 3-introduction to pharmacodynamic modeling methods. CPT Pharmacometrics Syst Pharmacol 2014;**3**:e88.

9. Gobburu JV, Jusko WJ. Role of dosage regimen in controlling indirect pharmacodynamic responses. Adv Drug Deliv Rev 2001;**46**:45-57.

10. Cerami E, Gao J, Dogrusoz U, Gross BE, Sumer SO, Aksoy BA, et al. The cBio cancer genomics portal: an open platform for exploring multidimensional cancer genomics data. Cancer Discov 2012;**2**:401-4.

11. Spasokoukotskaja T, Arner ES, Brosjo O, Gunven P, Juliusson G, Liliemark J, et al. Expression of deoxycytidine kinase and phosphorylation of 2-chlorodeoxyadenosine in human normal and tumour cells and tissues. Eur J Cancer 1995;**31A**:202-8.

12. Lee JT, Campbell DO, Satyamurthy N, Czernin J, Radu CG. Stratification of nucleoside analog chemotherapy using 1-(2'-deoxy-2'-18F-fluoro-beta-D-arabinofuranosyl)cytosine and 1-(2'-deoxy-2'-18F-fluoro-beta-L-arabinofuranosyl)-5-methylcytosine PET. J Nucl Med 2012;**53**:275-80.

13. Guidance for Industry Estimating the Maximum Safe Starting Dose in Initial Clinical Trials for Therapeutics in Adult Healthy Volunteers. U.S. Department of Health and Human Services Food and Drug Administration Center for Drug Evaluation and Research (CDER). http://www.fda.gov/downloads/Drugs/.../Guidances/UCM078932.pdf, 2005

14. Le Tourneau C, Stathis A, Vidal L, Moore MJ, Siu LL. Choice of starting dose for molecularly targeted agents evaluated in first-in-human phase I cancer clinical trials. J Clin Oncol 2010;**28**:1401-7.

15. Sachs JR, Mayawala K, Gadamsetty S, Kang SP, de Alwis DP. Optimal Dosing for Targeted Therapies in Oncology: Drug Development Cases Leading by Example. Clin Cancer Res 2016;**22**:1318-24.

16. Paller CJ, Bradbury PA, Ivy SP, Seymour L, LoRusso PM, Baker L, et al. Design of phase I combination trials: recommendations of the Clinical Trial Design Task Force of the NCI Investigational Drug Steering Committee. Clin Cancer Res 2014;**20**:4210-7.

17. Matthews PM, Rabiner EA, Passchier J, Gunn RN. Positron emission tomography molecular imaging for drug development. Br J Clin Pharmacol 2012;**73**:175-86.

18. Murphy JM, Armijo AL, Nomme J, Lee CH, Smith QA, Li Z, et al. Development of new deoxycytidine kinase inhibitors and noninvasive in vivo evaluation using positron emission tomography. J Med Chem 2013;**56**:6696-708.

19. 18F-Clofarabine PET/CT in Imaging Cancer Patients Before and After Interventions. https://clinicaltrials.gov/ct2/show/NCT02888301. Accessed October 8, 2018.

CHAPTER 3

Evaluation of potent isoquinoline-based thiosemicarbazone antiproliferatives against solid tumor models

ABSTRACT

A potent class of isoquinoline-based α-N-heterocyclic carboxaldehyde thiosemicarbazone (HCT) compounds has been re-discovered; based on this scaffold we have synthesized three series of antiproliferative agents through iterative rounds of methylation and fluorination modifications. Synergy between isoquinoline fluorination and 4' amine methylation was identified, and incubation of the compounds with physiologically relevant levels of $CuCl_2$ was shown to further potentiate their activity. The lead compound, **HCT-13**, was highly potent against a panel of pancreatic, small cell lung carcinoma, and prostate cancer models, with IC_{90} values in the low-to-mid nanomolar range. We show that the cytotoxicity of **HCT-13** is copper-dependent, that it acts as a copper ionophore, induces production of reactive oxygen species (ROS), and promotes mitochondrial dysfunction and S-phase arrest. Lastly, DNA damage response/ replication stress response (DDR/RSR) pathways, specifically Ataxia-Telangiectasia Mutated (ATM) and Rad3-related protein kinase (ATR), were identified as actionable adaptive resistance mechanisms following **HCT-13** treatment. Taken together, **HCT-13** is potent against solid tumor models and warrants *in vivo* evaluation against aggressive tumor models, either as a single agent or as part of a combination therapy.

INTRODUCTION

The diverse therapeutic potential of α-N-heterocyclic carboxaldehyde thiosemicarbazones (HCTs) have been investigated since the 1940s, with tuberculostatic activity being first observed *in vivo* as early as 1946.[1] This class of compounds was subsequently shown to possess antitumor, antiviral, antibacterial, and antifungal activities, prompting decades of research and development.[2–7] In particular, isoquinoline-based HCTs such as IQ-1 (**HCT-1**)[3] were the subject of early interest due to their efficacy, particularly in terms of 50-day survival rates of tumor-bearing mice (**Figure 1**).[5] The research groups of Sartorelli and French spent decades developing isoquinoline HCTs and investigating other HCT scaffolds, eventually turning their attention to pyridyl-based HCT analogs. Notably, in 1992 Sartorelli and coworkers developed 3-aminopyridine-2-carboxaldehyde thiosemicarbazone (3-AP, also known as Triapine), a pyridyl-based HCT. It has since undergone multiple clinical trials for the treatment of various cancers, and it is widely accepted to inhibit ribonucleotide reductase (RNR), a critical enzyme for rapidly proliferating cells such as bacteria and cancer cells.[8–14] Two other HCT compounds, namely di-2-pyridylketone 4-cyclohexyl-4-methyl-3-thiosemicarbazone (DpC) hydrochloride and 4-(2-pyridinyl)-2-(6,7-dihydro-8(5*H*)-quinolinylidene)hydrazide-1-piperazinecarbothioic acid (COTI-2)[15,16], have been investigated in the clinic. However, despite the early promise, no HCT compounds have yet advanced beyond phase II clinical trials.[13]

While the mechanisms of action of HCTs are multi-modal and have not yet been fully defined[17–25], their biological activities generally stem from the ability to chelate transition metals through their heterocyclic nitrogen, Schiff base nitrogen, and thiosemicarbazone sulfur. The resulting HCT-metal complexes can undergo redox cycles, a property that generates cytotoxic reactive oxygen species (ROS) through Fenton and/or Haber-Weiss processes.[26] HCTs are particularly adept at binding copper[27], which can be either detrimental or beneficial to the compound's biological activity. For instance, physiological concentrations of copper in human plasma (11-18 μM)[28,29] strongly interfere with the RNR-inhibitory activity of 3-AP[27], while the cytotoxicities of Dp44mT[30,31] and NSC-319726[32] against glioblastoma and other cancer models are potentiated by copper. Binding of this transition metal is intriguing from an anticancer therapy standpoint, as cancers rely upon higher intracellular levels of copper, relative to healthy cells, to promote angiogenesis, tumor growth, and metastasis.[33,34] Indeed, several therapeutic strategies have employed small molecules to disrupt copper homeostasis in cancers, either through chelation-mediated copper sequestration, or by increasing intracellular copper to cytotoxic levels through ionophoric modalities.[32,35]

The antiproliferative effects of HCTs coupled with their ability to bind copper make them a compelling scaffold from which to develop copper-mediated therapeutics. We have identified isoquinoline-based HCTs as a viable scaffold for this purpose, as previously reported analogs demonstrated both *in vitro* and *in vivo* efficacy. Additionally, studies investigating the isoquinoline HCT chemical space have not emerged for years, as focus shifted away from this scaffold following the report of 3-AP.[3,5,6] Therefore, we aimed to develop novel isoquinoline-based HCTs which leverage copper against malignancies. Herein, the design and synthesis of such a series of molecules is reported, with identification of a lead compound (**HCT-13**) which inhibits proliferation of pancreatic ductal adenocarcinoma (PDAC), small cell lung carcinoma (SCLC), and prostate cancer (PC) models at nanomolar concentrations in the presence of physiologically relevant levels of copper. We further demonstrate that **HCT-13** increases intracellular copper levels, generates reactive oxygen species (ROS), and interferes with the mitochondrial electron transport chain. Additionally, we have identified actionable adaptive resistance mechanisms which could be exploited in combination therapies.

METHODS AND MATERIALS

Cell culture and culture conditions

Pancreatic adenocarcinoma cell lines: PATU8988T, MIAPACA2, SU8686, PSN1, HPAC, BXPC3, DANG, SUIT2, A13A, CAPAN2, T3M4, A2.1, HUPT4, XWR200, L36PL, YAPC, PANC0327, PANC1, PATU8902, HPAF11, ASPC1, PANC0813, PANC0203, HS766T, SW1990, and CFPAC1; prostate cancer cell lines: 22Rv1, LNCaP, RM1 and C4-2; and small cell lung carcinoma cell lines: NCI-H526, NCI-H146, and NCI-H1963 were obtained from American Type Culture Collection (ATCC). 143 BTK WT and 143 BTK ρ_0, BJ WT and BJ ρ_0 cells were gifts from Prof. Michael Teitell in UCLA. Murine Prostate cancer cell lines MyC CaP was a kind gift from Prof. DLJ Thorek at WUSTL. Murine Pancreatic cancer cells KP4662 was kind gift from Prof. Robert Vonderheide at UPenn. With a few exceptions, cell lines were cultured in DMEM (Corning) or RPMI (Corning) containing 10% fetal bovine serum (FBS, Omega Scientific) and were grown at 37 °C, 20% O_2 and 5% CO_2. All cultured cells were incubated in antibiotic free media and were regularly tested for mycoplasma contamination using MycoAlert kit (Lonza) following the manufacturer's instructions, except that the reagents were diluted 1:4 from their recommended amount.

Proliferation assay

Cells were plated in 384-well plates (500 cells/well for adherent cell lines in 30 µl volume). Drugs were serially diluted to the desired concentrations and an equivalent volume of DMSO was added to vehicle control. Following 72 h incubation, ATP content was measured using CellTiter-Glo reagent according to manufacturer's instructions (Promega, CellTiter-Glo Luminescent Cell Viability Assay), and analyzed by SpectraMax luminometer (Molecular Devices). IC_{50} and IC_{90} values, concentrations required to inhibit proliferation by 50% and 90% respectively compared to DMSO treated cells, were calculated using Prism 6.0 h (Graphpad Software).

Western blot

Cells were lysed using RIPA buffer supplemented with protease (ThermoFisher, 78,430) and phosphatase (ThermoFisher, 78,420) inhibitors, scraped, sonicated, and centrifuged (20,000 × *g* at 4 °C). Protein concentrations in the supernatant were determined using the Micro BCA Protein Assay kit (Thermo), and equal amounts of protein were resolved on pre-made Bis-Tris polyacrylamide gels (Life Technologies). Primary antibodies: $pAMPK_{T172}$ (Cell signaling, #2535, 1:1000), HO-1 (Cell signaling, #5061S, 1:1000), pS345 CHEK1(Cell signaling, #2348L, 1:1000), pT68 CHEK2 (Cell signaling, #2197 S, 1:1000), pS139 H2A.X (Millipore, 05-636, 1:1000), clvd.

Casp3 (Cell signaling, #9662, 1:1000), and anti-actin (Cell Signaling Technology, 9470, 1:10,000). Primary antibodies were stored in 5% BSA (Sigma-Aldrich) and 0.1% NaN_3 in TBST solution. Anti-rabbit IgG HRP-linked (Cell Signaling Technology, 7074, 1:2500) and anti-mouse IgG HRP-linked (Cell Signaling Technology, 7076, 1:2500) were used as secondary antibodies. Chemiluminescent substrates (ThermoFisher Scientific, 34,077 and 34,095) and autoradiography film (Denville) were used for detection.

Viability/Apoptosis assay

Viable cells were measured by Trypan blue staining using vi-cell counter (Beckman Coulter, CA, USA). Apoptosis and cell death were assayed using Annexin V-FITC and PI according to manufacturer's instructions (FITC Annexin V Apoptosis Detection Kit, BD Sciences, #556570).

Cell cycle

Cell cycle was assessed using Propidium iodide staining at indicated timepoints. Cells were pulsed with EdU 1 h before collection at different time points. Cells were fixed 4% paraformaldehyde, permeabilized with perm/wash reagent (Invitrogen), stained with Azide-AF647 (using click-chemistry, Invitrogen; Click-iT EdU Flow cytometry kit, #C10634) and FxCycle-Violet (Invitrogen), and then analyzed by flow cytometry (a detailed description is available in the Supplementary Information).

ROS Measurements

Cellular ROS measurement was assayed with CM-H2DCFDA staining after treatment according to manufacturer's instructions (Reactive Oxygen Species (ROS) Detection Reagents, Invitrogen, #D399). The cells were then incubated with 5 μM of CM-H2DCFDA for 30 min, spun down at 450 x g for 4 mins, and the supernatant was replaced with fresh media containing lethal compounds and/or Cu(II). Then, the cells were incubated for 30 mins, spun down, and the supernatant was replaced with PBS. The samples were analyzed using flow cytometry.

Mitochondrial ROS was measured using MitoSOX staining according to manufacturer's instructions (MitoSOX, Invitrogen, #M36008). Cells were treated with HCT-13, washed and treated with MitoSOX. Cells were then incubated for 30 minutes at 37°C. After incubation, media is aspirated and cells are washed with PBS and analyzed by flow cytometry.

Mito Stress Test and Electron Flow Assay

All oxygen consumption rate (OCR) was measured using a XF24 Analyzer (Agilent) and normalized per µg protein. For cellular OCR, cells were incubated in unbuffered DMEM containing 25 mM glucose, 1 mM pyruvate and 2 mM glutamine. OCR was measured before (total respiration) and after the sequential injection of 1 µM oligomycin (complex V inhibitor), 0.75 µM FCCP (uncoupler), and 1 µM of rotenone and myxothiazol (complex I and III inhibitors, respectively), as described previously (1). Mitochondrial respiration was calculated by subtracting the non-mitochondrial respiration left after rotenone and myxothiazol injection. Oligomycin-sensitive respiration represents ATP-linked respiration (coupled respiration).

To measure electron transport chain complex activity from cells, cells were incubated in MAS buffer with 10 mM pyruvate (complex I substrate), 2 mM malate, 4 µM FCCP, 4 mM ADP, and 1 nM of XF Plasma Membrane Permeabilizer (PMP) reagent (Agilent). OCR was measured before and after the sequential injection of 2 µM rotenone, 10 mM succinate (complex II substrate), 4 µM antimycin A (complex III inhibitor), and a mix of 10 mM ascorbate and 100 µM TMPD (complex IV substrates), as described previously (2). Antimycin A-sensitive respiration represents the complex III respiration.

To measure OCR directly from mitochondria, mitochondria were isolated from fresh mouse liver by dual centrifugation at 800g and 8000g and seeded by centrifugation (2). Mitochondria were incubated with 1 mM pyruvate (complex I), 2 mM malate, 4 µM FCCP in MAS buffer, as well as the “corresponding drugs” for 30 min at 37ºC. OCR was measured before and after the sequential injections described in the previous paragraph.

Intracellular Cu(II) measurement

Cells were plated in 6-well plates and cultured for one day. Vehicle of HCT-13 were added to the cells the following day and incubated for 24 hours. The plates were then washed 2 times with PBS containing 1 mM EDTA and 2 times with PBS alone. The concentration of Cu(II) was measured using Inductive Coupled Plasma Mass Spectrometry (ICP-MS) using standard procedure.

DHODH activity

Recombinant protein was incubated in an aqueous solution (total volume, 1.0 mL) containing 500 µM DHO (Sigma, D1728), 200 mM K2CO3-HCl (pH 8.0), 0.2% triton x-100, and 100 µM coenzyme Q10 (Sigma, C9538) at 37 °C for 0, 15, 30, 45, or 60 min. An aliquot (100 µL) of the mixture of enzyme reaction mixture or cell/tissue lysate was mixed with 100 µL of 0, 0.5, or 1.0 µM orotic acid, 50 µL of H2O, 250 µL of 4.0 mM 4-TFMBAO (Sigma, 422231), 250 µL of 8.0 mM

K_3[Fe(CN)6] (Sigma, 244023), and 250 µL of 80 mM K_2CO_3 (Sigma, P5833) and then heated at 80 °C for 4.0 min. The reaction was stopped by cooling in an ice-water bath and the absorbance was measured with a spectrofluorometer (FP-6300 Jasco, Tokyo, Japan): excitation and emission wavelengths were 340 nm and 460 nm, respectively.

FACS analyses

All flow cytometry data were acquired on a five-laser LSRII cytometer (BD), and analyzed using the FlowJo software (Tree Star).

RESULTS

Synthesis of isoquinoline-based α-N-heterocyclic carboxaldehyde thiosemicarbazone (HCT) compounds

Among the previously reported isoquinoline HCTs, the 5-, 7-, and 8-fluoro analogs of **HCT-1** were of particular interest to our group. These compounds varied in terms of potency and toxicity[5], demonstrating that the effects of fluorination were dependent upon the position of isoquinoline substitution. The benefits that fluorination endows upon small-molecule drugs are well documented[36,37], and are also reflected in the marketplace, since approximately 20% of all pharmaceuticals are fluorinated.[38] Therefore, it was important to investigate how the previously unreported 4- and 6-fluoro analogs of **HCT-1** would perform in antiproliferative assays against cancer models. Additionally, we were intrigued as to whether fluorination at these positions would synergize with 4' amine alkylation, as Kowol et al. discovered that 4' amine alkylation potentiated the cytotoxicity of 3-AP analogs.[39]

A total of 15 isoquinoline-based HCTs – four known compounds (**HCT-1, HCT-4, HCT-5, HCT-6**) and 11 novel compounds – were synthesized and tested for antiproliferative potency against cancer models (**Scheme 1, Table 1**). The synthetic approach began with methylation of the appropriate isoquinoline **1** to generate **2** (**Scheme 1**). Depending upon the desired 5-position substituent, **2** was then subjected to either Route A (5-hydrido), Route B (5-amino), or Route C (5-methylamino). Syntheses of **HCTs 1-3**, **HCTs 6-8**, and **HCTs 11-13** were carried out by Route A, wherein the methyl substituent of **2** was oxidized using selenium dioxide (SeO_2) to furnish the carboxaldehyde **3**. Condensation with the appropriate thiosemicarbazide under acidic conditions yielded the desired HCT. **HCT-5** and **HCT-10** were synthesized *via* Route B, which began with nitration of **2** followed by an iron-mediated reduction to the amine, which was subsequently Boc-protected and oxidized to produce carboxaldehyde **4**. This intermediate was then simultaneously Boc-deprotected and condensed with the appropriate thiosemicarbazide under acidic conditions to furnish the target HCT. Syntheses of **HCT-4**, **HCT-9**, **HCT-14**, and **HCT-15** *via* Route C proceeded from **2** with installation of a nitro group, subsequent conversion to the mono-Boc-methylamine, and SeO_2-mediated oxidation to furnish **5**. Concurrent Boc-deprotection and thiosemicarbazide condensation were again achieved under acidic conditions to provide the desired HCT compound. While characterizing the HCTs, we occasionally observed the presence of a minor *Z*-isomeric product, particularly for **HCTs 11-15**. This isomer arose from an intramolecular hydrogen bond between the 2' amine of the thiosemicarbazone and the heterocyclic isoquinoline nitrogen, forming a stable 6-membered hydrogen bonded species.[40] The E and Z isomers were inseparable by reversed-phase HPLC purification and

were used as a mixture *in vitro*, as previous studies reported no significant difference in potency.[40]

Fluorination and dimethylation display synergistic effects further potentiated by copper supplementation

IC_{90} values against MIAPACA2 cells for all compounds were first determined in normal cell culture conditions (DMEM media and 10% FBS) (**Figure 2**). Compounds were separated into three series – 4' primary amines, 4' secondary amines, and 4' tertiary amines – to reflect the relative degrees of 4' amine methylation. A series of non-methylated 4' primary amine compounds was first synthesized, with known compounds **HCT-1**, **HCT-4**, and **HCT-5** included to gauge whether fluorination of the isoquinoline proved beneficial for biological activity.[41,42] Within the 4' primary amine series, fluorination at the isoquinoline 4-position (**HCT-2)** did not show an increase in potency relative to unsubstituted analog **HCT-1**. However, fluorination at the 6-position (**HCT-3)** showed a 3-fold increase in potency, demonstrating that the fluorine position impacts the potency of these compounds.

In the 4' secondary amine series, synergistic effect was observed when combining isoquinoline fluorination with 4' amine methylation. The 4-fluorine substituted **HCT-7** and the 6-fluorine substituted **HCT-8** were each significantly more potent than their non-fluorinated analog **HCT-6**, as well more potent than their 4' primary amine analogs (**HCT-2** and **HCT-3**, respectively). The trend of isoquinoline substitution and 4' secondary amine combining to enhance potency held for 5-methylamino substituted **HCT-9** and 5-amino substituted **HCT-10**. Taken together, these results suggested that combining isoquinoline substitution, particularly 4- or 6-fluorination, with 4' amine methylation produced synergistic antiproliferative effects when compared with either modification alone.

The effects of fluorine substitution became significantly more pronounced for the di-methylated 4'-tertiary amine compounds **HCT-12** and **HCT-13**, whose IC_{90} values were in the nM range and were roughly 110- and 270-fold more potent, respectively, when compared to their non-fluorinated analog **HCT-11**. Fluorination at the 6-position (**HCT-13**) was found to be a superior modification when compared to fluorination at the 4-position (**HCT-12**), a trend which also held for the fluorine-substituted 5-methylamino compounds **HCT-14** and **HCT-15**.

HCT compounds are known to be copper chelators, and a recent publication by Stockwell and coworkers demonstrated that the activity of a known 4' tertiary amine HCT (NSC-319726) was significantly potentiated by the addition of copper.[32] To test whether our compounds were similarly potentiated, IC_{90} (+Cu IC_{90}) values were determined against MIAPACA2 cells in media supplemented with physiologically relevant levels of copper (DMEM media + 10% FBS + 20 μM

$CuCl_2$) (**Fig. 2)**. While the activity of **HCT-5** was attenuated, all other compounds displayed a significant increase in potency under copper-supplemented conditions. For non-fluorinated isoquinoline compounds **HCT-1**, **HCT-6**, and **HCT-11**, the +Cu IC_{90} values improved as the degree of methylation at the 4' amine increased (10-fold, 60-fold, and 400-fold increase in potency, respectively, versus non-copper-supplemented IC_{90} values). Copper supplementation was similarly beneficial for fluorinated isoquinolines – all such compounds displayed significant improvements in antiproliferative potency in presence of copper, and fluorine substitution led to greater potency when compared with corresponding non-fluorinated analogs. Compounds bearing 4' tertiary amines were the most active, achieving +Cu IC_{90} values as low as 21.6 nM (**HCT-13**). The results demonstrated that physiologically relevant levels of copper potentiated the activity of isoquinoline HCTs, and that 4' amine methylation synergized with fluorine substitution. Due to its potency and straightforward synthesis, we chose **HCT-13** as a lead compound for in-depth mechanism of action studies.

HCT-13 highly potent against a panel of solid tumor models and induces copper-dependent cytotoxicity

Serum copper levels are elevated (>20 μM) in individuals with solid tumor types such as pancreatic ductal adenocarcinoma (PDAC), small cell lung carcinoma (SCLC), and prostate cancer (PC).[43–48] These cancers rely upon elevated copper levels to sustain growth, making this transition metal a viable target for therapeutic modulation.[34] In a panel of PDAC, SCLC, and PC cancer models cultured in media supplemented with physiologically relevant levels of copper (20 μM $CuCl_2$), **HCT-13** was a highly potent growth inhibitor, with +Cu IC_{90} values ranging from 1 nM to 200 nM (**Figure 3a**). The MIAPACA2 cell line, a well-characterized PDAC model that was highly sensitive to **HCT-13** treatment, was used to further investigate the mechanism of action of the lead compound.

MIAPACA2 proliferation was measured in response to **HCT-13** in the presence and absence of 20 μM $CuCl_2$ (Cu(II)), as well as in response to 20 μM Cu(II) alone (**Figure 3b**). The potency of **HCT-13** improved by greater than 5-fold under Cu(II) supplemented conditions, with its IC_{90} decreasing from 110 nM to 21 nM. Importantly, Cu(II) supplementation alone did not affect proliferation at all. To probe whether **HCT-13** was acting as an ionophore, intracellular copper levels were measured using inductively coupled plasma mass spectrometry (ICP-MS). In the presence of **HCT-13**, intracellular copper levels increased both with and without Cu(II) supplementation (**Figure 3c**). Additionally, treatment with bathocuproine disulfonate (BCPS), a membrane impermeable Cu(II) chelator, abrogated the cytotoxicity of **HCT-13** in the presence of Cu(II), suggesting that the growth inhibitory effect of our lead compound is largely dependent upon the availability of copper (**Figure 3d**). Collectively, this data suggests that **HCT-13** is a

Cu(II) ionophore which increases intracellular copper concentration, and whose cytotoxicity is copper-dependent.

HCT-13 induces oxidative stress and ROS production

While **HCT-13** in the presence of Cu(II) exhibited nanomolar potency against a panel of solid cancer models, the underlying reasons remained unknown as the canonical mechanism of HCT cytotoxicity is poorly defined in the literature. Cu(II)-supplemented MIAPACA2 cells treated with **HCT-13** showed induction of AMPK phosphorylation (T172) at 24 h, demonstrating suppression of mitochondrial oxidative phosphorylation (**Figure 4a**). Further, **HCT-13** treatment increased heme oxygenase-1 (HO-1) levels in MIAPACA2 cells, indicative of ROS induction (**Figure 4a**). Based on the immunoblot results, we set out to determine whether **HCT-13** treatment was leading to ROS generation. We found that treatment with our lead compound induced ROS generation detectable by CM-H_2DCFDA staining (**Figure 4b**). Interestingly, ROS generation resulting from **HCT-13** treatment of MIAPACA2 cells was also observed in the mitochondria, as measured by mitochondria-specific dye MitoSOX (**Figure 4c**).

HCT-13 induces mitochondrial dysfunction and displays mitochondria-dependent cytotoxicity

Considering the canonical role AMPK plays in energy homeostasis, and the implication that AMPK activation may signal mitochondrial dysfunction[49], we compared the metabolic status of MIAPACA2 cells treated with **HCT-13** for 24 hr with and without 20 μM Cu(II) using a Seahorse Bioscience XFe24 analyzer. In the presence of Cu(II), **HCT-13** significantly reduced both the basal respiration and maximum respiratory capacities of MIAPACA2 cells, indicating mitochondrial electron transport chain (mtETC) impairment (**Figure 5a**). *In vitro* mitochondrial complex activity following **HCT-13** treatment was dissected by an electron flow assay in isolated mitochondria, which showed decreased activity of complexes I and II (**Figure 5b**).

These findings suggested that **HCT-13** inhibited mtETC activity but did not indicate whether the lead compound's cytotoxicity stemmed from effects independent of mitochondrial function. Another HCT compound, Dp44mT, was reported to increase AMPK expression and induce ROS, although its cytotoxicity was not attributed to the functionality of the mitochondria.[50] To determine whether the cytotoxicity of **HCT-13** was mitochondria-dependent, its effects upon 143 BTK ρ_0, an mtDNA-deficient fibroblast cell line, were examined. Both 143 BTK ρ_0 and parental (wild type, WT) cells were treated with **HCT-13** + 20 μM Cu(II) for 48 h, after which cell viability was determined through trypan blue staining (**Figure 5c**). Compared to WT, the ρ_0 cells were significantly less sensitive to the treatment. The cytotoxicity of **HCT-13** was partially abolished

by supplementation with uridine (rU) but not by pyruvate, suggesting disruption to the supply of pyrimidine nucleotides in addition to impaired mitochondria (**Supplementary Figure S2a**). Proper mitochondrial function is necessary for the action of dihydroorotate dehydrogenase, an enzyme critical for the *de novo* production of pyrimidine nucleotides, and one for which **HCT-13** did not demonstrate affinity (**Supplementary Figure S2b**). Additionally, cell cycle analysis revealed marked S-phase arrest in 143 BTK WT cells but not in 143 BTK ρ_0 (**Figure 5d**). Taken together, these results indicate that the cytotoxic effects of **HCT-13** are mitochondria-dependent and suggest that **HCT-13** may be indirectly targeting DHODH, and thus *de novo* pyrimidine nucleotide production, through induction of mitochondrial dysfunction.

Small molecule kinase inhibitor screen with HCT-13 identifies the DNA-damage pathway as a resistance mechanism

To identify potential resistance mechanisms and synergistic interactions with **HCT-13**, we performed an unbiased pharmacological inhibition screen using a chemical genomics platform consisting of 430 kinase inhibitors (Selleckchem, Cat. L1200). MIAPACA2 cells were treated with the 430-member library, covering a 7-point concentration range spanning between 6.5 nM and 5 μM, with and without 25 nM **HCT-13** in presence of 20 μM $CuCl_2$. After 72 h of incubation, ATP content was measured using CellTiter-Glo (**Figure 6a**). A composite synergy score was calculated for each combination, defined as the sum of the Bliss Additivity Score (% proliferation inhibition observed - % proliferation inhibition expected). A positive synergy score indicates greater-than-additive interaction, and a negative score indicates less-than-additive interaction i.e. antagonism.

The ten highest scoring compounds were kinase inhibitors contained in the DNA damage response/replication stress response (DDR/RSR) module, with the ATM/ATR/CHK pathway featuring as the most prominent codependency (**Figure 6b, 6c**). All six ATM, ATR and CHEK1 inhibitors included in the library scored positively in the screen, indicating synergy with our lead compound. Upon **HCT-13** + Cu(II) treatment, we consistently observed phosphorylation of the downstream targets of ATR and ATM, CHEK1 and CHEK2, respectively, indicating activation of this pathway as an adaptive resistance mechanism. This phosphorylation was accompanied by induction of DNA damage marker pH2AX and by cleavage of apoptotic marker caspase 3 (**Figure 6d**). The synergistic interaction between **HCT-13** and ATR inhibition was further validated using cell death assays measured by Annexin V/PI and Trypan Blue Viability Staining in PDAC (MIAPACA2, CFPAC-1) and PC (C4-2) cell lines (**Figure 6E, 6F, and Supplementary Figure S3b, S3c**).

DISCUSSION

We primarily focused on two modifications of the **HCT-1** (IQ-1) scaffold during our synthetic planning: fluorination of the isoquinoline ring, and sequential methylation of the 4' amine. Though the 5-, 7-, and 8-fluoro-substituted analogs of **HCT-1** were previously reported, and while it was apparent that fluorine position could influence a compound's toxicity and produce differential antiproliferative effects upon various cell lines, no trends had previously emerged regarding the effects of fluorine position.[5] Additionally, multiple groups have shown that 4' amine methylation potentiates the activity HCTs such as pyridine 2-carboxyaldehyde thiosemicarbazones and 2-acetylpyridine thiosemicarbazones.[24,39,40] We therefore sought to synthesize the novel 4- and 6-fluoro analogs of **HCT-1** and investigate what effects sequential 4' amine methylation had upon antiproliferative activity. Following our isoquinoline HCT synthetic campaign, analysis of the antiproliferative data revealed several trends. Without copper supplementation, fluorination at either the 4- or 6-position of the isoquinoline ring led to an increase in potency for five out of six compounds, when compared with their corresponding non-fluorinated analogs (**Figure 2**). In some cases, the change was dramatic – for example, the IC_{90} of **HCT-13** was nearly 270-fold lower than its non-fluorinated analog **HCT-11**. Secondly, 4' amine methylation in the absence of isoquinoline substitution or copper supplementation was detrimental to activity, as demonstrated by the decrease in potencies for **HCT**s **6** and **11** when compared with 4' primary amine **HCT-1** (**Figure 2**). However, combining 4' amine methylation and isoquinoline substitution in a single compound, as in **HCT**s **7-10**, **12** and **13**, produced synergistic antiproliferative effects when compared with either their 4' primary amine or unsubstituted isoquinoline analogs. **HCT-13** again exemplified this trend, with potency nearly 270-fold greater than its non-substituted isoquinoline analog **HCT-11** and nearly 50-fold greater than its non-methylated analog **HCT-3** (**Figure 2**). The underlying mechanisms responsible for this synergy remain under study by our group. Finally, the antiproliferative activities of all but one of our isoquinoline HCTs were potentiated by supplementation with physiologically relevant levels of copper, with **HCT-5** being the exception.

The observed trends culminated with identification of our lead compound as **HCT-13**, which was uncomplicated in its synthesis and potent both in the absence and presence of copper supplementation.

The potency of **HCT-13** is highlighted by its nanomolar IC_{90} values against a panel of PDAC, SCLC, and PC cancer models in the presence of physiologically relevant levels of copper (**Figure 3a**). The use of copper-chelating small molecules in anticancer therapy is an established strategy which is executed either through sequestration of copper from tumor tissue, or through increasing intracellular copper to cytotoxic levels.[51] **HCT-13** behaved as an ionophore and increased intracellular levels of copper, both in the presence and absence of copper

supplementation. This property is essential for the cytotoxicity of **HCT-13**, as sequestration of copper via BCPS-chelation negated our lead compound's growth inhibitory effects (**Figure 3d**). We further demonstrated that **HCT-13** leverages copper to effect its cytotoxicity in a mitochondria-dependent manner. Specifically, the data indicate that **HCT-13** induces mitochondrial dysfunction and mitochondria-dependent S-phase arrest, and generates ROS and oxidative stress in different cancer models. Strikingly, mitochondria-deficient 143 BTK ρ_0 cells were significantly less sensitive to **HCT-13** in the presence of copper compared to their parental 143 BTK WT counterpart, providing further evidence of mitochondria-dependent cytotoxicity (**Fig 5c**). It is possible that the observed S-phase arrest results from disruption of the *de novo* pathway (DNP) for pyrimidine nucleotide biosynthesis, which supplies cells with the pyrimidine nucleotides necessary for replication. The lone oxidation step of the pyrimidine DNP is carried out by dihydroorotate dehydrogenase (DHODH), an enzyme located in the inner mitochondrial membrane, which utilizes ubiquinone as a redox partner. Without a properly functioning mitochondrial ETC, DHODH does not have access to the levels of ubiquinone necessary for the oxidative enzyme to adequately turn-over, leading to shortages in pyrimidine nucleotides and corresponding S-phase arrest.[52–57]

In general, cancer cells exhibit higher levels of ROS and higher baseline oxidative stress than healthy cells, which may imbue our lead compound with selectivity towards them. The ROS and mitochondrial dysfunction produced in MIAPACA2 cells by **HCT-13** lead to an increase in DNA damage marker pH2AX, which may explain why our compound synergized with inhibitors of ATR (Ataxia-Telangiectasia Mutated (ATM) and Rad3-related protein kinase), the most upstream kinase in the DNA-damage response/replication stress response (DDR/RSR) pathway. Synergy with DDR/RSR inhibitors may increase the therapeutic window of our lead compound, should it be administered in combination therapy. The observed mechanisms of action of **HCT-13** suggest that it may also synergize with radiotherapy, as therapeutic ionizing radiation increases ROS, thereby increasing oxidative stress and DNA damage in the targeted area(s). Therefore, **HCT-13** could also function as a radiosensitizer by further increasing the load of ROS, oxidative stress, and DNA damage when administered in combination with radiation therapy. Taken together, the potency of **HCT-13** as a single-agent therapeutic against aggressive solid tumor models, its mechanism of action, and the observed synergy with ATR inhibitors warrant further testing *in vivo.*

CONCLUSION

A class of isoquinoline-based HCTs has been expanded upon to produce a set of novel antiproliferative compounds. The synergistic effects of combining 4' amine methylation with isoquinoline substitution were demonstrated, and **HCT-13** was identified as a highly potent antiproliferative which is active against a panel of PDAC, SCLC, and PC cancer models. The presence of physiologically-relevant levels of Cu(II) greatly potentiated our lead compound's activity, and subsequent investigation into **HCT-13**'s mechanism of action revealed that it acts as a copper ionophore and requires copper to effect its cytotoxicity. Furthermore, **HCT-13** induces ROS production, oxidative stress, S-phase arrest, and mitochondrial dysfunction which may contribute to indirect inhibition of DHODH. Lastly, a high-throughput phenotypic screen of protein kinase inhibitors was used to identify actionable adaptive resistance mechanisms of **HCT-13**-treated cells, and the DDR/RSR pathways were revealed as actionable vulnerabilities. Specifically, we show that ATR inhibition synergizes with **HCT-13** in presence of physiologically-relevant levels of Cu(II). Taken together, this study demonstrates the potential of **HCT-13** for use in anti-cancer therapy, either as a single agent or as part of a larger combination therapy.

FIGURES, SCHEMES AND TABLES

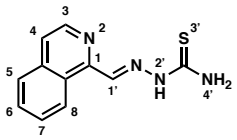

IQ-1(HCT-1)

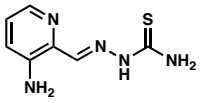

Triapine (3-AP)

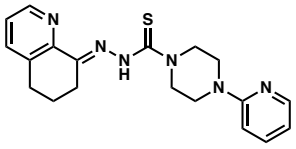

COTI-2

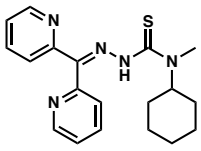

DpC

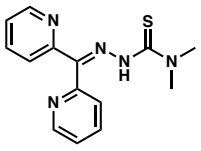

Dp44mT

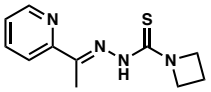

NSC319726

Fig. 3.1. Structures of α-N-heterocyclic carboxaldehyde thiosemicarbazone (HCT) compounds of clinical and research significance.

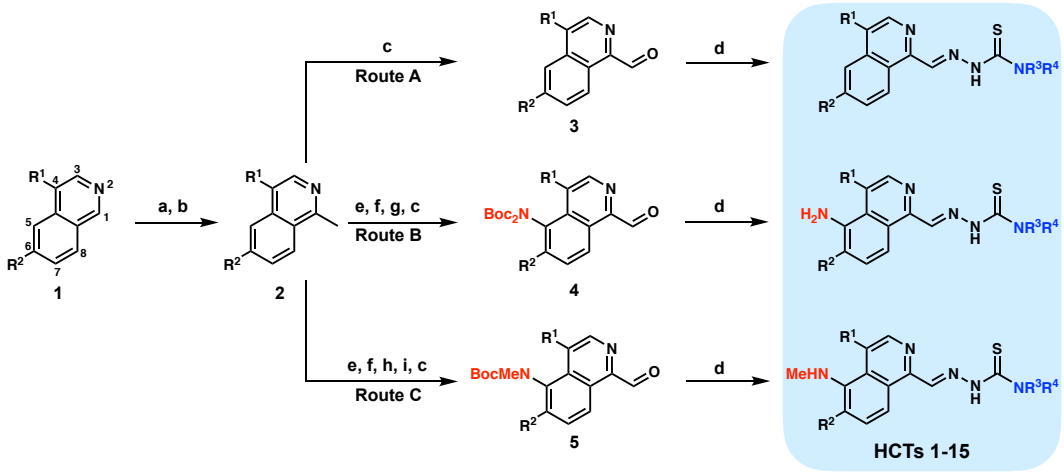

Scheme 3.1. Synthesis HCT compounds 1-15 from simple isoquinolines[a,b]

[a](a) allyl chloroformate, MeMgBr, THF; (b) $Pd(PPh_3)_4$, morpholine; DDQ, CH_2Cl_2; (c) SeO_2, 1,4-dioxane, 60 °C; (d) appropriate thiosemicarbazide, HCl, EtOH, reflux or microwave 50 °C; (e) KNO_3, H_2SO_4; (f) Fe, HCl, MeOH, reflux; (g) Boc_2O, DMAP, TEA, THF; (h) Boc_2O, DMAP, TEA, THF; $NaHCO_3$, MeOH, reflux or K_2CO_3, MeOH, reflux; (i) NaH, THF; MeI. [b]HCTs 1-3, 6-8, and 11-13 synthesized through Route A; HCTs 5 and 10 synthesized through Route B; HCTs 4, 9, 14, and 15 synthesized through Route C. See Supporting Information for full synthetic details.

Table 3.1. Substitution patterns of HCTs 1-15[a]

	HCT-1	HCT-2	HCT-3	HCT-4	HCT-5	HCT-6	HCT-7	HCT-8	HCT-9	HCT-10	HCT-11	HCT-12	HCT-13	HCT-14	HCT-15
R^1	H	F	H	H	H	H	F	H	H	H	H	F	H	H	F
R^2	H	H	F	H	H	H	H	F	H	H	H	H	F	F	H
R^3	H	H	H	H	H	Me	Me	Me	Me	Me	Me	Me	Me	Me	Me
R^4	H	H	H	H	H	H	H	H	H	H	Me	Me	Me	Me	Me
5-Pos	H	H	H	NHMe	NH_2	H	H	H	NH_2	NHMe	H	H	H	NHMe	NHMe

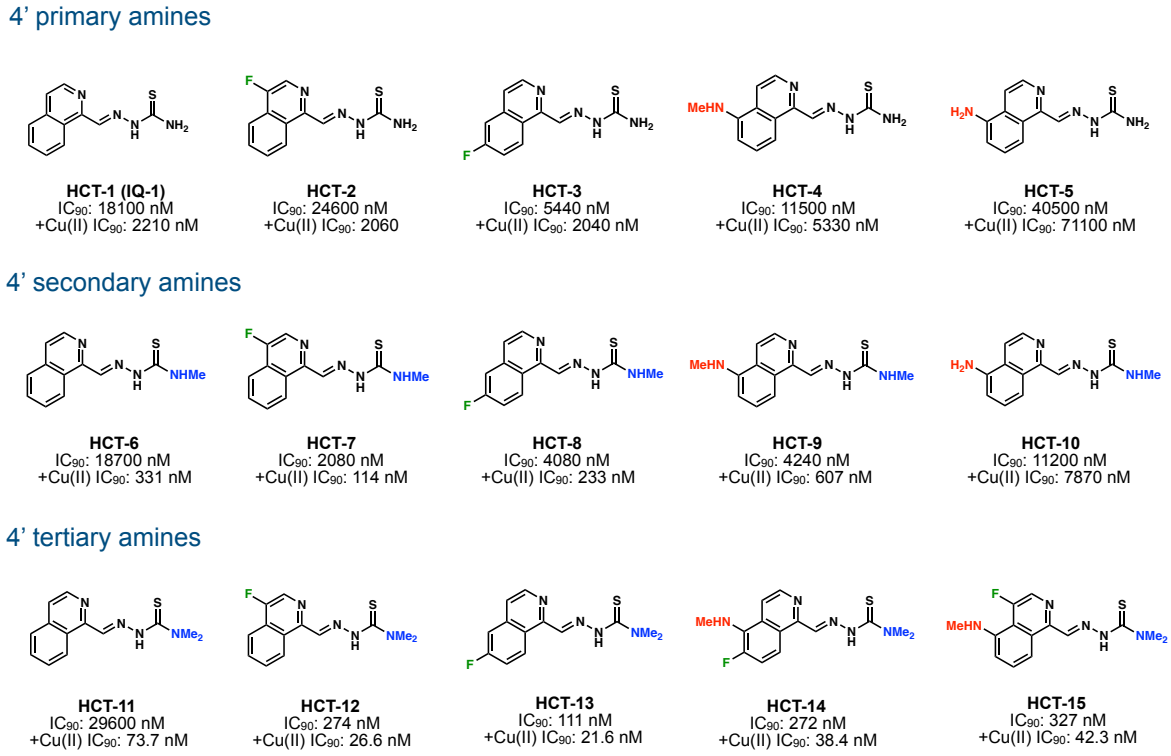

Fig. 3.2. Cu(II) supplementation potentiates the activity of isoquinoline HCTs. MIAPACA2 cells were treated with the indicated HCT ± 20 μM Cu(II) for 72 h, then cell viability was measured with CellTiter-Glo to determine IC_{90} values.

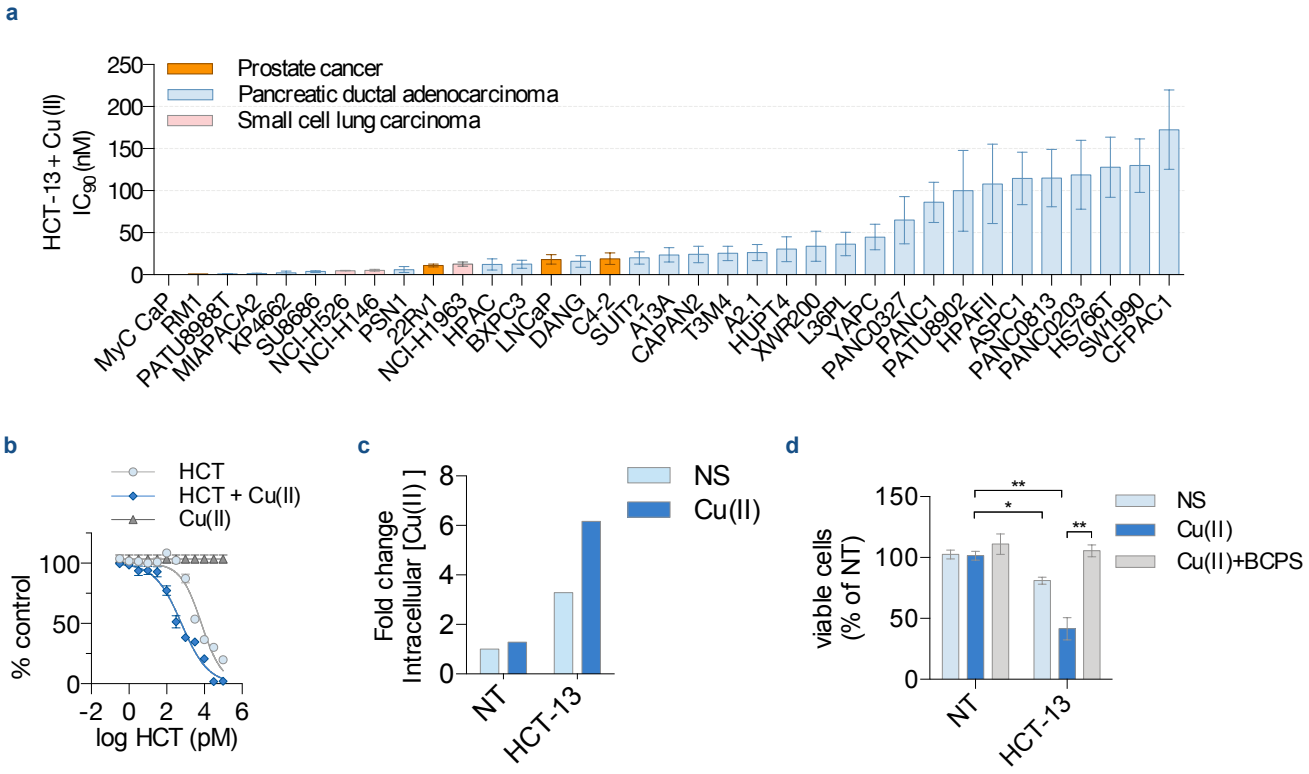

Fig. 3.3. Copper potentiates HCT-13 toxicity against a panel of cancer models. (**a**) IC_{90} in a panel of human and mouse prostate cancer (PC), small cell lung carcinoma (SCLC) and pancreatic ductal adenocarcinoma (PDAC) models treated with HCT-13 + Cu(II) (20 µM) for 72h measured by CellTiterGlo. (**b**) Proliferation rate of MIAPACA2 PDAC cells measured by CellTiterGlo following HCT-13 treatment for 72h ± Cu(II) (20 µM), and with Cu(II) alone. (**c**) Intracellular concentrations of copper measured by inductively coupled plasma mass spectrometry (ICP-MS) in MIAPACA2 PDAC cells treated with HCT-13 (25nM) for 24h ± Cu(II) (20 µM). (**d**) Inhibition of proliferation of MIAPACA2 cells treated with HCT-13 (25nM) + Cu(II) (20 µM) for 24h ± bathocuproine disulfonate (BCPS, 300 µM) measured by trypan blue exclusion.

(mean ± SD, n = 2, one-way ANOVA corrected for multiple comparisons by Bonferroni adjustment, * $P < 0.05$; ** $P < 0.01$; *** $P < 0.001$).

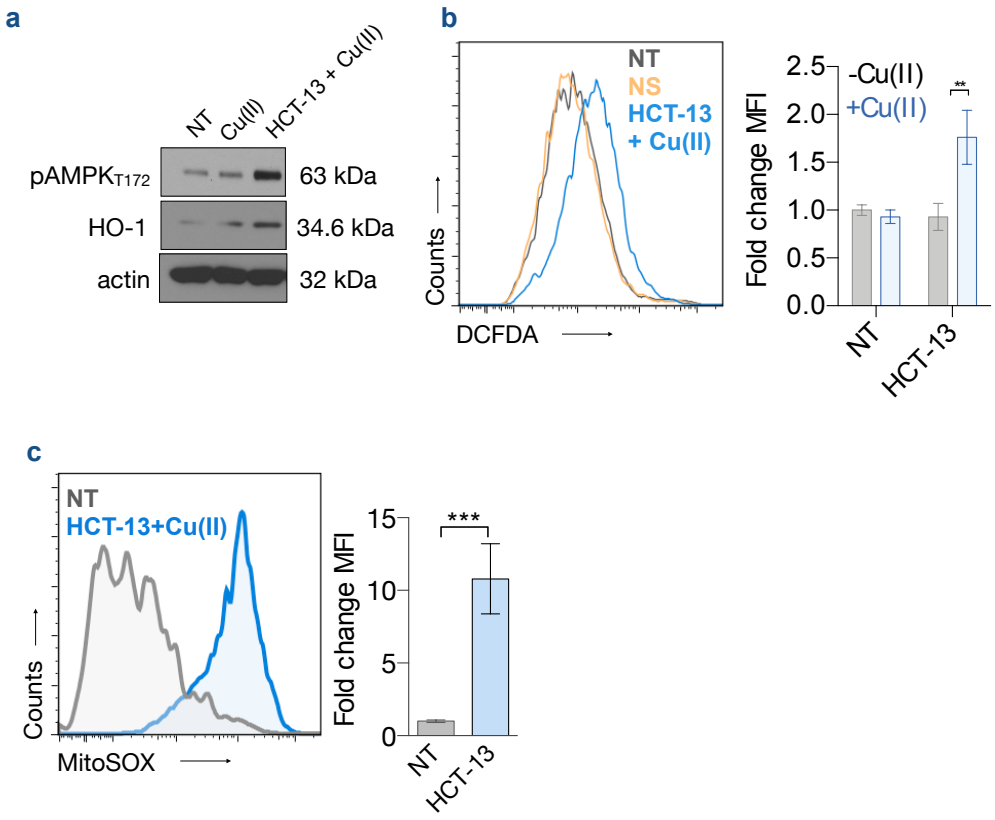

Fig. 3.4. Induction of ROS by HCT-13. (**a**) Representative immunoblots of MIAPACA2 PDAC cells treated as indicated for 24h. (**b**) Reactive oxygen species (ROS) measurement using CM-H2DCFDA staining after HCT-13 (25nM) + Cu(II) (20 μM) treatment for 24h. (**c**) Mitochondrial ROS detection using MitoSOX staining in MIAPACA2 PDAC cells treated with HCT-13 (25 nM) + Cu(II) (20 μM) for 24h.

(mean ± SD, n = 2, Student t-test, ***P < 0.001).

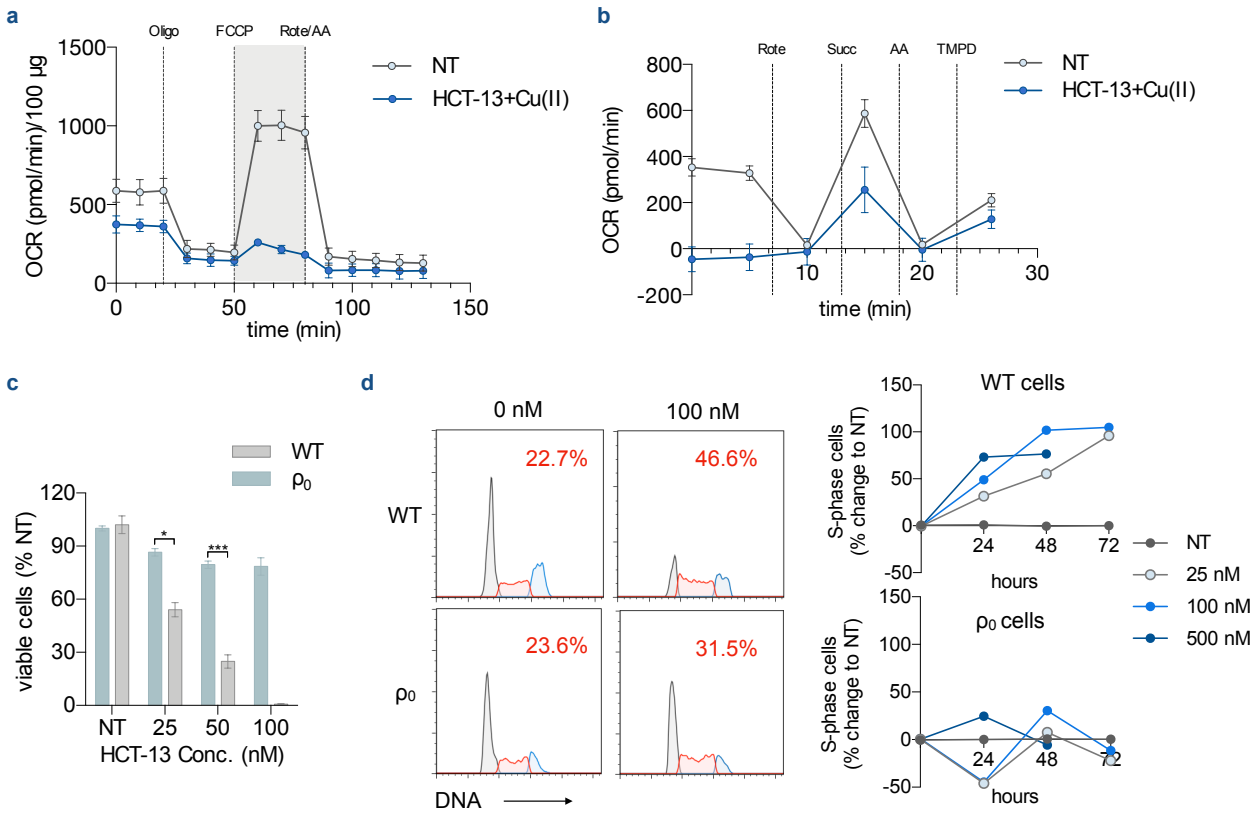

Fig. 3.5. HCT-13 alters cellular energetics through inhibition of electron transport chain and has selective mitochondrial toxicity. (**a**) Mito Stress Test of MIAPACA2 PDAC cells treated with HCT-13 (25 nM) + Cu(II) (20 µM) for 24h. (**b**) Electron flow assay in isolated mitochondria treated with HCT-13 (100 nM) + Cu(II) (20 µM) for 1h. (**c**) Viability of 143 BTK parental (wild type, WT) and ρ_0 cells after 48h of the indicated HCT-13 concentration + Cu(II) (20 µM) treatment, assessed with Trypan Blue Staining. (**d**) 48h cell cycle histogram and plots of S-phase arrest plots in 143 BTK WT and 143 BTK ρ_0 cells at 24, 48 and 72h following treatment with indicated concentrations of HCT-13 + Cu(II) (20 µM).

(mean ± SD, n = 2, one-way ANOVA corrected for multiple comparisons by Bonferroni adjustment, * $P < 0.05$; ** $P < 0.01$; *** $P < 0.001$).

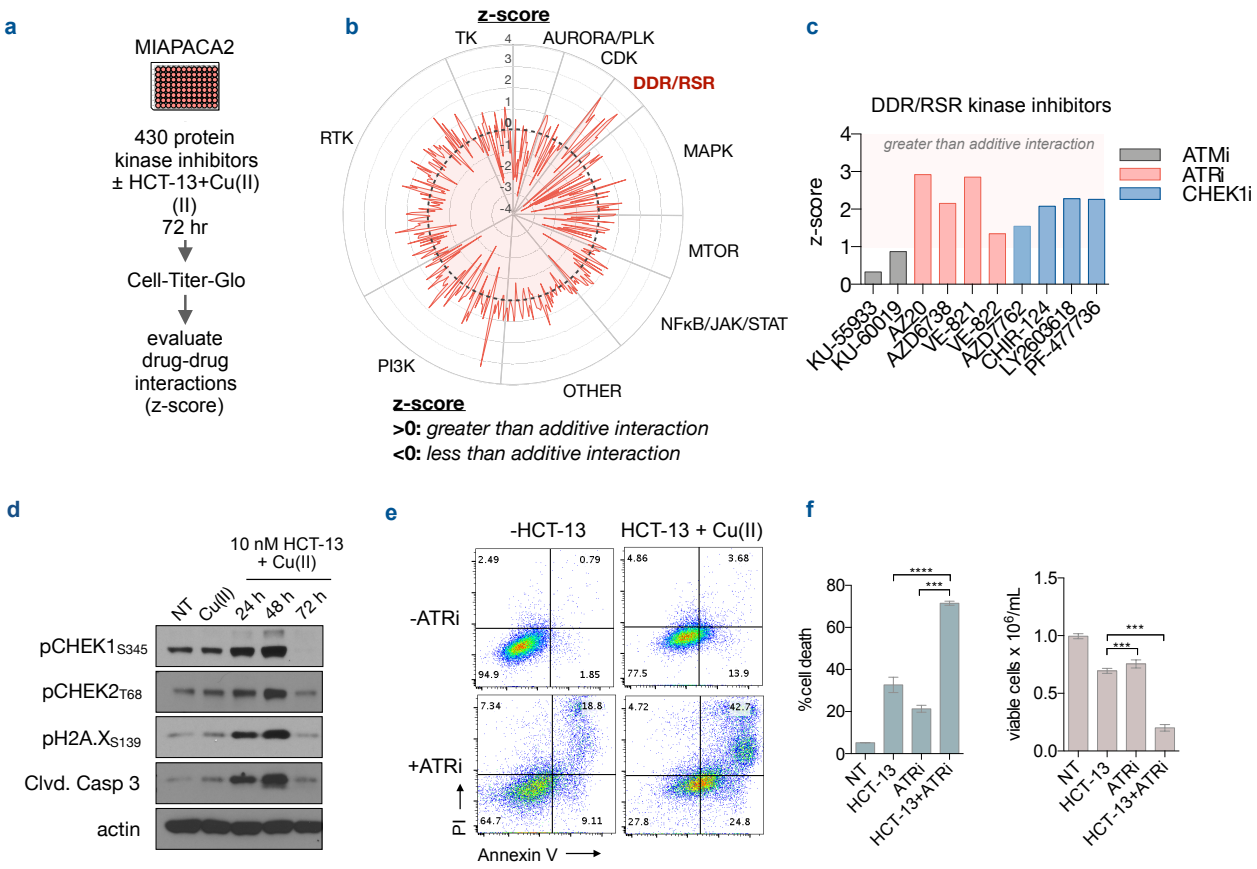

Fig. 3.6. A chemical genomics screen identifies the replication stress response pathway as an actionable co-dependency of HCT-13-treated cells. (**a**) Experimental design of a synthetic lethality screen using a library of protein kinase inhibitors against HCT-13-treated cells in the presence of Cu(II) (20 μM). (**b**) Radar plot of screen results. (**c**) z-score values for kinase inhibitors within the DNA damage response/replication stress response (DDR/RSR) pathway module. (**d**) Representative immunoblot of replication stress and cell death biomarkers in MIAPACA2 PDAC cells treated with HCT-13 (10 nM) + Cu(II) (20 μM). (**e**) Annexin V/PI staining in MIAPACA2 cells to validate the synergistic interaction of HCT-13 (25nM) + Cu(II) (20 μM) with ATRi (250nM VE-822) treated for 72h. (**f**) Trypan Blue Viability staining in MIAPACA2 cells to validate the synergistic interaction of HCT-13 (25nM) with ATRi (250nM VE-822) treated for 72h in presence of Cu(II) (20 μM).

(mean ± SD, n = 2, one-way ANOVA corrected for multiple comparisons by Bonferroni adjustment, * P < 0.05; ** P < 0.01; *** P < 0.001; **** P < 0.0001).F

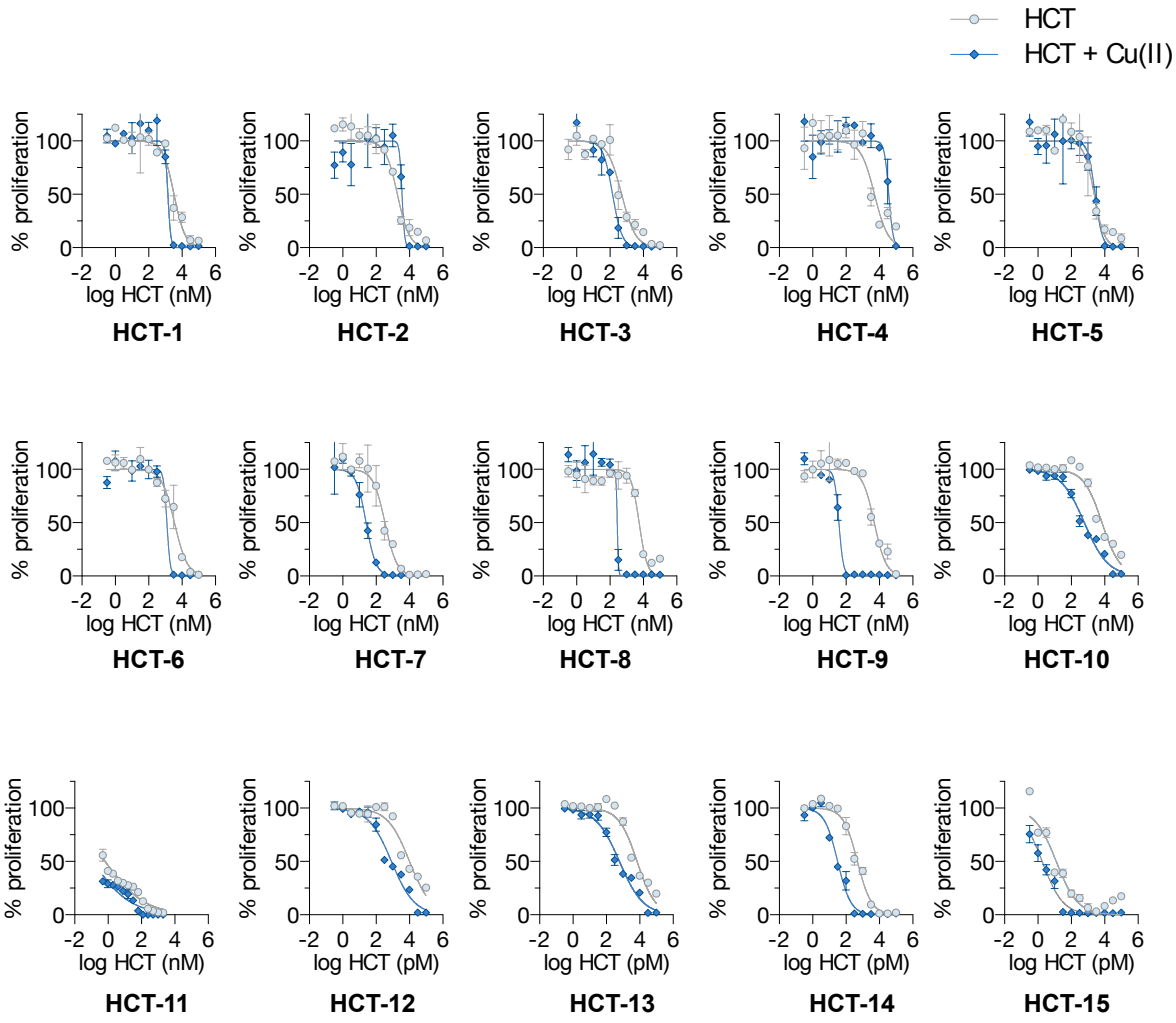

Fig. S3.1. Summary of HCT compound dose response curves. Viability curves measured with CellTiterGlo in MIAPACA2 cells treated with each HCT ± Cu(II) (20 μM) for 72h.

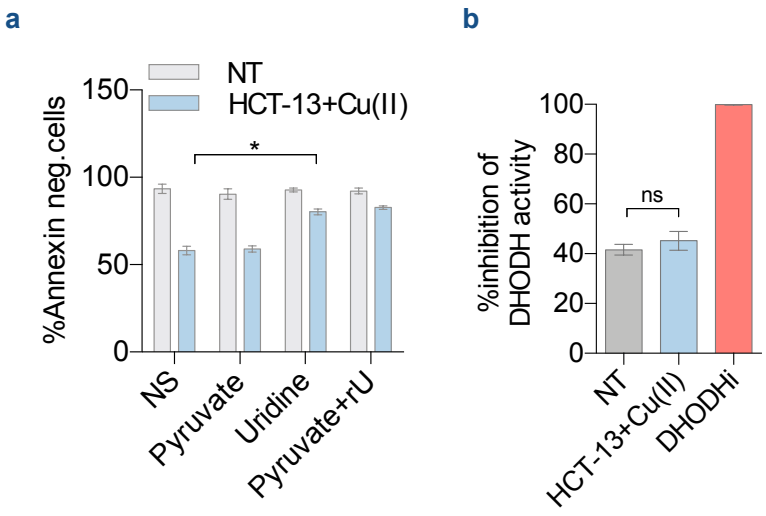

Fig. S3.2. Cell proliferation inhibition induced by HCT-13 is partially rescued by uridine supplementation. (**a**) Rescue of HCT-13 (25 nM)-induced cell death by Uridine (rU) (200 μM), Pyruvate (1 mM), or both following 48h of treatment (**b**) Measurement of DHODH activity using recombinant DHODH assay following treatment with indicated perturbations for 2 min. DHODH inhibitor used: NITD-982 - 1 μM; HCT-13 - 100 nM, 1 μM, (100 nM data shown); Cu(II) - 20 μM. (mean ± SD, n = 2, Student t-test, * $P < 0.05$).

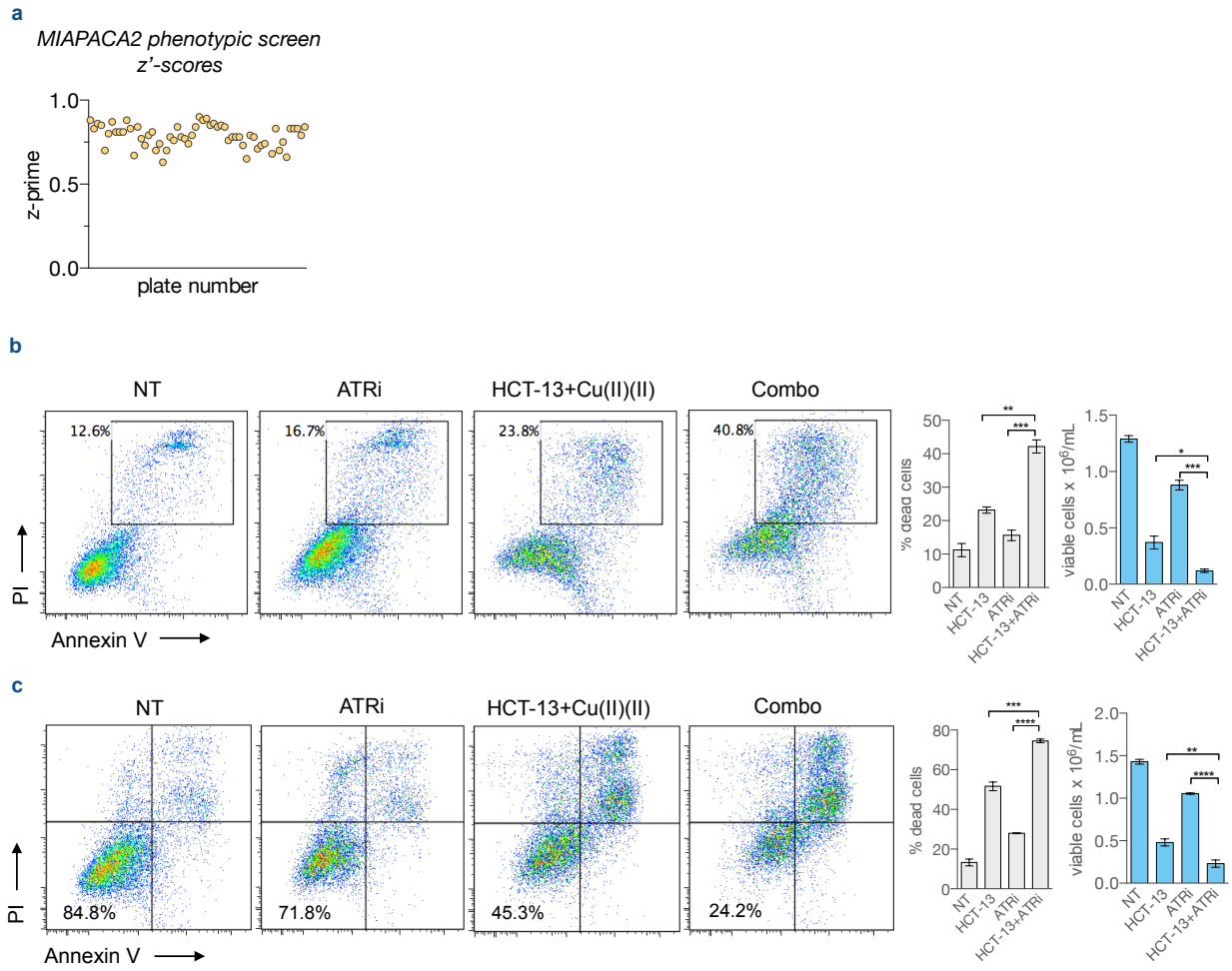

Fig. S3.3. Identification of resistance mechanisms to HCT-13 using a synthetic lethality screen (**a**) Assay quality, as measured by Z-factor (Z') scores (**b and c**) Annexin V/PI staining and Trypan Blue staining in CFPAC-1 PDAC cells and C4-2 PC cells to validate the synergistic interaction of HCT-13 with ATRi (250 nM VE-822) treated for 72h in presence of Cu(II) (20 μM). (mean ± SD, n = 2, one-way ANOVA corrected for multiple comparisons by Bonferroni adjustment, * P < 0.05; ** P < 0.01; *** P < 0.001; **** P < 0.0001).

REFERENCES

1. Brockman, R. W.; Thomson, J. R.; Bell, M. J.; Skipper, H. E. Observations on the Antileukemic Activity of Pyridine-2-carboxaldehyde Thiosemicarbazones and Thiocarbohydrazone*. *Cancer Res.* **1956**, *16*, 167-170.

2. Beraldo, H.; Gambino, D. The Wide Pharmacological Versatility of Semicarbazones, Thiosemicarbazones, and Their Metal Complexes. *Mini Rev. Med. Chem.* **2004**, *4*, 31-39.

3. Sartorelli, A. C. Effect of Chelating Agents Upon the Synthesis of Nucleic Acids and Protein: Inhibition of DNA Synthesis by 1-Formylisoquinoline Thiosemicarbazone. *Biochem. Biophys. Res. Commun.* **1967**, *27*, 26-32.

4. Liu, M. C.; Lin, T. S.; Sartorelli, A. C. Synthesis and Antitumor Activity of Amino Derivatives of Pyridine-2-carboxaldehyde Thiosemicarbazone. *J. Med. Chem.* **1992**, *35*, 3672-3677.

5. Agrawal, K. C.; Mooney, P. D.; Sartorelli, A. C. Potential Antitumor Agents. 13. 4-Methyl-5-amino-1-formylisoquinoline Thiosemicarbazone. *J. Med. Chem.* **1976**, *19*, 970-972.

6. French, F. A.; Blanz, E. J.; DoAmaral, J. R.; French, D. A. Carcinostatic Activity of Thiosemicarbazones of Formyl Heteroaromatic Compounds. VI. 1-Formylisoquinoline Derivatives Bearing Additional Ring Substituents, with Notes on Mechanism of Action. *J. Med. Chem.* **1970**, *13*, 1117-1124.

7. French, F. A.; Blanz, E. J. The Carcinostatic Activity of α-(N) Heterocyclic Carboxaldehyde Thiosemicarbazone. *Cancer Res.* **1965**, *25*, 1454-1458.

8. Karp, J. E.; Giles, F. J.; Gojo, I.; Morris, L.; Greer, J.; Johnson, B.; Thein, M.; Sznol, M.; Low, J. A Phase I study of the novel ribonucleotide reductase inhibitor 3-aminopyridine-2-carboxaldehyde thiosemicarbazone (3-AP, Triapine®) in combination with the nucleoside analog fludarabine for patients with refractory acute leukemias and aggressive myeloproliferative disorders. *Leuk. Res.* **2008**, *32*, 71-77.

9. Le, T. M.; Poddar, S.; Capri, J. R.; Abt, E. R.; Kim, W.; Wei, L.; Uong, N. T.; Cheng, C. M.; Braas, D.; Nikanjam, M.; Rix, P.; Merkurjev, D.; Zaretsky, J.; Kornblum, H. I.; Ribas, A.; Herschman, H. R.; Whitelegge, J.; Faull, K. F.; Donahue, T. R.; Czernin, J.; Radu, C. G. ATR Inhibition Facilitates Targeting of Leukemia Dependence on Convergent Nucleotide Biosynthetic Pathways. *Nat. Commun.* **2017**, *8*, 241.

10. Ohui, K.; Afanasenko, E.; Bacher, F.; Ting, R. L. X.; Zafar, A.; Blanco-Cabra, N.; Torrents, E.; Dömötör, O.; May, N. V.; Darvasiova, D.; Enyedy, É. A.; Popović-Bijelić, A. Reynisson, J.; Rapta, P.; Babak, M. V.; Pastorin, G.; Arion, V. B. New Water-Soluble Copper(II) Complexes with Morpholine-Thiosemicarbazone Hybrids: Insights into the Anticancer and Antibacterial Mode of Action. *J. Med. Chem.* **2018**, 62(2), 512-530.

11. Aye, Y.; Long, M. J.; Stubbe, J. Mechanistic Studies of Semicarbazone Triapine Targeting Human Ribonucleotide Reductase *in Vitro* and in Mammalian Cells. *J. Biol. Chem.* **2012**, *287*, 35768-35778.

12. Ma, B.; Goh, B. C.; Tan, E. H.; Lam, K. C.; Soo, R.; Leong, S. S.; Wang, L. Z.; Mo, F.; Chan, A. T.; Zee, B.; Mok, T. A multicenter phase II trial of 3-aminopyridine-2-carboxaldehyde thiosemicarbazone (3-AP, Triapine®) and gemicitabine in advanced non-small-cell lung cancer with pharmacokinetic evaluation using peripheral blood mononuclear cells. *Invest. New Drugs* **2008**, *26*, 169-173.

13. Knox, J. J.; Hotte, S. J.; Kollmannsberger, C.; Winquist, E.; Fisher, B.; Eisenhauer, E. A. Phase II study of Triapine® in patients with metastatic renal cell carcinoma: a trial of the National Cancer Institute of Canada Clinical Trials Group (NCIC IND.161). *Invest. New Drugs* **2007**, *25*, 471-477.

14. Yu, Y.; Kalinowski, D. S.; Kovacevic, Z.; Siafakas, A. R.; Jansson, P. J.; Stefani, C.; Lovejoy, D. B.; Sharpe, P. C.; Bernhardt, P. V.; Richardson, D. R. Thiosemicarbazone from the Old to New: Iron Chelators That are More Than Just Ribonucleotide Reductase Inhibitors. *J. Med. Chem.* **2009**, *52*, 5271-5294.

15. Salim, K. Y.; Maleki Vareki, S.; Danter, W. R.; Koropatnick, J. COTI-2, a novel small molecule that is active against multiple human cancer cells in lines *in vitro* and *in vivo*. *Oncotarget* **2016**, *7*, 41363-41379.

16. Guo, Z. L.; Richardson, D. R.; Kalinowski, D. S.; Kovacevic, Z.; Tan-Un, K. C.; Chan, G. C. *J.* The novel thiosemicarbazone, di-2-pyridylketone 4-cyclohexyl-4-methyl-3-thiosemicarbazone (DpC), inhibits neuroblastoma growth in vitro and in vivo multiple mechanisms*. Hematol. Oncol.* **2016**, *9*, 98.

17. Malarz, K.; Mrozek-Wilczkiewicz, A.; Serda, M.; Rejmund, M.; Polanski, J.; Musiol, R. The role of oxidative stress in activity of anticancer thiosemicarbazones. *Oncotarget* **2018**, *9*, 17689-17710.

18. Finch, R. A.; Liu, M. C.; Cory, A. H.; Cory, J. G.; Sartorelli, A. C. Triapine (3-aminopyridine-2-carboxaldehyde thiosemicarbazone; 3-AP): an inhibitor of ribonucleotide reductase with antineoplastic activity. *Adv. Enzyme Regul.* **1999**, *39*, 3-12.

19. Yu, Y.; Wong, J.; Lovejoy, D. B.; Kalinowski, D. S.; Richardson, D. R. Chelators at the Cancer Coalface: Desferrioxamine to Triapine and Beyond. *Clin. Cancer. Res.* **2006**, *12*, 6876-6883.

20. Alvero, A. B.; Chen, W.; Sartorelli, A. C.; Schwartz, P.; Rutherford, T.; Mor, G. Triapine (3-aminopyridine-2-carboxaldehyde thiosemicarbazone) Induces Apoptosis in Ovarian Cancer Cells. *J. Soc. Gynecol. Investig.* **2006**, *13*, 145-152.

21. Yu, Y.; Gutierrez, E.; Kovacevic, Z.; Saletta, F.; Obeidy, P.; Suryo Rahmanto, Y.; Richardson, D. R. Iron Chelators for the Treatment of Cancer. *Curr. Med. Chem.* **2012**, *19*, 2689-2702.

22. Merlot, A. M.; Kalinowski, D. S.; Richardson, D. R. Novel Chelators Treatment: Where Are We Now? *Antioxid. Redox Signal.* **2013**, *18*, 973-1006.

23. Chaston, T. B.; Lovejoy, D. B.; Watts, R. N.; Richardson, D. R. Examination of the Antiproliferative Activity of Iron Chelators: Multiple Cellular Targets and the Different Mechanism of Action of Triapine Compared with Desferrioxamine and the Potent Pyridoxal Isonicotinoyl Hydrazone Analogue 311. *Clin. Cancer Res.* **2003**, *9*, 402-414.

24. Cory, J. G.; Cory, A. H.; Rappa, G.; Lorico, A.; Liu, M. C.; Lin, T. S.; Sartorelli, A. C. Inhibitors of ribonucleotide reductase: comparative effects of amino- and hydroxy-substituted pyridine-2-carboxaldehyde thiosemicarbazones. *Biochem. Pharmacol.* **1994**, *48*, 335-344.

25. Richardson, D. R.; Kalinowski, D. S.; Richardson, V.; Sharpe, P. C.; Lovejoy, D. B.; Islam, M.; Bernhardt, P. V. 2-Acetylpyridine Thiosemicarbazones are Potent Iron Chelators and Antiproliferative Agents: Redox Activity, Iron Complexation and Charaterization of their Antitumor Activity. *J. Med. Chem.* **2009**, *52*, 1459-1470.

26. Popović-Bijelić, A.; Kowol, C. R.; Lind, M. E.; Luo, J.; Himo, F.; Enyedy, E. A.; Arion, V. B.; Gräslund, A. Ribonucleotide reductase inhibition by metal complexes of Triapine (3-aminopyridine-2-carboxaldehyde thiosemicarbazone): A combined experimental and theoretical study. *J. Inorg. Biochem.* **2011**, *105*, 1422-1431.

27. Ishiguro, K.; Lin, Z. P.; Penketh, P. G.; Shyam, K.; Zhu, R.; Baumann, R. P.; Zhu, Y. L.; Sartorelli, A. C.; Rutherford, T. J.; Ratner, E. S. Distinct mechanisms of cell-kill by triapine and its terminally dimethylated derivative Dp44mT due to a loss or gain of activity of their copper(II) complexes. *Biochem. Pharmacol.* **2014**, *91*, 312-322.

28. Denoyer, D.; Clatworthy, S. A.; Masaldan, S.; Meggyesy, P. M.; Cater, M. A. Heterogeneous copper concentrations in cancerous human prostate tissues. *Prostate* **2015**, *75*, 1510-1517.

29. Madsen, E.; Gitlin, J. D. Copper and Iron Disorders of the Brain. *Annu. Rev. Neurosci.* **2007**, *30*, 317-337.

30. Jansson, P. J.; Yamagishi, T.; Arvind, A.; Seebacher, N.; Gutierrez, E.; Stacy, A.; Maleki, S.; Sharp, D.; Sahni, S.; Richardson, D. R. Di-2-pyridylketone 4,4-Dimethyl-3-thiosemicarbazone Overcomes Multidrug-Resistance by Novel Mechanism Involving the Hijacking of Lysosomal P-Glycoprotein (Pgp). *J. Biol. Chem.* **2015**, *290*, 9588-9603.

31. Whitnall, M.; Howard, J.; Ponka, P.; Richardson, D. R. A class of iron chelators with a wide spectrum of potent antitumor activity that overcomes resistance to chemotherapeutics. *Proc. Natl. Acad. Sci. USA* **2006**, *103*, 14901-14906.

32. Shimada, K.; Reznik, E.; Stokes, M. E.; Krishnamoorthy, L.; Bos, P. H.; Song, Y.; Quartararo, C. E.; Pagano, N. C.; Carpizo, D. R.; deCarvalho, A. C.; Lo, D. C.; Stockwell, B. R. Copper-Binding Small Molecule Induces Oxidative Stress and Cell-Cycle Arrest in Glioblastoma-Patient-Derived Cells. *Cell Chem. Biol.* **2018**, *25*, 585-594.

33. Chen, D.; Cui, Q. C.; Yang, H.; Dou, Q. P. Disulfiram, a Clinically Used Anti-Alcoholism Drug and Copper-Binding Agent, Induces Apoptotic Cell Death in Breast Cancer Cultures and Xenografts via Inhibition of the Proteasome Activity. *Cancer Res.* **2006**, *66*, 10425-10433.

34. Brewer, G. J.; Dick, R. D.; Grover, D. K.; LeClaire, V.; Tseng, M.; Wicha, M.; Pienta, K.; Redman, B. G.; Jahan, T.; Sondak, V. K.; Strawderman, M.; LeCarpentier, G.; Merajver, S. D. Treatment of Metastatic Cancer with Tetrathiomolybdate, an Anticopper, Antiangiogenic Agent: Phase I Study. *Clin. Cancer Res.* **2000**, *6*, 1-10.

35. Cen, D.; Gonzalez, R. I.; Buckmeier, J. A.; Kahlon, R. S.; Tohidian, N. B.; Meyskens, F. L. Disulfiram Induces Apoptosis in Human Melanoma Cells: A Redox-related Process. *Mol. Cancer Ther.* **2002**, *1*, 197-204.

36. Müller, K.; Faeh, C.; Diederich, F. Fluorine in Pharmaceuticals: Looking Beyond Intuition. *Science.* **2007**, *317*, 1881-1886.

37. Purser, S.; Moore, P. R.; Swallow, S.; Gouverneur, V. Fluorine in Medicinal Chemistry. *Chem. Soc. Rev.* **2008**, *37*, 320-330.

38. Zhou, Y.; Wang, J.; Gu, Z.; Wang, S.; Zhu, W.; Aceña, J. L.; Soloshonok, V. A.; Izawa, K.; Liu, H. Next Generation of Fluorine-Containing Pharmaceuticals, Compounds Currently in Phase II-III Clinical Trials of Major Pharmaceutical Companies: New Structural Trends and Therapeutic Areas. *Chem. Rev.* **2016**, *116*, 422-518.

39. Kowol, C. R.; Trondl, R.; Heffeter, P.; Arion, V. B.; Jakupec, M. A.; Roller, A.; Galanski, M.; Berger, W.; Keppler, B. K. Impact of Metal Coordination on Cytotoxicity of 3-Aminopyridine-2-carboxaldehyde Thiosemicarbazone and Novel Insights into Terminal Dimethylation. *J. Med. Chem.* **2009**, *52*, 5032-5043.

40. Kowol, C. R.; Miklos, W.; Pfaff, S.; Hager, S.; Kallus, S.; Pelivan, K.; Kubanik, M.; Enyedy, É. A.; Berger, W.; Heffeter, P.; Keppler, B. K. Impact of Stepwise NH_2-Methylation of Triapine on the Physicochemical Properties, Anticancer Activity, and Resistance Circumvention. *J. Med. Chem.* **2016**, *59*, 6739-6752.

41. Agrawal, K. C.; Booth, B. A.; Sartorelli, A. C. Potential Antitumor Agents. I. A series of 5-Substituted 1-Formylisoquinoline Thiosemicarbazones. *J. Med. Chem.* **1968**, *11*, 700-703.

42. Mooney, P. D.; Booth, B. A.; Moore, E. C.; Agrawal, K. C.; Sartorelli, A. C. Potential Antitumor Agents. 10. Synthesis and Biochemical Properties of 5-N-Alkylamino-, N,N-Dialkylamino-, and N-Alkylacetamido-1-formylisoquinoline Thiosemicarbazones. J. *Med. Chem.* **1974**, *17*, 1145-1150.

43. Denoyer, D.; Pearson, H. B.; Clatworthy, S. A.; Smith, Z. M.; Francis, P. S.; Llanos, R. M.; Volitakis, I.; Phillips, W. A.; Meggyesy, P. M.; Masaldan, S.; Cater, M. A. Copper as a target for prostate cancer therapeutics: copper-ionophore pharmacology and altering systemic copper distribution. *Oncotarget* **2016**, *7*, 37064-37080.

44. Cater, M. A.; Pearson, H. B.; Wolyniec, K.; Klaver, P.; Bilandzic, M.; Paterson, B. M.; Bush, A. I.; Humbert, P. O.; La Fontaine, S.; Donnelly, P. S.; Haupt, Y. Increasing Intracellular

Bioavailable Copper Selectivity Targets Prostate Cancer Cells. *ACS Chem. Biol.* **2013**, *8*, 1621-1631.

45. Safi, R.; Nelson, E. R.; Chitneni, S. K.; Franz, K. J.; George, D. J.; Zalutsky, M. R.; McDonnell, D. P. Copper signaling axis as a target for prostate cancer therapeutics. *Cancer Res.* **2014**, *74*, 5819-5831.

46. Kodydkova, J.; Vavrova, L.; Stankova, B.; Macasek, J.; Krechler, T.; Zak, A. Antioxidant Status and Oxidative Stress Markers in Pancreatic Cancer and Chronic Pancreatitis. *Pancreas* **2013**, *42*, 614-621.

47. Lener, M. R.; Scott, R. J.; Wiechowska-Kozłowska, A.; Serrano-Fernández, P.; Baszuk, P.; Jaworska-Bieniek, K.; Sukiennicki, G.; Marciniak, W.; Muszyńska, M.; Kładny, J.; Gromowski, T.; Kaczmarek, K.; Jakubowska, A.; Lubiński. Serum concentration of selenium and copper in patients diagnosed with pancreatic cancer. *Cancer Res. Treat.* **2016**, *48*, 1056-1064.

48. Zhang, X.; Yang, Q. Association between serum copper levels and lung cancer risk: A meta-analysis. *J. Int. Med. Res.* **2018**, 46(12), 4863-4873.

49. Herzig, S.; Shaw, R. AMPK: guardian of metabolism and mitochondrial homeostasis. *Nat. Rev. Mol. Cell Biol.* **2018**, *19*, 121-135.

50. Krishan, S.; Richardson, D. R.; Sahni, S. The Anticancer Agent, Di-2-Pyridylketone 4,4-Dimethyl-3-Thiosemicarbazone (Dp44mT), Up-Regulates the AMPK-Dependent Energy Homeostasis Pathway in Cancer Cells. *Biochem. Biophys. Acta.* **2016**, *1863*, 2916-2933.

51. Englinger, B.; Pirker, C.; Heffeter, P.; Terenzi, A.; Kowol, C. R.; Keppler, B. K.; Berger, W. Metal Drugs and the Anticancer Immune Response. Metal Drugs and the Anticancer Immune Response. *Chem. Rev.* **2019**, 119, 1519-1624.

52. Madak, J. T.; Bankhead, A.; Cuthbertson, C. R.; Showalter, H. D.; Neamati, N. Revisiting the role of dihydroorotate dehydrogenase as a therapeutic target for cancer. *Pharmacol. Ther.* [Online early access, in press]. DOI: https://doi.org/10.1016/j.pharmthera.2018.10.012. Published online: October 19, **2018**.

53. Löffler, M.; Jöckel, J.; Schuster, G. & Becker, C. Dihydroorotat-ubiquinone oxidoreductase links mitochondria in the biosynthesis of pyrimidine nucleotides. *Mol. Cell Biochem.* **1997**, *174*, 125-129.

54. Rawls, J.; Knecht, W.; Diekert, K.; Lill, R.; Löffler, M. Requirements for the mitochondrial import and localization of dihydroorotate dehydrogenase. *Eur. J. Biochem.* **2000**, *267*, 2079-2087.

55. Zameitat, E.; Freymark, G.; Dietz, C. D.; Löffler, M.; Bölker, M. Functional Expression of Human Dihydroorotate Dehydrogenase (DHODH) in *pyr4* Mutants of *Ustilago maydis* Allows Target Validation of DHODH Inhibitors In Vivo. *Appl. Environ. Microbiol.* **2007**, *73*, 3371-3379.

56. Lane, A. N.; Fan, T. W. Regulation of mammalian nucleotide metabolism and biosynthesis. *Nucleic Acids Res.* **2015**, *43*, 2466-2485.

57. Morais, R.; Desjardins, P.; Turmel, C.; Zinkewich-Péotti, K. Development and Characterization of continuous avian cell lines depleted of mitochondrial DNA. *In Vitro Cell. Dev. Biol.* **1988**, *24*, 649-658.

CHAPTER 4

Metabolic modifier screen reveals secondary targets of protein kinase inhibitors within nucleotide metabolism

ABSTRACT

A cell-based metabolic modifier screening platform for the discovery of modulators of convergent pyrimidine nucleotide biosynthetic pathways was designed and implemented. In screening a library of protein kinase inhibitors, multiple compounds were shown to possess previously uncharacterized metabolism modifying activity. The JNK inhibitor JNK-IN-8 was found to be a potent inhibitor of nucleoside transport, a property which was confirmed using nucleoside-analog PET imaging in mice. The PDK1 inhibitor OSU-03012 (also known as AR-12) and the RAF inhibitor TAK-632 were shown to inhibit the therapeutically relevant enzyme dihydroorotate dehydrogenase (DHODH) and their affinity unambiguously confirmed through *in vitro* assays and co-crystallization with human DHODH.

INTRODUCTION

The redundant and plastic nature of metabolic networks represents a significant obstacle in the targeting of cancer metabolism. This hurdle manifests in two ways, the first being redundancy in enzymes performing identical biochemical reactions, such as the hexokinase isozymes which phosphorylate glucose(Xu et al., 2018). The second is the presence of convergent, parallel metabolic pathways producing a common metabolite from unique precursors, usually consisting of scavenging and *de novo* arms. Convergent metabolic nodes have been noted in nucleotide(Le et al., 2017), lipid (cholesterol)(York et al., 2015) and amino acid (aspartate) metabolism (Garcia-Bermudez et al., 2018).

Despite these difficulties, the development of metabolism modifiers remains a robust area of research. One such therapeutically relevant target is pyrimidine nucleotide biosynthesis which consists of nucleoside scavenging (NSP) and *de novo* (DNP) pathways which both generate uridine monophosphate (UMP), the common precursor for all pyrimidine nucleotides (Okesli, Khosla, & Bassik, 2017). The NSP scavenges preformed nucleosides from the extracellular environment, shuttling them into the cell via nucleoside transporters where they are phosphorylated by uridine-cytidine kinases (UCKs) to produce UMP. It is thought that UCK2 is the primary NSP kinase, given its 20-fold higher catalytic efficiency compared with isozyme UCK1(An R. Van Rompay, Karin Linden, Magnus Johansson, Anna Karlsson, 2001). The DNP consists of a six-step process that utilizes glutamine, aspartate and bicarbonate to produce UMP through the action of the trifunctional enzyme CAD, electron transport chain-linked dihydroorotate dehydrogenase (DHODH), and bifunctional UMP synthase (UMPS). Amongst these proteins, DHODH in particular has been the subject of significant research interest in anticancer settings(Madak, Bankhead, Cuthbertson, Showalter, & Neamati, 2019; Sykes et al., 2016), including pancreatic ductal adenocarcinoma (PDAC)(Santana-Codina et al., 2018). This interest is complemented by over 90 patent applications involving DHODH inhibition in the last decade(Lolli et al., 2018).

In this study, we show that the pyrimidine NSP and DNP are interchangeable in their ability to sustain cancer cell proliferation and that a synthetic lethal phenotype can be achieved through their simultaneous inhibition. With this knowledge, we construct a metabolic modifier screen for identifying selective modulators of NSP and DNP pathways. In screening a library of protein kinase inhibitors, we found that the c-Jun N-terminal kinase (JNK) inhibitor JNK-IN-8 is a potent inhibitor of nucleoside transporters vital for NSP function, and that the 3-phosphoinositide-dependent protein kinase 1 (PDK1) inhibitor OSU-03012 (also known as AR-12) and the pan-RAF inhibitor TAK-632 both bind and inhibit the pyrimidine DNP enzyme DHODH.

METHODS AND MATERIALS

Data Availability

Full kinase inhibitor library phenotypic screen results are included as **Supplemental Table 1**. The accession numbers for the protein structure data reported are **6OC0** (OSU-03012:DHODH) and **6OC1B (**TAK-632:DHODH).

Cell culture

All cell cultures were between passages 3 and 20 and maintained in antibiotic free DMEM or RPMI +10% dialyzed FBS, at 37ºC in 5% CO_2. We routinely monitored for mycoplasma contamination using the PCR-based Venor Mycoplasma kit. PDAC cell lines were acquired either from a commercial vendor (ATCC, DSMZ) or from collaborators. Cell line identity was independently authenticated by PCR.

Drugs

Drug stocks were prepared in DMSO or H_2O and diluted fresh in cell culture media for treatments. NITD-982 was synthesized as previously described by Dr. Daniel Sun and Ethan Rosser (UCLA)(Bonavia et al., 2011).

In vivo mouse studies

All animal studies were approved by the UCLA Animal Research Committee (ARC). 4-6 week-old female NSG mice, obtained from UCLA Radiation Oncology, were injected subcutaneously on bilateral flanks with $0.5x10^6$ CCRF-CEM cells suspended 1:1 in PBS:matrigel. **20** d post-inoculation treatment was initiated. JNK-IN-8 was suspended in 2% ethanol and 5% Tween-80 in PBS and administered by intraperitoneal (i.p.) injection at 25 mg/kg.

Protein kinase inhibitor phenotypic screen

A library of 430 protein kinase inhibitors was arrayed in polypropylene 384-well plates at 200x concentrations covering a 7-point concentration range (corresponding to 1x concentrations: 5μM, 1.65μM, 550nM, 185nM, 61.5nM, 20.6nM, 6.85nM). 25μl per well of condition-specific growth media (DNP+NSP: media +10 μM rU; DNP: media alone; NSP: media +10 μM rU + 1 μM NITD-982) was plated in opaque-white 384-well plates using a BioTek multidrop liquid handler. Protein kinase inhibitors were added by 250 nL pin-tool transfer (BioMek FX, Beckman-Coulter) and inhibitor/media mixtures were incubated at room temperature for 30 m. 25 μL of a 40,000 cells/mL MIAPACA2 suspension (for 1000 cells / well) was subsequently added to each well. After 72 h, 50 μL of CellTiter-Glo reagent diluted 1:4 in dH_2O was added to each well and

luminescence was measured using a Wallac plate reader (Perkin Elmer). Each condition was assayed in duplicate (n=2) and % proliferation values were calculated by normalizing experimental wells to plate negative controls and averaging replicate values. Composite pathway selectivity synergy scores for each test compound were defined as the sum of the excess over Bliss additivity scores (% proliferation inhibition observed - % proliferation inhibition expected) between individual protein kinase inhibitor concentrations across the 7-point concentration range. Z factor scores for individual assay plates were calculated using eight positive and eight negative control wells on each plate as previously described(Ji-Hu Zhang, 1999). All plates gave a Z factor > 0.5 (**Figure S3C**).

^{3}H-rU and ^{3}H-dC uptake assays

Radioactive probe uptake assays were conducted as previously described (Campbell et al., 2011). Briefly, 5 ×10^{5} CCRF-CEM cells were resuspended in 1 mL of media per well in 12-well plates. After 1 h, cells were incubated with the indicated amounts of tritiated probe ± JNK-IN-8 for an additional hour. Cells were then harvested and washed twice with ice-cold PBS. Radioactivity was measured using a beta-counter (Perkin-Elmer).

Positron Emission Tomography (PET) imaging

MicroPET/CT experiments were conducted as previously described (Shu et al., 2010). Briefly, prewarmed and anesthetized NSG mice were injected with [^{18}F]CFA, and PET and CT images were acquired using the G8 PET/CT scanner (Sofie Biosciences) 4 h after i.p. administration of JNK-IN-8 or its vehicle and 3 h after the injection of 740 kBq of [^{18}F]CFA.

Radiochemical Synthesis of [^{18}F]-Labeled Probes.

The syntheses of [^{18}F]CFA was performed as previously described (Shu et al., 2010).

Flow cytometry

All flow cytometry data were acquired on five-laser BD LSRII, and analyzed using FlowJo software (Tree Star).

AnnexinV/PI: Treated PDAC cells were washed with PBS and incubated with AnnexinV and propidium iodide diluted in 1x Annexin binding buffer. 20,000 events were collected per sample.

Propidium iodide cell cycle analysis: Treated PDAC cells were washed with PBS and suspended in propidium iodide cell cycle staining solution (100 µg/ml propidium iodide; 20 µg/ml Ribonuclease A). 10,000 events were collected per sample.

Viability analysis

For CellTiter-Glo analysis cells were plated at $1x10^3$ cells / well in at 50 µl / well in white opaque 384-well plates and treated as described. Following incubation 50 µl of CellTiter-Glo reagent (Diluted 1:5 in dH_2O) was added to each well, plates incubated at room temperature for 5 m and luminescence was measured using a BioTek microplate luminescence reader. Proliferation rate normalized growth inhibition was calculated using the previously described GR metric (Hafner et al., 2016).

For crystal violet staining, PDAC cells were plated in 6-well cell culture plates at $1x10^4$ cells/well and treated as described. Following treatment cells were fixed by incubating in 4% PFA in PBS for 15 m at room temperature. Plates were subsequently washed with PBS and stained with 0.1% crystal violet in H_2O for 15 m at room temperature.

Gene cloning, protein expression, and purification of DHODH in E.coli cells

Primers were ordered to add NdeI (AGAGAACAGATTGGTGGTCATATGATGGCCACGGGAGATGAG) upstream of residue 29 (after the mitochondrial membrane associated loop) and BamHI (TCGGGCTTTGTTAGCAGCCGGATCCTTACCTCCGATGATCTGCTCC) after the stop codon to insert into N-terminal His-Sumo pET 14b vector. This clone, His-Sumo-DHODH 29-395 (subsequently referred to as DHODH) was successfully inserted into the vector in XL1-blue cells for vector propagation.

The vector was transformed into C41(DE3) cells for productions. Cells were grown at 37 °C in 2xYT medium supplemented with 100 µg/mL ampicillin (Amp), treated with 0.1 mM isopropyl β-D-1-thiogalactopyranoside (IPTG) at an OD600 nm of 0.6-0.8, and then cultured for an additional 18h at 18 °C. Cells were harvested by centrifugation, washed with 200 mM NaCl and 25 mM Tris pH 7.5, and pelleted at 5000 rpm for 20 minutes before storage at -20°C. 6.7g/L of cell pellet was obtained.

DHODH was purified according to known purification conditions(Baumgartner et al., 2006). Cell pellet was resuspended in lysis buffer (50 mM Tris pH 7.5; 600 mM NaCl; 0.33% w/v Thesit; 10% Glycerol; 1 mM PMSF) and lysed by sonication on ice. Lysed cells were centrifuged at 58,500 RCF for 45 minutes at 4°C, and the supernatant was filtered through a 0.45 µM filter and loaded onto a 5-mL His-Trap column pre-equilibrated with buffer A (50 mM Tris pH 7.4; 600 mM NaCl; 0.05% w/v Thesit; 10% Glycerol). The column was washed with buffer A for 70 mL, buffer A with 25 mM imidazole for 50 mL, and buffer A with 50 mM imidazole for 50 mL. The protein was eluted with buffer A with 250 mM imidazole. The eluted fraction was diluted 1:1 with Buffer A. Sumo protease was added and the protein was dialyzed overnight at 4°C against 1L of Buffer

A. The dialyzed protein was loaded back onto the His-Trap column equilibrated with buffer A. The cut-DHODH was eluted with buffer A with 50 mM imidazole. The purified protein was concentrated to 5 mL and injected onto S-200 gel filtration column (GE Healthcare) equilibrated with: 50 mM HEPES pH 7.7, 400 mM NaCl, 10% Glycerol, 1mM EDTA, 0.05 % w/v Thesit. Eluted fractions consistent with monomer size were collected, concentrated, flash frozen, and stored at -80°C.

Recombinant DHODH enzyme assay

Evaluation of DHODH inhibition was performed as previously described(Baumgartner et al., 2006). Purified recombinant DHODH was incubated in an aqueous solution (total volume, 1.0 mL) containing 500 μM DHO, 200 mM K_2CO_3-HCl (pH 8.0), 0.2% triton X-100, and 100 μM coenzyme Q10 at 37 °C for 0, 15, 30, 45, or 60 m. An aliquot (100 μL) of the mixture of enzyme reaction mixture or cell/tissue lysate was mixed with 100 μL of 0, 0.5, or 1.0 μM orotic acid, 50 μL of H_2O, 250 μL of 4.0 mM 4-TFMBAO, 250 μL of 8.0 mM $K_3[Fe(CN)_6]$, and 250 μL of 80 mM K_2CO_3 and then heated at 80 °C for 4 m. The reaction was stopped by cooling in an ice-water bath and the absorbance was measured with a spectrofluorometer (FP-6300 Jasco, Tokyo, Japan): excitation and emission wavelengths were 340 nm and 460 nm, respectively.

Crystallization of DHODH with OSU-03012 and TAK-632 compounds

For co-crystallizaion of DHODH and OSU-03012, crystals were obtained using the same conditions reported in previously published DHODH structures(Lewis et al., 2016; Baumgartner et al., 2006; Das et al., 2013; Davies et al., 2009; Erra et al., 2011; Hurt, Sutton, & Clardy, 2006; Ladds et al., 2018; Liu, Neidhardt, Grossman, Ocain, & Clardy, 2000; McLean et al., 2010; Sainas et al., 2018; Walse et al., 2008), namely 1.6 – 2.6 M ammonium sulfate and 5-30% glycerol in the well in pH 4.5, with 20 mg/mL DHODH with 2 mM dihydroorotate (DHO), 20.8 mM dodecyldimethyl-N-amineoxide (DDAO), and 400 μM inhibitor. Protein was mixed 1:1 with mother liquor and hanging drops were used at room temperature. Crystals appeared after 48 hours and reached maximal size within one week. Molecular replacement used 4OQV (Deng et al., 2014) as the starting model. Interestingly, DHODH-TAK-632 crystals grown in similar conditions to those used for the DHODH-OSU-03012 complex did not show TAK-632 density. As a result, novel DHODH crystallization conditions were identified using commercial screens. For co-crystallization of DHODH with TAK-632, crystals were obtained in conditions of 1.4-1.6 M sodium phosphate, pH 8.2. Protein solution (20 mg/mL DHODH with 2 mM DHO, 20.8 mM DDAO, and 400 μM inhibitor) was mixed 1:1 with mother liquor and hanging drops were used at room temperature. Crystals appeared after 48 hours and reached maximal size within one week. Ligplot+ (Laskowski & Swindells, 2011; Wallace, Laskowski, & Thornton, 1995) was used

to determine hydrophilic and hydrophobic interactions between inhibitors and DHODH molecules.

Immunoblot analysis

PBS-washed cell pellets were resuspended in cold RIPA buffer supplemented with protease and phosphatase inhibitors. Protein lysates were normalized using BCA assay, diluted using RIPA and 4x laemmli loading dye, resolved on 4-12% Bis-Tris gels and electro-transferred to nitrocellulose membranes. After blocking with 5% nonfat milk in TBS + 0.1% Tween-20 (TBS-T), membranes were incubated overnight in primary antibodies diluted (per manufacturers instructions) in 5% BSA in TBS-T. Membranes were washed with TBST-T and incubated with HRP-linked secondary antibodies prepared at a 1:2500 dilution in 5% nonfat dry milk in TBS-T. HRP was activated by incubating membranes by incubating membranes with mixture of SuperSignal Pico and SuperSignal Femto ECL reagents (100:1 ratio). Exposure of autoradiography film was used for detection.

Statistical analyses

Data are presented as mean ± SD with number of biological replicates indicated. Comparisons of two groups were calculated using indicated unpaired two-tailed Student's t-test and P values less than 0.05 were considered significant. For some experiments, generated mean normalized values (ratios from two groups, treated to untreated) were compared to the hypothetical value 1 (indicating equal values between treated and untreated), calculated using one-sample t-test, and P values less than 0.05 were considered significant. Comparisons of more than two groups were calculated using one-way ANOVA followed by Bonferroni's multiple comparison tests, and P values less than 0.05/m, where m is the total number of possible comparisons, were considered significant.

RESULTS

Design of a differential metabolic modifier screen for identification of novel modulators of pyrimidine nucleotide metabolism

While redundant routes for UMP biosynthesis can complicate targeting, impaired proliferation resulting from simultaneous restriction of both routes can be used to identify selective modifiers of either NSP or DNP pathway activity (**Figure S1A**). A differential metabolic modifier screen was developed for the discovery of small molecule modulators of UMP production by leveraging this biosynthetic redundancy. This cell-based screening platform concurrently tests the effects of small molecule compounds on the proliferation of cells in baseline (NSP and DNP active), NSP-only, and DNP-only conditions (**Figure 1A**). Molecules which inhibit proliferation in baseline conditions are classified as non-specific inhibitors. Those which inhibit proliferation in NSP-only conditions are NSP inhibitors, while those that inhibit growth in DNP-only conditions are DNP inhibitors. The screen design was validated using the known DHODH inhibitor NITD-982 (Wang et al., 2011) and the FDA-approved nucleotide transport inhibitor dipyridamole (DPA), using CellTiter-Glo (CTG) to evaluate proliferation impairment (**Figure S1B**).

Cancer cell lines exhibited varying degrees of sensitivity to NITD-982 (as determined by doubling-time-normalized proliferation inhibition) and were all rescued by uridine (rU) supplementation (**Figure S2**)(Hafner, Niepel, Chung, & Sorger, 2016). MIAPACA2 PDAC cells were utilized in the screen due to their ability to maintain baseline proliferation levels in NSP-only or DNP-only conditions, while also exhibiting a significant decrease in proliferation upon simultaneous NSP and DNP inhibition (**Figure S3A**).

A library of 430 protein kinase inhibitors was chosen for evaluation, the rationale being twofold. First, we hypothesized that our synthetic lethality screen may identify compounds that indirectly target pyrimidine metabolism by inhibiting regulatory signal transduction pathways. Second, because the majority of kinase inhibitors are ATP-mimetics, and given their resemblance to nucleotides, we predicted that protein kinase inhibitors may posses additional, non-canonical targets within nucleotide metabolism. Consistently, several protein kinase inhibitors, specifically those exhibiting similarities with the phenylamino pyrimidine (PAP) imatinib scaffold, and a subset of p38 MAPK inhibitors, exhibit activity against nucleoside transporters(Damaraju, Weber, Kuzma, Cass, & Sawyer, 2016; Huang et al., 2002). The library was screened at 7-point dose response in duplicate. Composite NSP and DNP pathway selectivity scores were calculated for each compound as the sum of condition-specific anti-proliferative effects across the dose range (**Figure S3B**). Assay quality was monitored using the Z-factor metric (**Figure S3C**)(Ji-Hu Zhang, Kevin R. Oldenburg, 1999).

The JNK inhibitor JNK-IN-8, the BTK inhibitor CNX-774, and the VEGFR inhibitor AMG-706 were active in the NSP-only condition (**Figure 1B**). The selectivity of these hits was unique among inhibitors of JNK (**Figure 1C**), BTK, and VEGFR (**Figures S3D-S3F**), indicating this phenotype likely did not result from on-target effects.

The PDK1 inhibitor OSU-03012 (also known as AR-12) and the pan-RAF inhibitor TAK-632 were identified as eliciting potent and selective inhibition of proliferation in the DNP-only condition (**Figure 1D**)(Zhu et al., 2004; Okaniwa et al., 2013). Among the four PDK1 inhibitors and 14 RAF inhibitors tested, OSU-03012 and TAK-632 were unique in their ability to selectively inhibit the DNP, suggesting that their ability to inhibit the pyrimidine DNP was not the consequence of on-target effects (**Figures 1E-1F**). Hit selectivity was confirmed using an orthogonal long-term proliferation inhibition assay (**Figure S3G**).

JNK-IN-8 inhibits nucleoside uptake *in vitro* and *in vivo*

While three protein kinase inhibitors were identified as selective inhibitors of the pyrimidine NSP, JNK-IN-8 was exceptionally so. We reasoned that the activity of JNK-IN-8 could arise from either the inhibition of nucleoside shuttling across the plasma membrane, achieved by concentrative (CNT) or equilibrative (ENT) nucleoside transporters, or of UCKs. To determine the level at which JNK-IN-8 is active, the uptake of tritiated rU and dC was quantified. These nucleosides rely upon the same transporters to enter the cell but require unique kinases for conversion into their respective monophosphate forms and resultant intracellular accumulation

(**Figure 2A**). The assay revealed that JNK-IN-8 inhibited the uptake of rU and dC with similar potency (33 nM and 31 nM, respectively), suggesting that the compound was inhibiting nucleoside transport (**Figure 2B**). Additionally, JNK-IN-8 treatment rescued JURKAT cells from the anti-proliferative effects of gemcitabine, a dCK-dependent nucleoside analog prodrug which relies upon nucleoside transporters to enter the cell, with an EC_{50} of 15.2 nM (**Figure S4A, S4B**).

After demonstrating the ability of JNK-IN-8 to inhibit the pyrimidine NSP *in vitro*, we assessed its ability to block accumulation of a dCK-specific nucleoside analog PET probe, ^{18}F-clofarabine ([^{18}F]CFA), in CCRF-CEM xenograft tumors formed in NSG mice(Kim et al., 2016). Following treatment, PET imaging revealed that tumor [^{18}F]CFA PET uptake was decreased in JNK-IN-8-treated mice, relative to vehicle-treated controls (**Figure 2C-2D**).

Identification *de novo* UMP biosynthesis target of OSU-03012 and TAK-632

Two kinase inhibitors, TAK-632 and OSU-03012, were identified as potent and selective inhibitors of the DNP (**Figure S4C**). We reasoned that these compounds could target either CAD, DHODH, or UMPS enzymes in *de novo* pyrimidine biosynthesis (**Figure 3A**). Both compounds induced S-phase arrest in MIAPACA2 cells, a phenotype associated with insufficient dNTP biosynthesis to sustain DNA replication and activation of intra-S phase signaling checkpoints. This effect was rescued by orotate (the product of DHODH) supplementation and could be completely reversed by rU supplementation (**Figures 3B-3C**). DHODH inhibition emerged as a likely mechanism, as it catalyzes one of three committed steps within the DNP and is a druggable protein (Madak et al., 2019). Additionally, both OSU-03012 and TAK-632 posses fluorine substituents which have been shown to stabilize bioactive conformations of DHODH inhibitors (Bonomo, Tosco, Giorgis, Lolli, & Fruttero, 2013; Baumgartner et al., 2006). In an *in vitro* colorimetric recombinant human DHODH activity assay, TAK-632 and OSU-03012 both inhibited DHODH activity in a dose-dependent manner (**Figure 3D**) (Baumgartner et al., 2006). In screening a panel of 23 PDAC cell lines we found the sensitivity to OSU-03012 to be heterogenous (**Figure S6A**). Importantly, the response to TAK-632 or OSU-03012 correlated with the response to a known DHODH inhibitor in this cell line panel (**Figure 3E**).

To determine the molecular interactions between the protein and its putative inhibitors, complete DHODH co-crystallization data sets were obtained and processed to 1.4 Å and 2.7 Å for OSU-03012 and TAK-632, respectively (**Figure S5a**). Both compounds bind in a hydrophobic channel composed by two N-domain α-helices through which ubiquinone travels, consistent with previously identified DHODH inhibitors (Baumgartner et al., 2006). A long-range hydrogen bond between Arg 69 and OSU-03012 helps orient the molecule to the hydrophobic pocket where the phenanthrene moiety inserts, while the remainder of the molecule lays on the outer surface of DHODH, blocking the hydrophobic channel (**Figures 4A, S5B**). Three hydrogen bonds stabilize TAK-632 in the same hydrophobic pocket: two with Tyr 37 and Leu 66 help stabilize the inhibitor at the opening of the channel, while a third with Gln 46 helps pull the inhibitor deep into the pocket (**Figures 4B, S5C**).

OSU-03012 synergizes with replication stress response inhibitors to induce cancer cell death

OSU-03012 was recently reported to synergize with replication stress response kinase inhibitors in RSK-subtype mutant KRAS cancer models(Yuan et al., 2018). However, after confirming that OSU-03012 binds DHODH, we hypothesized that the observed synergy resulted from DHODH inhibition rather than PDK1 inhibition. We treated MIAPACA2 cells with M6620, an inhibitor of the proximal replication stress response kinase ATR, and either OSU-03012 or the PDK1 inhibitor GSK-2334470 for 72 h. We observed a synergistic increase in cell death when OSU-03012 and an ATR inhibitor were combined, whereas the combination of GSK-2334470 and M6620 demonstrated only a nominal increase in cell death (**Figure S6B**). Immunoblot analysis of S6K and S6 phosphorylation, PDK1 downstream targets, confirmed that GSK-2334470 potently blocked PDK1 while OSU-03012 triggered CHEK1 phosphorylation, a replication stress biomarker, only in the absence of rU (**Figure S6C**). Taken together, these data indicate that replication stress triggered by OSU-03012 is the consequence of DHODH inhibition rather than inhibition of its canonical target.

DISCUSSION

Our screening strategy expands on previous “nutrient-sensitized” genetic and small molecule screens, the general design of which can be applied to any number of metabolic systems, so long as said system produces a critical metabolite through parallel and redundant biosynthetic pathways(Arroyo et al., 2016; Gohil et al., 2010). UMP biosynthesis (i.e. pyrimidine metabolism) was identified as an amenable extension for this type of screen, as it consists of convergent pathways, and UMP depletion triggers a quantifiable change in phenotype.

JNK-IN-8, developed as an irreversible inhibitor of c-Jun N-terminal kinases 1, 2, and 3 with low-nanomolar affinity, was the most potent of three NSP inhibitors identified(Zhang et al., 2012). Our data show that it is additionally a potent inhibitor of nucleoside transport, both *in vitro* and *in vivo*. We conclude that JNK-IN-8 should not be used in conjunction with compounds, including cancer-treating antimetabolites, which rely upon nucleoside transport for their research or therapeutic purpose. Furthermore, JNK-IN-8 should not be used in research settings wherein upregulation of the pyrimidine DNP may confound experimental results.

The structurally and functionally unrelated OSU-03012 and TAK-632 were identified as inhibitors of the pyrimidine DNP. A recent report described the ability of OSU-03012 and analogs to inhibit virus propagation *via* pyrimidine nucleotide biosynthesis inhibition, specifically implicating DHODH (Yang et al., 2018). Our work substantiates these findings, is the first to unambiguously confirm the affinity of OSU-03012 for DHODH through crystallography studies, and the first to demonstrate the same for TAK-632. Notably, our studies show that OSU-03012 and TAK-632 bind in the same hydrophobic tunnel of DHODH as known inhibitors brequinar and teriflunomide (active metabolite of leflunomide). This suggests that these two protein kinase inhibitors compete with ubiquinone, a redox partner of DHODH which traverses the hydrophobic tunnel to regenerate FMN from $FMNH_2$. By competitively inhibiting the binding of ubiquinone, these compounds prevent DHODH from completing its redox cycle which effectively abrogates its activity.

OSU-03012 has orphan drug designation in the European Union for treatment of tularaemia and cryptococcosis. We hypothesize that its effectiveness in these indications stems from its ability to inhibit DHODH, rather than from ‘on-target’ effects against PDK1. Indeed, DHODH inhibitors have demonstrated efficacy against viruses such as dengue virus and respiratory syncytial virus (Bonavia et al., 2011; Yang et al., 2018; Wang et al., 2011). In anticancer settings, OSU-03012 was recently demonstrated to synergize with CHK1 inhibitors in KRAS-mutant cancers (Yuan et

al., 2018), which was initially attributed to its ability to inhibit PDK1. However, our data show that GSK-2334470, a PDK1 inhibitor more potent than OSU-03012, displayed markedly little synergy with ATR inhibition. In light of our crystallographic data, we conclude that the synergy observed between OSU-03012 and ATR inhibition is likely a result of the DHODH-inhibitory ability of the former. Taken together, our data suggest that DHODH inhibitors have utility in oncology, particularly if used in conjunction with ATR inhibitors or other DNA-damage response/replication stress response pathway inhibitors(Le et al., 2017).

In summary, we designed and applied a metabolic modifier screen which identified multiple protein kinase inhibitors as having non-canonical targets within pyrimidine metabolism. Similarly constructed phenotypic screens designed against other metabolic networks containing convergent nodes may find use in drug discovery campaigns or in repurposing screens using existing compounds.

FIGURES

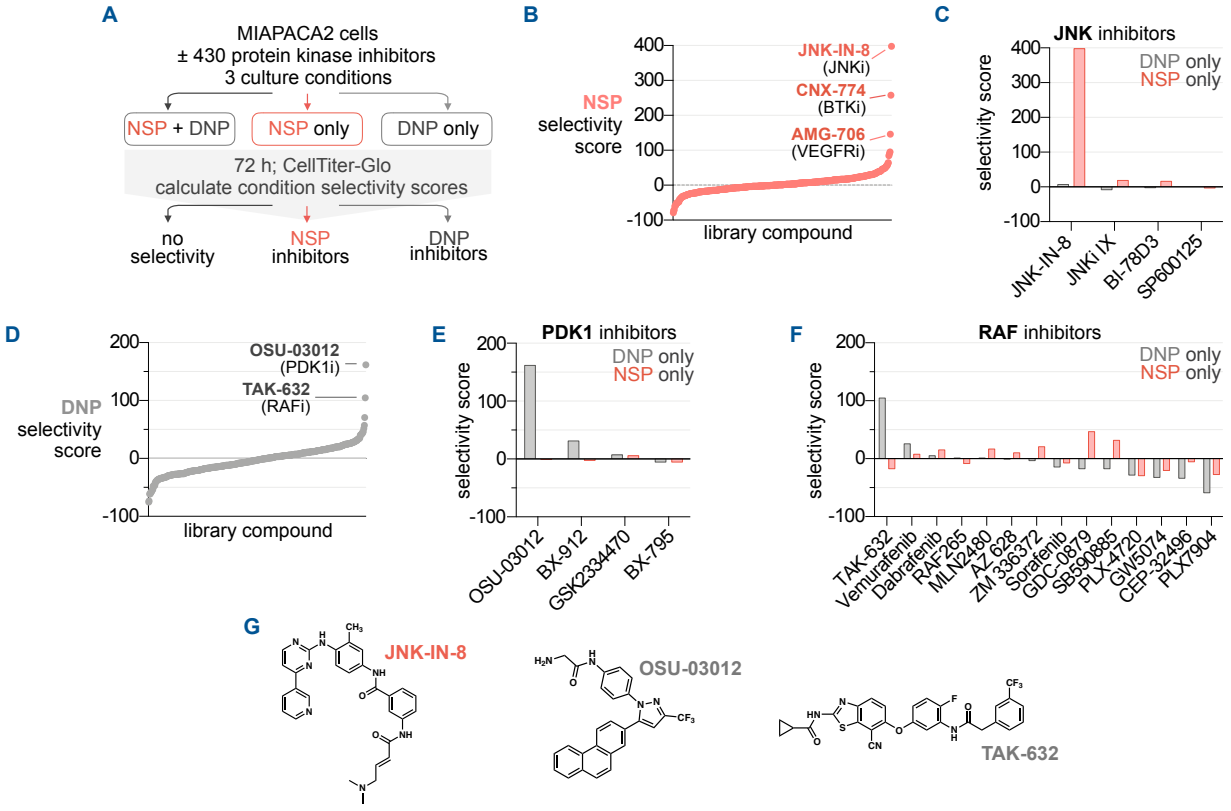

Fig. 4.1 | Identification of UMP-DNP and -NSP modulators in a small molecule protein kinase inhibitor library. (**A**) Phenotypic screening strategy. The impact of 430 protein kinase inhibitors on cell proliferation was evaluated in MIAPACA2 cells plated in 3 distinct growth conditions; 1) NSP + DNP (media + 10 μM uridine (rU)); 2) NSP only (media + 10 μM rU + 1 μM NITD-982); or 3) DNP only (media alone). % proliferation values were calculated using CellTiter-Glo (CTG) following 72 h treatment (7-point dose response; n=2). (**B, C**) Waterfall plots ranking library compounds based on NSP (**B**) or DNP (**C**) pathway selectivity scores determined as described in **Fig. S3B**. (**D-F**) Summary of NSP and DNP selectivity scores across library compounds annotated as JNK (**D**), PDK1 inhibitors (**E**), or RAF inhibitors (**F**). (**G**) Structures of hit compounds.

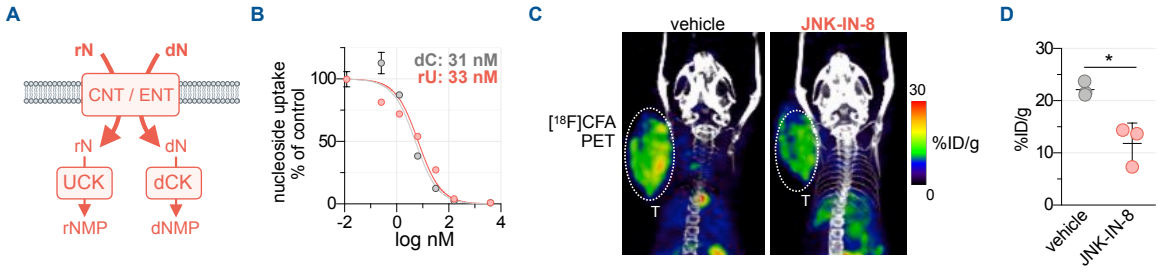

Fig. 4.2 | JNK-IN-8 inhibits nucleoside transport *in vitro* and *in vivo*. (**A**) Nucleoside uptake can be prevented by inhibition of either nucleoside transporters or kinases. (**B**) Uptake of ^{3}H-rU or ^{3}H-dC in CCRF-CEM cells following 2 h incubation ± JNK-IN-8 (mean±SD; n=2). IC_{50} values are indicated. (**C**) Representative PET/CT scans of CCRF-CEM subcutaneous tumor bearing NSG mice imaged with [^{18}F]CFA X h after treatment with vehicle (n=2) or JNK-IN-8 (50 mg/kg; n=3) T, tumor. (**D**) Quantification of [^{18}F]CFA tumor uptake in **C** (%ID/g: percentage injected dose per gram; mean±SD; student t-test, * P<0.05).

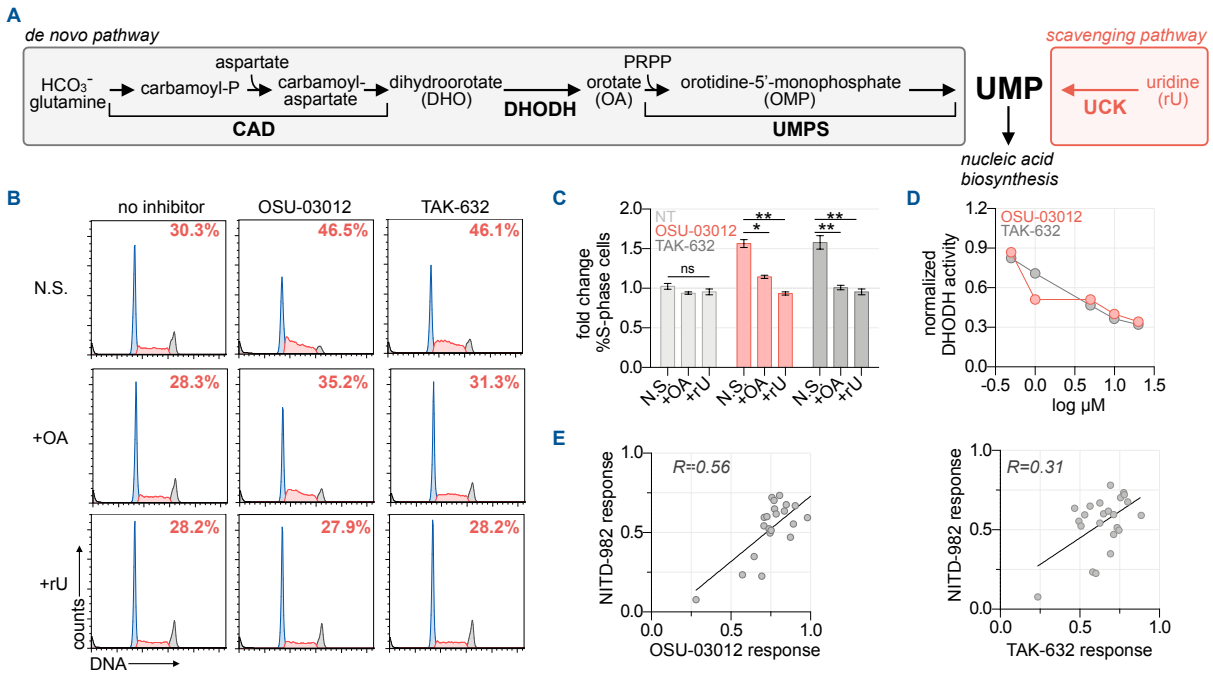

Fig. 4.3 | OSU-03012 and TAK-632 inhibit DHODH. (**A**) Summary of UMP biosynthesis. (**B**) Propidium iodide cell cycle analysis of MIAPACA2 PDAC cells treated ± 5 µM TAK-632; 5 µM OSU-03012 supplemented with 50 µM orotate (OA) or 10 µM rU (N.S.: no supplement). Insert indicates % S-phase cells. (**C**) Summary of fold changes in S-phase cells from experiment in (mean±SD; n=2; one-way ANOVA corrected for multiple comparisons by Bonferroni adjustment, ns: not significant; * P<0.05; ** P<0.01). (**D**) *in vitro* DHODH enzyme assay performed in the presence of OSU-03012 or TAK-632. (**E**) Correlation between DHODHi (1 µM NITD-982) and OSU-03012 (3.12 µM) or TAK-632 (3.12 µM) response across a panel of 27 PDAC cell lines determined using CTG following 72 h of treatment. Response calculated as doubling time normalized proliferation inhibition. Pearson correlation coefficient is indicated.

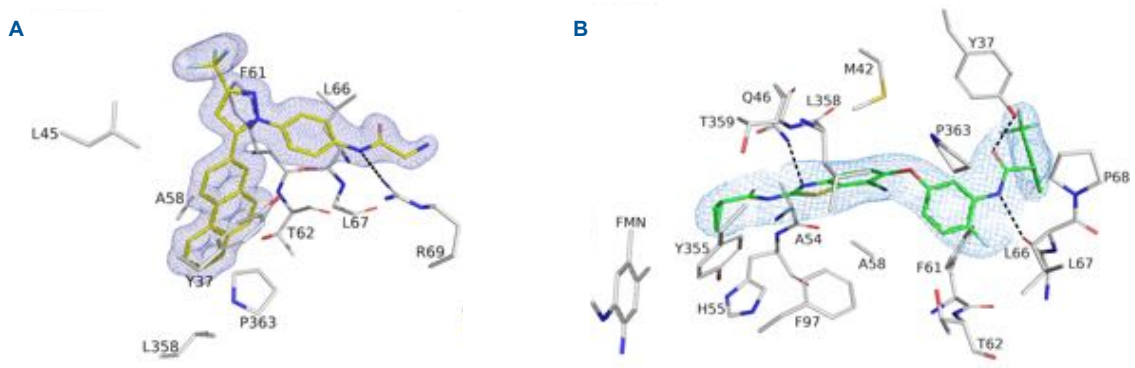

Fig. 4.4 | OSU-03012 and TAK-632 bind DHODH. (**A,B**) Crystal Structure of DHODH with OSU-03012 (**A**) or TAK-632 (**B**). 2mFo-DFc electron density for OSU-03012 (carbons in yellow) or TAK-632 (carbons in green) contoured at 1 σ. Dashed black lines represent hydrogen bonds between the ligands and DHODH. Interacting residues as predicted by LigPlot+ are shown and labeled.

Supplementary Figures

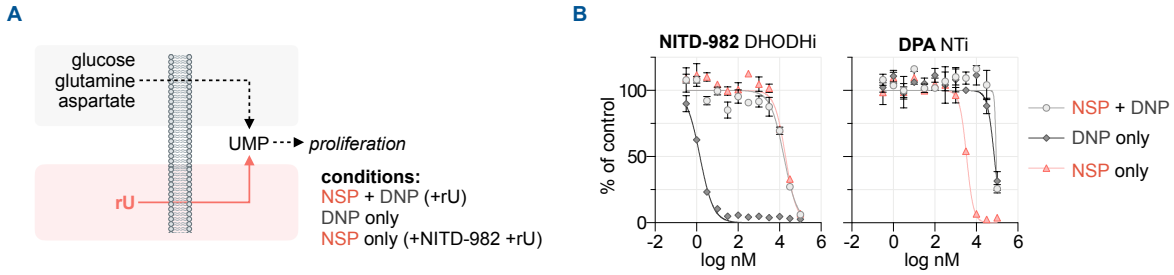

Fig. S4.1 | Validation of UMP as a critical, convergent metabolic node in cancer cells. (**A**) UMP can be produced by a *de novo* pathway (DNP) from glucose, glutamine, bicarbonate and aspartate or from extracellular uridine (rU) by a nucleoside transporter and kinase-dependent salvage pathway (NSP). (**B**) Dose response curves of DHODH inhibitor NITD-982 and nucleoside transport inhibitor dipyridamole (DPA) in JURKAT cells cultured in NSP + DNP (media + 10 μM rU), NSP only (media + 10 μM rU + 1 μM NITD-982), or DNP only (media alone) for 72 h as determined by CellTiter-Glo (CTG; mean±SD; n=4).

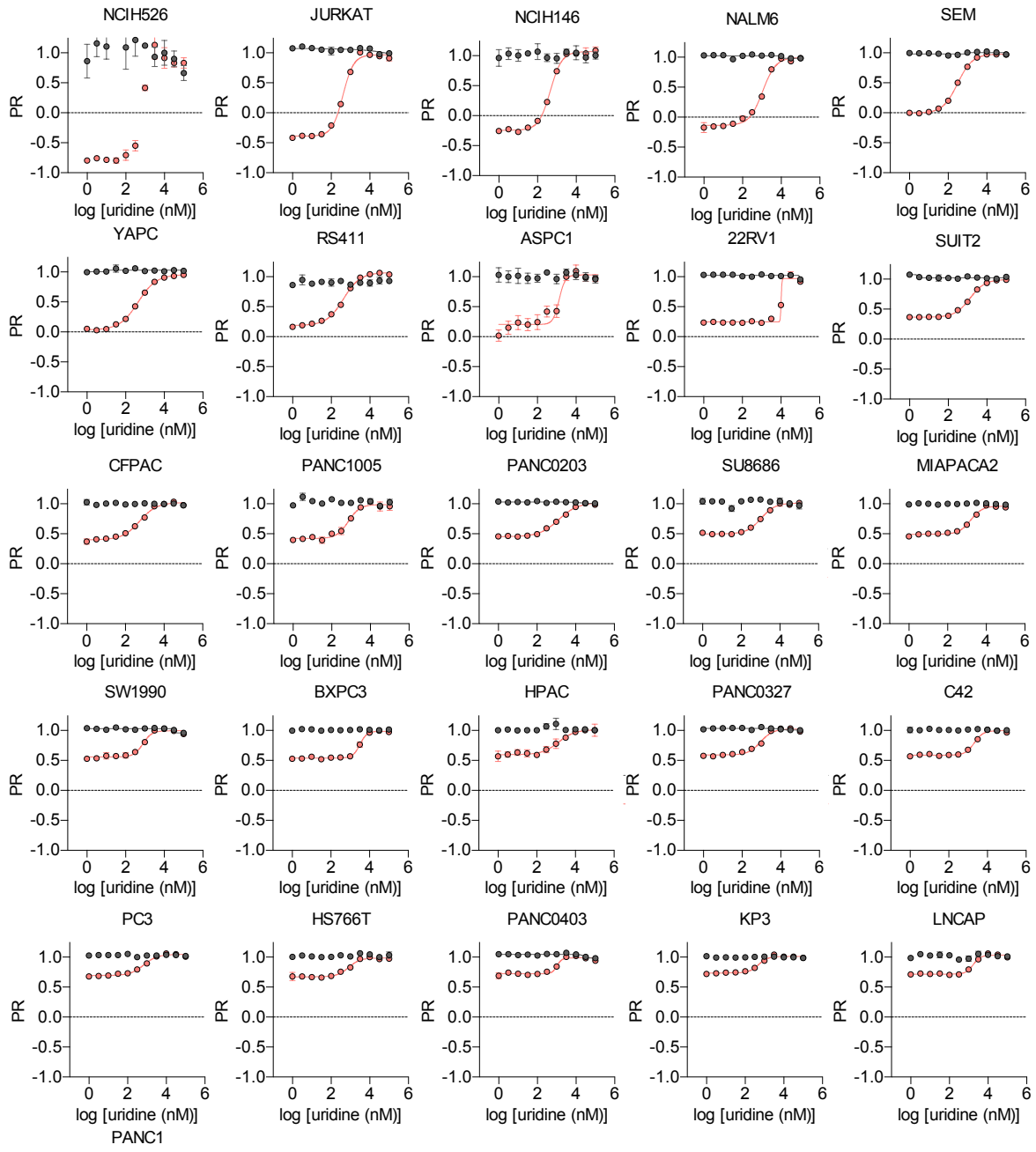

Fig. S4.2 | UMP-DNP and NSP are interchangeable in sustaining proliferation across a panel of cancer cell lines. Uridine titration in cancer cell lines cultured in media + 10% dFBS ±1 μM NITD-982 (n=4). Relative proliferation rate (PR) was calculated by normalizing % proliferation values at 72 h to cell line proliferation rate. Proliferation rates were calculated utilizing CTG measurements at the time of treatment (t0) and vehicle-treated controls at 72 h.

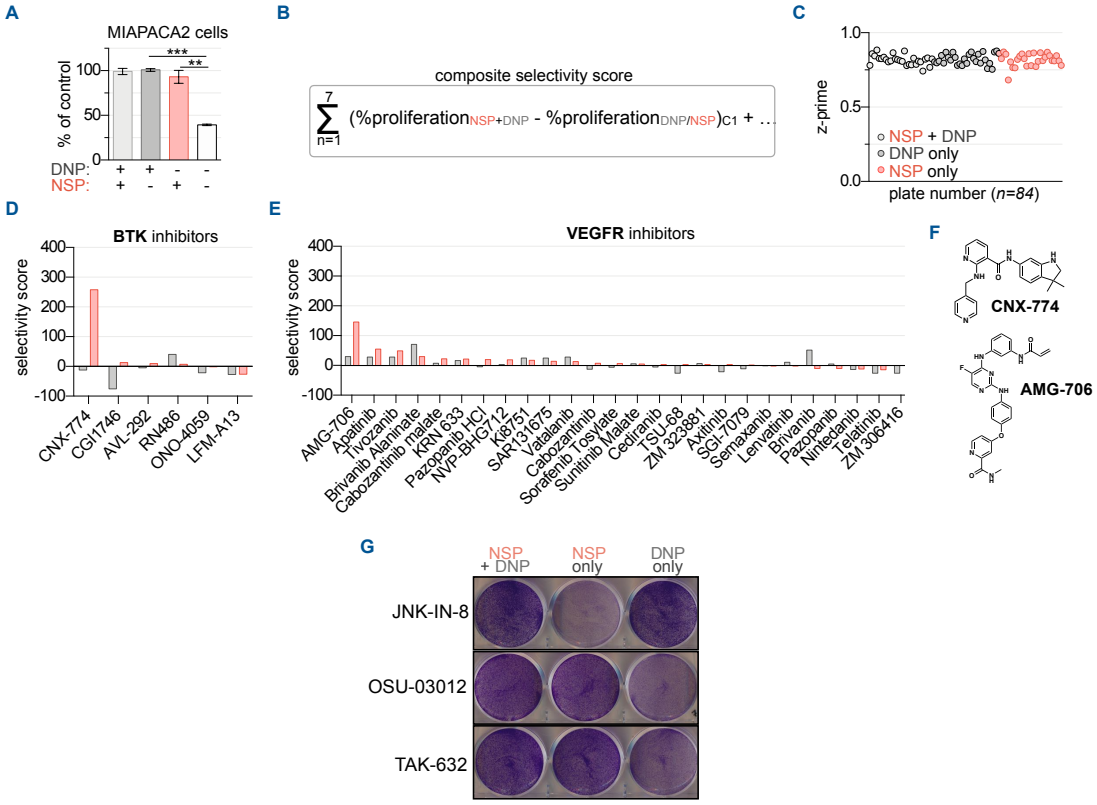

Fig. S4.3 | Phenotypic screen identifies UMP-NSP and -DNP inhibitors. (**A**) CTG analysis of MIAPACA2 cells cultured in NSP+DNP (media +10 μM rU), DNP (media alone), NSP (media +10 μM rU +1 μM NITD-982) or starvation conditions (media + 1 μM NITD-982) for 72 h (mean±SD; n=4; one-way ANOVA corrected for multiple comparisons by Bonferroni adjustment, ** P < 0.01; *** P < 0.001) (**B**) Methodology applied to determine UMP-DNP and -NSP selectivity scores (n=2). (**C**) Z'-scores calculated for individual assay plates from experiment in **Figure 1**. (**D**) Selectivity scores for BTK inhibitors included in the screen. (**E**) Selectivity scores for VEGFR inhibitors included in the screen. (**F**) Structures of hit compounds. (**G**) Validation of hit compounds using 7 d crystal violet proliferation assay. MIAPACA2 cells were treated with 1 μM JNK-IN-8, 1 μM OSU-03012, 1 μM TAK-632 in NSP+DNP, DNP or NSP conditions.

A

	JNK-IN-8	CNX-774	AMG-706
NSP+DNP IC_{50}	3090 nM	1700 nM	12441 nM
DNP IC_{50}	2990 nM	2270 nM	10381 nM
NSP IC_{50}	12.86 nM	76.7 nM	134 nM
dFdC EC_{50}	15.16 nM	36.2 nM	75.4 nM

B

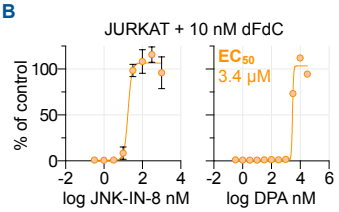

C

	OSU-03012	TAK-632
NSP+DNP IC_{50}	3829 nM	2346 nM
DNP IC_{50}	390.7 nM	579.8 nM
NSP IC_{50}	3426 nM	1978 nM

Fig. S4.4 | Evaluation of UMP-NSP and -DNP inhibitor potency and selectivity. (**A**) Calculation of JNK-IN-8, CNX-774, and AMG-706 IC50 values for JURKAT cells cultured in NSP+DNP, DNP-only, and NSP-only conditions, and EC50 values for gemcitabine (dFdC) rescue. (**B**) JNK-IN-8 and DPA dose response in JURKAT cells treated with 10 nM dFdC (n=4; mean±SD) for 72 h determined using CTG. (**C**) Calculation of OSU-03012 and TAK-632 IC50 in JURKAT cells treated for 72 h determined using CTG.

A

Structure	*DHODH + OSU-03012*	*DHODH + TAK-632*
PDB codes	6OC0	6OC1
Data collection statistics		
X-ray source and detector	LS-CAT 21-ID-D Dectris Eiger x 9M	LS-CAT 21-ID-G MARCCD 300
Wavelength (Å)	0.99987	0.97872
Temperature (K)	100	100
Resolution[a] (Å)	1.40 (1.48-1.40)	2.7 (2.85-2.7)
Number of Reflections		
Observed	1,090,019 (113,565)	306,440 (48,502)
Unique	114,363 (17,418)	13,751 (2,169)
Completeness (%)	99.0 (94.2)	99.9 (99.8)
R_{meas} (%)	7.0 (54.5)	17.0 (183.3)
$CC_{1/2}$ (%)	99.9 (87.8)	99.9 (71.1)
Average I/σ(I)	19.2 (2.8)	21.6 (2.1)
Space group	P 3_2 2 1	P 2_1 3
Unit cell: a, b, c (Å)	90.01, 90.01, 123.07	113.67, 113.67, 113.67
Unit cell: α, β, γ (°)	90, 90, 120	90, 90, 90
Wilson B-factors (Å·)	13.9	66.4
Refinement statistics		
Refinement program	REFMAC5	REFMAC5
R_{work} (%)	15.7	23.4
R_{free} (%)	19.1	29.1
Resolution range (Å)	48.55-1.40	46.45-2.70
Protein molecules per a.u.	1	1
Number of atoms:		
Protein	2845	2769
Water molecules	232	36
ORO + FMN	42	42
Inhibitor	34	39
R.m.s. deviation from ideal:		
Bond length (Å)	0.009	0.0021
Bond angles (°)	1.7114	1.264
Average B-factors (Å·)		
Protein	23.9	73.0
Water molecules	32.6	44.7
ORO + FMN	12.2	56.6
Inhibitor	29.3	73.0
Ramachandran plot statistics (%)		
Most favored regions	97	86
Additionally allowed regions	3	14
Outlier regions	0	1

B

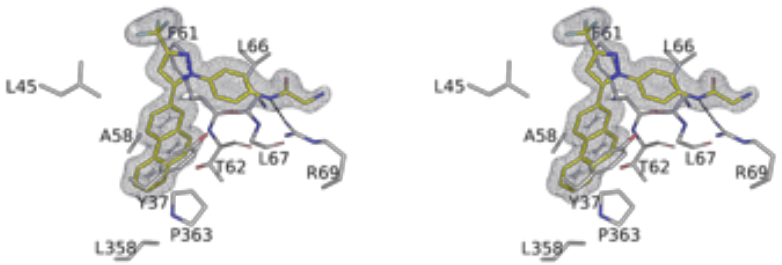

C

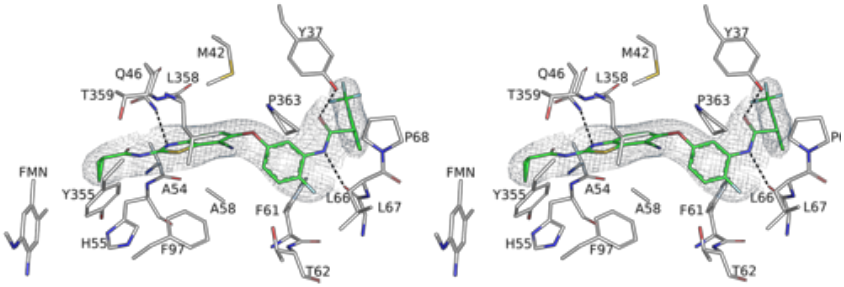

Fig. S4.5 | Evaluation of DHODH / inhibitor interactions. (**A**) Stereoscopic image of Figure **4A** (OSU-03012). (**B**) Stereoscopic image of Figure 4B (TAK-632).(C) Crystallographic data collection and refinement statistics. [a]High resolution shell in parenthesis; r.m.s., root- mean-square; a.u., asymmetric unit

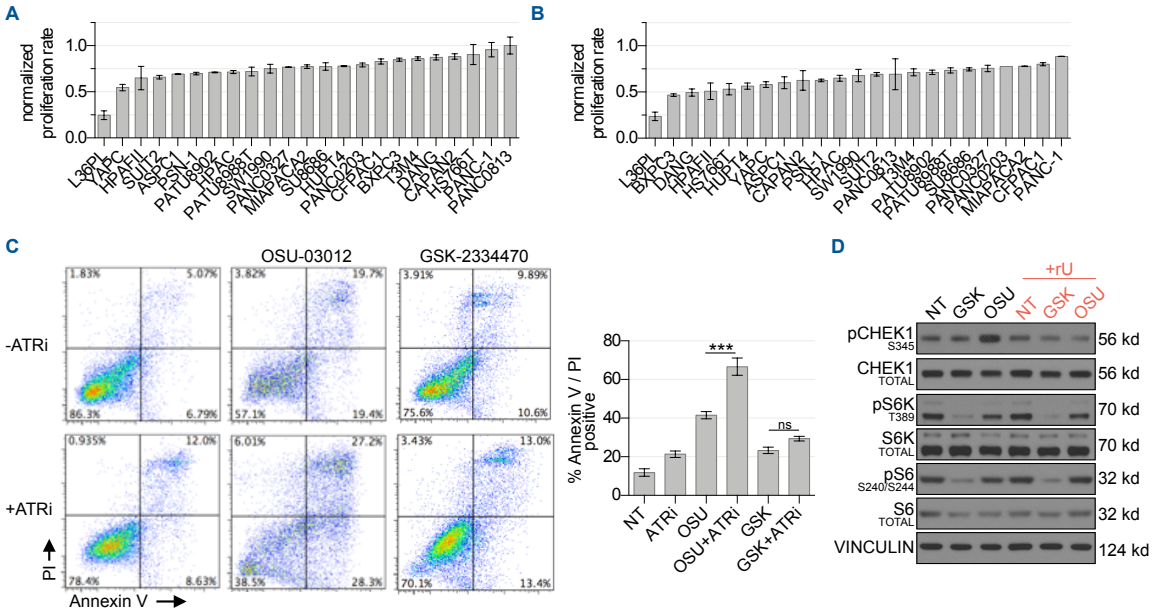

Fig. S4.6 | AnnexinV/PI flow cytometry analysis of OSU-03012 / ATRi combination.
Representative flow cytometry plots from experiment in **Figure 3H**.

REFERENCES

1. An R. Van Rompay, A. N., Karin Linden, Magnus Johansson, Anna Karlsson. (2001). Phosphorylation of Uridine and Cytidine Nucleoside Analogs by Two Human Uridine-Cytidine Kinases. *Molecular Pharmacology*, *59*(5), 1181-1186.

2. Arroyo, J. D., Jourdain, A. A., Calvo, S. E., Ballarano, C. A., Doench, J. G., Root, D. E. et al. (2016). A Genome-wide CRISPR Death Screen Identifies Genes Essential for Oxidative Phosphorylation. *Cell Metabolism*, *24*(6), 875-885.

3. Baumgartner, R., Walloschek, M., Kralik, M., Gotschlich, A., Tasler, S., Mies, J. et al. (2006). Dual binding mode of a novel series of DHODH inhibitors. *J Med Chem*, *49*(4), 1239-1247.

4. Bonavia, A., Franti, M., Pusateri Keaney, E., Kuhen, K., Seepersaud, M., Radetich, B., Shao, J., Honda, A., Dewhurst, J., Balabanis, K., Monroe, J., Wolff, K., Osborne, C., Lanieri, L., Hoffmaster, K., Amin, J., Markovits, J., Broome, M., Skuba, E., Cornella-Taracido, I., Joberty, G., Bouwmeester, T., Hamann, L., Tallarico, J. A., Tommasi, R., Compton, T., Bushell, S. M. (2011). Identification of broad-spectrum antiviral compounds and assessment of the druggability of their target forefficacy against respiratory syncytial virus (RSV). *Proc Natl Acad Sci USA*, *108*(17), 6739-6744.

5. Bonomo, S., Tosco, P., Giorgis, M., Lolli, M., & Fruttero, R. (2013). The role of fluorine in stabilizing the bioactive conformation of dihydroorotate dehydrogenase inhibitors. *J Mol Model*, *19*(3), 1099-1107.

6. Campbell, D. O., Yaghoubi, S. S., Su, Y., Lee, J. T., Auerbach, M. S., Herschman, H. et al. (2011). Structure-guided Engineering of Human Thymidine Kinase 2 as a Positron Emission Tomography Reporter Gene for Enhanced Phosphorylation of Non-natural Thymidine Analog Reporter Probe. *J. Biol. Chem.*, *287*(1), 446-454.

7. Damaraju, V. L., Weber, D., Kuzma, M., Cass, C. E., & Sawyer, M. B. (2016). Selective Inhibition of Human Equilibrative and Concentrative Nucleoside Transporters by BCR-ABL Kinase Inhibitors: Identification of Key hENT1 Amino Acid Residues for Interaction with BCR-ABL Kinase Inhibitors. *J Biol Chem*, *291*(36), 18809-18817.

8. Das, P., Deng, X., Zhang, L., Roth, M. G., Fontoura, B. M., Phillips, M. A. et al. (2013). SAR Based Optimization of a 4-Quinoline Carboxylic Acid Analog with Potent Anti-Viral Activity. *ACS Med Chem Lett*, *4*(6), 517-521.

9. Davies, M., Heikkilä, T., McConkey, G. A., Fishwick, C. W., Parsons, M. R., & Johnson, A. P. (2009). Structure-based design, synthesis, and characterization of inhibitors of human and Plasmodium falciparum dihydroorotate dehydrogenases. *J Med Chem*, *52*(9), 2683-2693.

10. Deng, X., Kokkonda, S., El Mazouni, F., White, J., Burrows, J. N., Kaminsky, W. et al. (2014). Fluorine modulates species selectivity in the triazolopyrimidine class of Plasmodium falciparum dihydroorotate dehydrogenase inhibitors. *J Med Chem*, *57*(12), 5381-5394.

11. Erra, M., Moreno, I., Sanahuja, J., Andrés, M., Reinoso, R. F., Lozoya, E. et al. (2011). Biaryl analogues of teriflunomide as potent DHODH inhibitors. *Bioorg Med Chem Lett*, *21*(24), 7268-7272.

12. Garcia-Bermudez, J., Baudrier, L., La, K., Zhu, X. G., Fidelin, J., Sviderskiy, V. O. et al. (2018). Aspartate is a limiting metabolite for cancer cell proliferation under hypoxia and in tumours. *Nat Cell Biol*, *20*(7), 775-781.

13. Gohil, V. M., Sheth, S. A., Nilsson, R., Wojtovich, A. P., Lee, J. H., Perocchi, F. et al. (2010). Nutrient-sensitized screening for drugs that shift energy metabolism from mitochondrial respiration to glycolysis. *Nat Biotechnol*, *28*(3), 249-255.

14. Hafner, M., Niepel, M., Chung, M., & Sorger, P. K. (2016). Growth rate inhibition metrics correct for confounders in measuring sensitivity to cancer drugs. *Nat Methods*, *13*(6), 521-527.

15. Huang, M., Wang, Y., Collins, M., Gu, J. J., Mitchell, B. S., & Graves, L. M. (2002). Inhibition of Nucleoside Transport by p38 MAPK Inhibitors. *J. Biol. Chem.*, *277*(32), 28364-28367.

16. Hurt, D. E., Sutton, A. E., & Clardy, J. (2006). Brequinar derivatives and species-specific drug design for dihydroorotate dehydrogenase. *Bioorg Med Chem Lett*, *16*(6), 1610-1615.

17. Ji-Hu Zhang, T. D. Y. C., Kevin R. Oldenburg. (1999). A Simple Statistical Paramter for Use in Evaluation and Validation of High Throughput Screening Assays. *Journal of Biomolecular Screening*, *4*(2), 67-73.

18. Kim, W., Le, T. M., Wei, L., Poddar, S., Bazzy, J., Wang, X. et al. (2016). [F]CFA as a clinically translatable probe for PET imaging of deoxycytidine kinase activity. *Proc Natl Acad Sci USA*, *113*(15), 4027-4032.

19. Ladds, M. J. G. W., van Leeuwen, I. M. M., Drummond, C. J., Chu, S., Healy, A. R., Popova, G. et al. (2018). Publisher Correction: A DHODH inhibitor increases p53 synthesis and enhances tumor cell killing by p53 degradation blockage. *Nat Commun*, *9*(1), 2071.

20. Laskowski, R. A., & Swindells, M. B. (2011). LigPlot+: multiple ligand-protein interaction diagrams for drug discovery. *J Chem Inf Model*, *51*(10), 2778-2786.

21. Le, T. M., Poddar, S., Capri, J. R., Abt, E. R., Kim, W., Wei, L. et al. (2017). ATR inhibition facilitates targeting of leukemia dependence on convergent nucleotide biosynthetic pathways. *Nat Commun*, *8*(1), 241.

22. Lewis, T. A., Sykes, D. B., Law, J. M., Muñoz, B., Rustiguel, J. K., Nonato, M. C. et al. (2016). Development of ML390: A Human DHODH Inhibitor That Induces Differentiation in Acute Myeloid Leukemia. *ACS Med Chem Lett*, *7*(12), 1112-1117.

23. Liu, S., Neidhardt, E. A., Grossman, T. H., Ocain, T., & Clardy, J. (2000). Structures of human dihydroorotate dehydrogenase in complex with antiproliferative agents. *Structure*, *8*(1), 25-33.

24. Lolli, M. L., Sainas, S., Pippione, A. C., Giorgis, M., Boschi, D., & Dosio, F. (2018). Use of human Dihydroorotate Dehydrogenase (hDHODH) Inhibitors in Autoimmune Diseases and New Perspectives in Cancer Therapy. *Recent Pat Anticancer Drug Discov*, *13*(1), 86-105.

25. Madak, J. T., Bankhead, A., Cuthbertson, C. R., Showalter, H. D., & Neamati, N. (2019). Revisiting the role of dihydroorotate dehydrogenase as a therapeutic target for cancer. *Pharmacology & Therapeutics*, *195*, 111-131.

26. McLean, L. R., Zhang, Y., Degnen, W., Peppard, J., Cabel, D., Zou, C. et al. (2010). Discovery of novel inhibitors for DHODH via virtual screening and X-ray crystallographic structures. *Bioorg Med Chem Lett*, *20*(6), 1981-1984.

27. Okaniwa, M., Hirose, M., Arita, T., Yabuki, M., Nakamura, A., Takagi, T. et al. (2013). Discovery of a selective kinase inhibitor (TAK-632) targeting pan-RAF inhibition: design, synthesis, and biological evaluation of C-7-substituted 1,3-benzothiazole derivatives. *J Med Chem*, *56*(16), 6478-6494.

28. Okesli, A., Khosla, C., & Bassik, M. C. (2017). Human pyrimidine nucleotide biosynthesis as a target for antiviral chemotherapy. *Current Opinion in Biotechnology*, *48*, 127-134.

29. Sainas, S., Pippione, A. C., Lupino, E., Giorgis, M., Circosta, P., Gaidano, V. et al. (2018). Targeting Myeloid Differentiation Using Potent 2-Hydroxypyrazolo[1,5- a]pyridine Scaffold-Based Human Dihydroorotate Dehydrogenase Inhibitors. *J Med Chem*, *61*(14), 6034-6055.

30. Santana-Codina, N., Roeth, A. A., Zhang, Y., Yang, A., Mashadova, O., Asara, J. M. et al. (2018). Oncogenic KRAS supports pancreatic cancer through regulation of nucleotide synthesis. *Nat Commun*, *9*(1), 4945.

31. Shu, C. J., Campbell, D. O., Lee, J. T., Tran, A. Q., Wengrod, J. C., Witte, O. N. et al. (2010). Novel PET probes specific for deoxycytidine kinase. *J Nucl Med*, *51*(7), 1092-1098.

32. Sykes, D. B., Kfoury, Y. S., Mercier, F. E., Wawer, M. J., Law, J. M., Haynes, M. K. et al. (2016). Inhibition of Dihydroorotate Dehydrogenase Overcomes Differentiation Blockade in Acute Myeloid Leukemia. *Cell*, *167*(1), 171-186.e15.

33. Wallace, A. C., Laskowski, R. A., & Thornton, J. M. (1995). LIGPLOT: a program to generate schematic diagrams of protein-ligand interactions. *Protein Eng*, *8*(2), 127-134.

34. Walse, B., Dufe, V. T., Svensson, B., Fritzson, I., Dahlberg, L., Khairoullina, A. et al. (2008). The structures of human dihydroorotate dehydrogenase with and without inhibitor reveal conformational flexibility in the inhibitor and substrate binding sites. *Biochemistry*, *47*(34), 8929-8936.

35. Wang, Q. Y., Bushell, S., Qing, M., Xu, H. Y., Bonavia, A., Nunes, S. et al. (2011). Inhibition of dengue virus through suppression of host pyrimidine biosynthesis. *J Virol*, *85*(13), 6548-6556.

36. Xu, S., Catapang, A., Doh, H. M., Bayley, N. A., Lee, J. T., Braas, D. et al. (2018). Hexokinase 2 is targetable for HK1 negative, HK2 positive tumors from a wide variety of tissues of origin. *J Nucl Med*.

37. Yang, C. F., Gopula, B., Liang, J. J., Li, J. K., Chen, S. Y., Lee, Y. L. et al. (2018). Novel AR-12 derivatives, P12-23 and P12-34, inhibit flavivirus replication by blocking host de novo pyrimidine biosynthesis. *Emerg Microbes Infect*, *7*(1), 187.

38. York, A., Williams, K., Argus, J., Zhou, Q., Brar, G., Vergnes, L. et al. (2015). Limiting Cholesterol Biosynthetic Flux Spontaneously Engages Type I IFN Signaling. *Cell*, *163*(7), 1716-1729.

39. Yuan, T. L., Amzallag, A., Bagni, R., Yi, M., Afghani, S., Burgan, W. et al. (2018). Differential Effector Engagement by Oncogenic KRAS. *Cell Reports*, *22*(7), 1889-1902.

40. Zhang, T., Inesta-Vaquera, F., Niepel, M., Zhang, J., Ficarro, S. B., Machleidt, T. et al. (2012). Discovery of potent and selective covalent inhibitors of JNK. *Chem Biol*, *19*(1), 140-154.

41. Zhu, J., Huang, J. W., Tseng, P. H., Yang, Y. T., Fowble, J., Shiau, C. W. et al. (2004). From the cyclooxygenase-2 inhibitor celecoxib to a novel class of 3-phosphoinositide-dependent protein kinase-1 inhibitors. *Cancer Res*, *64*(12), 4309-4318.

CHAPTER 5

CONCLUSIONS AND FUTURE DIRECTIONS

One of the most pervasive hallmarks of cancer is genomic instability. It is clear that the maintenance of physiological dNTP levels is critical to sustain cellular proliferation and genome integrity. Through these studies, we have developed small molecule inhibitors that can modulate dNTP levels quantity and quality. We have further elucidated the interconnections between DNA synthesis and stress response signaling mechanisms, and generated strategies to obliterate cancer cells while sparing normal tissues.

Chapter 1: Nucleotide metabolism-RSR crosstalk

1. Quantification of alterations of nucleotide biosynthetic pathways in leukemia cells by ATR, the most upstream kinase in the replication stress response (RSR) pathway.

2. New therapeutic strategy to limit dNTP pools by combining existing modulators of nucleotide metabolism and RSR pathway.

3. Future studies

    1. Clinically applicable companion biomarkers like endogenous RS measurement that are predictive of responses in human tumors.

    2. Stratification of tumors based on contributions of *de novo* and salvage biosynthetic pathways.

    3. Therapeutic efficacy of targeting ATR and dCK in solid tumors with hypoxic tumor microenvironment (limited *de novo* activity).

Chapter 2: Pharmacology of dCK inhibitor, *(R)*DI-87

1. Preclinical development and pharmacology of a novel dCK inhibitor, *(R)*DI-87.

2. [^{18}F]CFA PET probe is used as a pharmacodynamic biomarker for measuring dCK activity to optimize DI-87 dose that resulted in maximal dCK inhibition.

3. PK-PD models for both dCK inhibition and tumor growth inhibition studies were used to optimize dosing schedules for first in-human clinical studies.

Chapter 3: Development of a potent copper ionophore

1. HCT-13, a novel isoquinoline based HCT was identified as a highly potent anti-proliferative against PDAC, SCLC and PC cancer models.

2. HCT-13 functions as a copper ionophore, and its cytotoxicity is attributed to production of ROS, and is mitochondrial function dependent.

3. Further, HCT-13 interferes with DNA replication arresting cells in S-phase, activating RSR pathway, and interacts with ATR inhibitor synergistically.

4. Ongoing studies - Development of Cu complex of HCT-13 and loading them in Mesoporous silica nanoparticles (MSN) for optimal bio distribution and delivery to tumors.

5. Future studies - Preclinical efficacy studies of MSN loaded Cu[HCT-13] in Prostate and PDAC cancer models.

Chapter 4: Metabolic modifier screen to identify secondary targets

1. Cell-based metabolic modifier screen is developed for the discovery of modulators of nucleotide biosynthetic pathways.

2. JNK-IN-8, a JNK inhibitor was discovered to be potent nucleoside transporter inhibitor.

3. OSU-03012, a PDK1 inhibitor was discovered to be a potent DHODH inhibitor, and confirmed by co-crystal structure with DHODH.

4. Clinical implications - JNK-IN-8 should not be used in conjunction with compounds, including cancer-treating antimetabolites, which rely upon nucleoside transport for their research or therapeutic purpose.

5. Similarly constructed phenotypic screens designed against other metabolic networks containing convergent nodes may find use in drug discovery campaigns or in repurposing screens using existing compounds.

Graphical Summary of Thesis